



저작자표시-비영리-변경금지 2.0 대한민국

이용자는 아래의 조건을 따르는 경우에 한하여 자유롭게

- 이 저작물을 복제, 배포, 전송, 전시, 공연 및 방송할 수 있습니다.

다음과 같은 조건을 따라야 합니다:



저작자표시. 귀하는 원저작자를 표시하여야 합니다.



비영리. 귀하는 이 저작물을 영리 목적으로 이용할 수 없습니다.



변경금지. 귀하는 이 저작물을 개작, 변형 또는 가공할 수 없습니다.

- 귀하는, 이 저작물의 재이용이나 배포의 경우, 이 저작물에 적용된 이용허락조건을 명확하게 나타내어야 합니다.
- 저작권자로부터 별도의 허가를 받으면 이러한 조건들은 적용되지 않습니다.

저작권법에 따른 이용자의 권리는 위의 내용에 의하여 영향을 받지 않습니다.

이것은 [이용허락규약\(Legal Code\)](#)을 이해하기 쉽게 요약한 것입니다.

[Disclaimer](#)

Ph.D. DISSERTATION

**A Study on Improved Cochlear
Implant: CNT Bundle-based Thin
Electrode Array and Implantable
Multi-channel Connector**

향상된 인공와우 장치에 대한 연구:

탄소나노튜브 기반의 얇은 전극과

생체삽입형 다채널 커넥터

BY

GWANG JIN CHOI

FEBRUARY 2020

**DEPARTMENT OF ELECTRICAL
AND COMPUTER ENGINEERING
COLLEGE OF ENGINEERING
SEOUL NATIONAL UNIVERSITY**

A Study on Improved Cochlear Implant: CNT Bundle-based Thin Electrode Array and Implantable Multi-channel Connector

지도교수 김 성 준

이 논문을 공학박사 학위논문으로 제출함
2020년 1월

서울대학교 대학원
전기·정보공학부
최 광 진

최 광 진의 공학박사 학위논문을 인준함
2019년 12월

위 원 장 홍 용 택 (인)

부위원장 김 성 준 (인)

위 원 오 승 하 (인)

위 원 전 상 범 (인)

위 원 임 윤 섭 (인)

Abstract

Cochlear implant is a neural prosthesis that restores the hearing ability in people suffering from severe hearing loss. For decades, the effectiveness and safety of cochlear implant have been established and cochlear implant has benefited more than half a million recipients worldwide. However, there have been issues that need to be addressed to increase hearing ability such as atraumatic electrode insertion, safe re-implantation surgery, hearing performance improvement, increase of effective stimulation channels, and low-cost device. In this dissertation, the following issues of cochlear implant are studied: atraumatic insertion and cochlear implant re-implantation.

An implantable device of cochlear implant is composed of a hermetic package generating electrical stimulation pulses and an intracochlear electrode array interfacing the auditory nerves to apply stimulation pulses. However, the insertion procedure of an intracochlear electrode array into the cochlea can cause structural tissue damage, which determines the hearing performance. In this dissertation, a thin and flexible carbon nanotube (CNT) bundle-based electrode array is suggested to reduce the trauma during electrode insertion procedure. CNT has been studied for potential use in biomedical fields, including fabrication of microelectrode array or neural probe for lower stiffness than metal-based electrodes. The fundamental principle of the fabrication process is to encapsulate CNT bundles to form a multi-channel intracochlear electrode array. Each CNT bundle is used for an individual

electrode channel after being coated with parylene-C for insulation. The developed electrode array has a thickness of 135 μm at the apex and 395 μm at the base, which is thinner than conventional intracochlear electrode arrays. The insertion test and animal experiments are performed to evaluate the flexibility and feasibility of the electrode array. Insertion forces are measured during insertion of the fabricated electrode array into a human cochlea model. And, the electrode array is acutely implanted into an SD rat to record the electrical auditory brainstem responses (eABR). The CNT bundle-based intracochlear electrode array shows 6-fold lower insertion force than metal wire-based electrode array, and the eABR waves are evoked by the electrical stimulation via the fabricated electrode array.

Additionally, an implantable connector used in numerous neural prostheses can have advantages such as simplification of surgery and safe replacement of implantable devices. As neural prostheses have been developed, the requirements for miniaturized implantable multi-channel connectors also have increased. Also, an implantable connector can contribute to the safe and simple re-implantation procedure of cochlear implant. In current cochlear implant, an intracochlear electrode array is inseparable from a hermetic package. If an implantable connector for cochlear implant guarantees the miniaturized size sufficient for implantation and long-term reliability, the connection of an electrode array and a hermetic package using an implantable connector can make implant surgery more flexible and reduce the risk of trauma during replacement surgery. In this study, an experimental prototype of a re-connectable and miniaturized implantable multi-channel connector is presented. The implantable connector, which has female-to-female bidirectional

structure, is fabricated by the thermal press bonding of micro-patterned liquid crystal polymer (LCP) films. For simple electrical connection, a bump structure is formed inside the connector to apply the contact pressure between conductor lines of the connector and those of the inserted cable. After being connected to cables, the connector is sealed with silicone-based packings and tightened by metal cases, which results in the maximum channel density of 28.3 channel/cm². The repeated connection test is performed to verify the durability and the re-connectability of the fabricated connector. The contact resistances of the four and eight-channel connectors are 53.2 mΩ and 75.2 mΩ, respectively, and remain almost the same values during 50 times of repeated connection tests. *In vitro* accelerated soak tests are carried out to assess the sealing performance and the long-term reliability, and the fabricated connector samples show 79 days of average soak time in a 75 °C saline environment until device failure.

In summary, a CNT bundle-based intracochlear electrode array is developed and evaluated via measurement of mechanical characteristics and *in vivo* animal test. In addition, an implantable multi-channel connector is assessed in terms of electrical & mechanical characteristics and sealing performance. It is expected that the proposed intracochlear electrode array may reduce the risk of trauma during electrode insertion surgery with minimized insertion force. And, if the enhancement of the channel density and the sealing performance of the proposed implantable connector is followed, the connector can be applied to cochlear implant for safe re-implantation procedure.

Keywords: cochlear implant, intracochlear electrode array, atraumatic insertion, carbon nanotube, re-implantation, implantable connector, high channel density

Student Number: 2015-20997

Contents

Abstract	i
Contents	v
List of Figures	viii
List of Tables	xvi
List of Abbreviations	xvii
Chapter 1 Introduction	1
1.1 Overview of Cochlear Implant	2
1.2 Conventional Cochlear Implant	3
1.3 Proposed Cochlear Implant	8
1.3.1 CNT Bundle-based Thin Intracochlear Electrode Array ----	9
1.3.2 Implantable Multi-channel Connector	10
1.4 Dissertation Outline	13
Chapter 2 Materials and Methods	14
2.1 Carbon Nanotube (CNT) Bundle-based Thin Intracochlear Electrode Array	15
2.1.1 Electrode Array Configuration	15
2.1.2 Fabrication Process	16
2.1.3 Evaluations	22

2.1.3.1	Insertion and Extraction Force Measurement -----	22
2.1.3.2	Mechanical Simulation -----	23
2.1.3.3	Electrochemical Analysis -----	24
2.1.3.4	<i>In Vivo</i> Animal Test -----	25
2.2	Implantable Multi-channel Connector -----	29
2.2.1	Connector Design -----	29
2.2.2	Fabrication Process -----	32
2.2.3	Evaluations -----	38
2.2.3.1	Measurements of Electrical Characteristics -----	38
2.2.3.2	Repeated Connection Test -----	40
2.2.3.3	<i>In Vitro</i> Accelerated Soak Test -----	41
Chapter 3	Results -----	45
3.1	CNT Bundle-based Thin Intracochlear Electrode Array -- -----	46
3.1.1	Fabricated Electrode Array -----	46
3.1.2	Insertion and Extraction Force in Scala Tympani Model ---	49
3.1.3	Simulation of Horizontal and Vertical Deflection -----	53
3.1.4	Electrochemical Characteristics -----	54
3.1.5	Electrical Auditory Brainstem Response (eABR) Recording - -----	57
3.2	Implantable Multi-channel Connector -----	61
3.2.1	Fabricated Connector -----	61
3.2.2	Measurement of Contact Resistance -----	64

List of Figures

Figure 2.1 CNT bundle-based intracochlear electrode array. -----	15
Figure 2.2 A SEM image of CNT bundle having ribbon-shape. -----	16
Figure 2.3 Fabrication of CNT-bundle based intracochlear electrode array. (a)-(c) Each CNT bundle is electroplated with gold, and then parylene C is coated on the surface of electroplated CNT bundle. (d) 8 CNT bundles are cut to fit the lengths of different channels and electrode sites & connecting pads are exposed by laser ablation. (e)-(f) All the CNT bundles are vertically stacked up and encapsulated with silicone elastomer. (g) Electrical contacts with external electronics are made using silver epoxy. -----	18
Figure 2.4 Gold electroplating of CNT bundles. The CNT bundles are fixed on a square frame to avoid being curled up. Gold electroplating process is performed at -4 V DC voltage for 5 sec. -----	19
Figure 2.5 Parylene C evaporation process. Gold electroplated CNT bundles are attached at a height of 0.5 mm by double-sided adhesive tapes for conformal coating. -----	19
Figure 2.6 (a) Electrode lead CAD drawing of 4-inch photolithography mask. (b) Enlarged view of connection pads at electrode side (pitch: 250 μm). (c)	

Enlarged view of connection pads at electronics side (pitch: 500 μm). --- -----	21
Figure 2.7 Schematic of the insertion/extraction force measurement setup. -----	23
Figure 2.8 Modeling of CNT bundle-based electrode array. -----	24
Figure 2.9 Experimental setup for eABR recording. (a) Illustration of the eABR recording setup. (b)-(c) Photograph of anesthetized rat with inserted CNT bundle-based electrode array and cochleostomy opening site. -----	27
Figure 2.10 A photograph of stimulation pulse generator [92]. -----	28
Figure 2.11 Overall configurations of implantable multi-channel connector. (a) LCP- based bidirectional connector and cable. (b) Assembled connector with metal cases. (c) Detailed cross-sectional image of the implantable connector: bump structure for contact pad junction, silicone elastomer packings for prevention of water leakage, and the metal cases to apply mechanical pressure to the packings. Block-shape packings are in both sides of the metal cases to seal the gap between the connector and the cable. Ring-shape packing is placed in the groove of the metal case to seal the gap between the joint of the metal cases. -----	31
Figure 2.12 Fabrication process of LCP-based connector and cable. (a) Attachment of LCP film on silicon wafer. (b) Metal seed layer deposition. (c) Photolithography. (d) Electroplating of gold layer. (e) Wet etching of the photoresist and the metal seed layer. (f) 3-stage and (f') Planar pressing	

jig for thermal press lamination of the LCP films. (g) and (g') Laser micro-machining for outline cutting and laser ablation (for the case of cable). ----- 33

Figure 2.13 CAD drawing (4-inch photolithography mask) of four-channel (a) connector and (b) cable (pad width: 300 μm , pitch: 500 μm). ----- 34

Figure 2.14 CAD drawing (4-inch photolithography mask) of eight-channel (a) connector and (b) cable (pad width: 150 μm , pitch: 250 μm). ----- 35

Figure 2.15 3-stage pressing jig for thermal lamination of LCP-based connector. (a)-(c) third, second, and first stage. (d) detaching procedure of the second stage. (e) Enlarged view of protruding plate with empty space for bump structure. ----- 36

Figure 2.16 Silicone elastomer molds for (a) ring-shape and (b)-(c) block-shape packings. ----- 37

Figure 2.17 Block-shape packings with (a) 125 %, (b) 137 %, and (c) 150 % volume ratio to internal space of metal case. ----- 38

Figure 2.18 Assembly procedure of entire connector parts. (a) Insertion of LCP cables into LCP connector with block-shape packings. (b) Metal cases and ring-shape packing (c) Fastening metal cases through cables. (d) Assembly of metal case with screw threads. ----- 38

Figure 2.19 Electrical characteristic measurement of LCP-based connector. (a) Measurement of assembled connector resistance. (R_{Total} : Assembled

connector resistance, R_{Load} : Load resistance, I : Current through load resistor, V_{Total} : Voltage across the assembled connector) (b) Measurement of contact resistance between the connector and cable (R_{Cable} : Cable resistance, $R_{Connector}$: Connector resistance, $R_{Contact}$: Contact resistance). --
 ----- 40

Figure 2.20 *In vitro* leakage test setup. Sample groups are immersed in PSB solution at 75 °C. Leakage and crosstalk current are measured using a picoammeter and a switching board for changing of measurement mode. - 42

Figure 2.21 Switching board with switches for line and mode conversion. (a) Photograph of the switching board. (b) Outline of the switching board. --
 ----- 42

Figure 2.22 Equivalent circuits of (a) two parallel conductor lines for crosstalk current model and (b) a conductor line for leakage current model. Conductor lines of the same length and width are assumed. ----- 44

Figure 3.1 CNT bundle-based intracochlear electrode array. (a) Photograph of the fabricated intracochlear electrode. Arrows at left and right indicate electrode sites at its base and apex, respectively. (b) LCP-based electrode lead (c) Electrode sites from base (1st site) to apex (8th site). Bidirectional arrows indicate each corresponding electrode site. ----- 47

Figure 3.2 SEM images of CNT bundle with numerous CNTs entangled. ----- 48

Figure 3.3 Experimental setup of insertion and extraction force measurements of 8-

channel CNT bundle-based intracochlear electrode array in scala tympani model. ----- 50

Figure 3.4 (a) Insertion force measurements of 8-channel CNT bundle-based intracochlear electrode array and metal wire-based dummy electrode array. (b) Enlarged view of a dashed rectangle portion in (a). Average and standard deviation of measured values are shown. ----- 51

Figure 3.5 (a) Extraction force measurements of 8-channel CNT bundle-based intracochlear electrode array and metal wire-based dummy electrode array. (b) Enlarged view of a dashed rectangle portion in (a). Average and standard deviation of measured values are shown. ----- 52

Figure 3.6 Simulation results of (a) horizontal and (b) vertical stiffness of CNT bundle-based electrode array. (c) Simulation result of metal wire-based dummy electrode array. ----- 53

Figure 3.7 Electrochemical properties of CNT bundle-based electrode array. (a) EIS: impedance magnitude (black) and phase angle (grey) are shown over frequency. (b) CV of the electrode array is measured in the range of -0.6 – 0.8 V. Average and standard deviation of measured values are shown. ----- 55

Figure 3.8 Electrochemical properties of various electrode materials. (a) Area-specific impedances and (b) CSCc magnitudes of various electrode materials are shown. ----- 56

Figure 3.9 Recorded eABR waves at (a) 1st, (b) 2nd, and (c) 3rd electrode sites. The recorded eABR voltage waveforms corresponding to different magnitudes of electrical stimulation current are combined in each graph. ----- 60

Figure 3.10 (a) Fabricated 4 & 8-channel LCP connector and cable. Contact pads with a width of 300 μm (4-channel) and 150 μm (8-channel). (b) Side view of the 4-channel LCP cable: thick insertion part inserted into the connector with a thickness of 450 μm and thin lead part with a thickness of 250 μm . (c) The LCP connector and inserted LCP cable. (d) Cross-sectional view of the LCP connector and cable. The bump structure applying the contact pressure to the contact pads. ----- 62

Figure 3.11 (a) LCP-based connector, cable, and metal cases. (b) Protrusion and groove structure of the metal cases with a width of 400 μm . Ring-shape packing is located at the groove of the metal case. (c) the assembled connector with the metal cases. ----- 63

Figure 3.12 Assembled connector resistance of (a) 4-channel connector and (b) 8-channel connector with 50, 60, and 70 mm of conductor line length. Contact resistances are obtained in the limit of the zero-length ($L = 0$ mm). ----- 65

Figure 3.13 Repeated resistance measurements of the fabricated LCP connector. Average and standard deviation of measured resistances are shown. -- 66

Figure 3.14 Four-channel connector samples sealed with (a) dental resin, (b) silicone elastomer, and (c) metal cases & packings. The thickness of the covered dental resin and silicone elastomer is 0.5 mm. ----- 68

Figure 3.15 Leakage and crosstalk current measurements during the *in vitro* accelerated soak test. Connector samples sealed with (a) dental resin (D-1, D-2, and D-3) and (b) silicone elastomer (S-1, S-2, and S-3). Connector samples assembled with metal cases and block-shape packings having (c) 125 % (B1-1, B1-2, and B1-3), (d) 137 % (B2-1, B2-2, and B2-3), and (e) 150 % (B3-1, B3-2, and B3-3) volume ratios. (Threshold level: 0.731 μ A, EL: estimated lifetime, Measurement of B2-3 is still in progress) --- ----- 71

Figure 4.1 Linear estimation of the proposed electrode array. The thickness of the 22 channel CNT bundle-based electrode array is estimated based on the thicknesses at the apex (135 μ m) and the base (395 μ m). ----- 74

Figure 4.2 SEM images of the gold electroplated CNT bundle with numerous gold particles. ----- 75

Figure 4.3 SEM images of (a) gold sputtered CNT bundle and (b) gold electroplated Pt/Ir wire. ----- 76

Figure 4.4 Scala tympani model with inserted intracochlear electrode array. Directions of horizontal and vertical deflection are described. ----- 79

Figure 4.5 Recorded eABR wave at the 1st electrode site at 500 μ A of current

stimulation level. ----- 81

Figure 4.6 Contact pads of the LCP-based cable (a) before and (b) after the repeated
connection test. ----- 85

List of Tables

Table 2.1 Properties of electrode materials used for mechanical simulation [79-90]. -----	24
Table 3.1 Manufacturers and dimensions of intracochlear electrode arrays [7, 14, 45- 47]. -----	48
Table 4.1 Characteristics of biocompatible polymer materials [90, 131-135]. -----	83
Table 4.2 Dimensions of implantable multi-channel connectors [67-70, 139]. -----	87

List of Abbreviations

Abbreviation	Term
CNT	Carbon Nanotube
CSCc	Cathodic Charge Storage Capacitance
CV	Cyclic Voltammetry
DBS	Deep Brain Stimulation
EAS	Electric Acoustic Stimulation
eABR	Electrical Auditory Brainstem Response
EIS	Electrochemical Impedance Spectroscopy
IACUC	Institutional Animal Care and Use Committee
LCP	Liquid Crystal Polymer
MTTF	Mean Time to Failure
PBS	Phosphate-Buffered Saline
SD	Sprague-Dawley
ST	Scala Tympani
PFA	Perfluoroalkoxy Alkane
Pt/Ir	Platinum/Iridium
MRI	Magnetic Resonance Imaging

◆ Note

Some parts of this dissertation are extracted and adapted from the journal publication which was published during the course of this study:

- ◆ Gwang Jin Choi, Tae Mok Gwon, Doo Hee Kim, Junbeom Park, Seung Min Kim, Seung Ha Oh, Yoonseob Lim, Sang Beom Jun, and Sung June Kim, “CNT bundle-based thin intracochlear electrode array,” *Biomedical Microdevices*, 21(27), 2019.

Chapter I

Introduction

1.1 Overview of Cochlear Implant

Neural prosthesis is an artificial system that uses electrical stimulation of the nervous system to restore impaired sensory or motor functions from neural diseases. A neural prosthesis typically consists of an external and an implantable device. An external device collects environmental signals, processes the signals and wirelessly transmits data & power into the implantable device. And the implantable device generates multiple trains of electrical pulses based on the transmitted data & power and sends the stimulation pulses to the target nervous system via an electrode array [1-3]. Cochlear implant, retinal implant, and deep brain stimulation (DBS) are the most successful neural prostheses currently used in the clinic. Cochlear implant has benefitted people with severe hearing loss by restoring hearing ability using electrical stimulation of the auditory nerve [4-7]. Retinal implant also implanted into the recipients, who have retinitis pigmentosa or age-related macular degeneration, to substitute the retina and stimulate the optic nerve [8, 9]. DBS uses electrical stimulation with an electrode array placed into the brain to treat neuropathic disorders associated with Parkinson's disease, essential tremor, and neuropathic pain [10-13].

Cochlear implants can restore the hearing capability in people suffering from sensorineural hearing loss caused by the damage of the hair cells. As sound waves enter the ear in normal hearing people, vibration signals are provoked by the sound waves striking the eardrum and transferred to the hair cells located in the basilar membrane of the spiral-shaped cochlea. The basilar membrane responds to higher frequencies at its base and lower frequencies at its apex, which is organized

tonotopically and acts like a frequency analyzer. As movements of the stereocilia on the hair cells in the basilar membrane are detected, the hair cells transform the vibration signals into electrical neural signals which are delivered via the auditory nerve to the auditory cortex. However, the hair cells can be damaged by genetic defects, infections, exposure to loud noise, drug abuse, and aging, which results in hearing loss. Cochlear implant substitutes and replaces the role of the hair cells and generates neural signals by electrically stimulating the auditory spiral ganglion nerves cell connected to the hair cells. Cochlear implant includes an external speech processor and an implantable device. The external speech processor picks up environmental sounds by a microphone, divides the input sound signals into a number of frequency bands, and wirelessly transmits power and processed data into the implantable device through a transcutaneous coil link. The implantable device, hermetically sealed by titanium packaging, produces electrical stimulation pulses according to the received data and conveys the pulses to an intracochlear electrode array. Then, each channel of the intracochlear electrode array elicits the neural responses around the auditory ganglion cells that are tuned to the corresponding frequency bands. Eventually, the electrically evoked neural responses at the various frequencies result in restoration of hearing [14].

1.2 Conventional Cochlear Implant

For decades, the effectiveness and safety of cochlear implant have been successfully established. In 2017, almost 500,000 recipients, who have hearing loss related to the damage of the hair cells, have received cochlear implant worldwide

[15]. However, there are other problems that need to be addressed in order to increase hearing performance. Degree of recovered hearing capability with cochlear implant is known to rely upon various issues including atraumatic insertion, re-implantation surgery, improvement of hearing performance, number of effective stimulation channels, and low-cost device [16, 17].

The intracochlear electrode array plays a highly important role in determining the recovery level of hearing ability. In cochlear implant, the multichannel electrode array is inserted into the scala tympani (ST) of the cochlea and interfaces the tonotopically organized auditory nerve cells by delivering the electrical pulses. The surgical procedure of the intracochlear electrode array insertion is primarily critical as the electrode array can easily damage the delicate cochlear structures by rupturing the basilar membrane & spiral ligament or penetrating the basilar membrane/osseous spiral lamina [18]. Trauma of this nature can significantly deteriorate the coupling between the electrode array and the target nerve cells as well as the residual hearing capacity. The geometrical design and the material of the intracochlear electrode array can also significantly influence the range of traumas in the cochlea [17, 19-21]. Conventional intracochlear electrode arrays contain multiple metal wires, such as platinum or platinum/iridium (Pt/Ir) alloy, inside a silicone elastomer carrier, which can increase the stiffness of the electrode array [22]. As the stiffness of the electrode array increases, the frictional forces between the electrode array and cochlear inner wall increases, thus enlarges the risk of trauma [14, 23]. In addition, to deliver sufficient current pulses to the target nerves, conventional intracochlear electrode arrays typically have a large electrode site area, which leads

to an increase in the thickness [24].

As a large number of recipients have gained access to cochlear implants, a growing number of device failures and revision procedures are expected [25-29]. Approximately 7.6 % of recipients have undergone cochlear implant revision in a few months to years. Reasons for implant revision include evident device breakdown, device migration/extrusion, decreased device performance, and infection/wound complications, which makes re-implantation inevitable. In addition, there have been modifications in the structures and the electronics of cochlear implant, and as new technology and coding strategies continue to advance, the re-implantation surgery to increase hearing performance can be considered. Also, as pediatric cochlear implantations have increased, many recipients may outlive the lifespan of their implant. For example, cochlear implant procedures are commonly operated on children as young as 12-month, and successful device performances for a 6-month old infant have been reported [30, 31]. However, many potential problems, such as tissue trauma resulting from explantation & re-implantation, difference in insertion depth/modiolus proximity, and decreases in performance can be followed during the re-implantation procedure [31, 32]. Almost 40 % of replacement implant recipients have shown a decrease in speech recognition ability [25]. The structure of cochlear implant, in which the intracochlear electrode array and the electronic packaging are combined into a one-body system, can be one of the reasons increasing the risk of re-implantation. Even if revisions are required only due to the problems of structures/electronics, explantation and replacement of the electrode are unavoidably accompanied, which causes additional insertion trauma.

Although cochlear implant has surprisingly succeeded with an excellent speech perception performance rate of 80 – 90% in a quiet environment, the sound perception level of cochlear implant recipient still has limitations compared to the natural hearing sensation [33, 34]. Many challenges remain to be solved for the restoration of the hearing performance to the natural hearing, such as a wide range of outcomes, music/tone perception, speech recognition in a noisy environment, and sound localization. Some researches for the performance improvements have focused on development of advanced external speech processor. Various processing strategies have been introduced like Compressed Analog, Interleaved Pulses, F0/F1/F2 Processing, Spectral-/Multi-peak coding, and Advanced Combinational Encoder, which tries to deliver formant, syllable, pitch information [35-38]. Currently, Continuous Interleaved Sampling, which uses a pulsatile process for non-simultaneous stimulation, is widely applied in commercial devices. And, there have been approached to use combined electric and acoustic stimulation (EAS) for recipients having a residual and low-frequency hearing. As low-frequency sound is provided with a hearing aid, high-frequency region is stimulated by means of cochlear implant, which leads to better hearing performance in noise or music listening [39-41]. Furthermore, bilateral electrical stimulation with cochlear implant on both sides is advantageous to provide good sound localization and speech perception in noisy environments [42]. However, the amount of information perceived by these strategies and methods is still much less than natural acoustic stimuli. Also, the implantable device and the intracochlear electrode array have not evolved significantly since the first introduction of a multi-channel cochlear implant.

A person with normal hearing has approximately 3,000 inner hair cells directly connected to about 10,000 – 40,000 spiral ganglion nerve cells [43, 44]. In comparison, conventional cochlear implants have 12 to 22 stimulation channels [7, 14, 45-47]. To deliver large quantity of information and improve the hearing performance, the number of effective stimulation channels also has to increase. However, conventional Pt/Ir wire-based cochlear electrode array is fabricated via manual processes by skilled workers, which precludes the scaling of the electrode array and limits integration of high-channel system. Silicon-based and polymer-based intracochlear electrode arrays have been proposed to offer the high-density of electrode channels using precise semiconductor fabrication processes, but these electrode arrays are not yet applied to full cochlear implant system but are rather in research stages [48-51]. Also, because electrical stimulation pulses spread out in conductive lymph fluid causing interference between the channels, the high-density electrode array does not simply lead to the increase of the distinct perceptual channel number. Therefore, field-shaping strategies have been designed to increase the number of distinguishable channel and spatial selectivity. Field-shaping is the modulation of intracochlear electric fields by using multi-polar stimulation techniques or varying the proportion of current delivered to adjacent electrode sites [52-55]. Although there are controversies about the effect of field shaping strategies, a few studies reported improved pitch perception and cochlear implant performance.

Also, the cost reduction of the cochlear implant is necessary for patients in developing countries. The cost of cochlear implant alone is about \$25,000, not including examination, implantation surgery, and postoperative care [56].

Considering the effectiveness and the benefits, the high cost is the main reason preventing more widespread use of cochlear implant [16]. In developed countries where cochlear implant manufacturers sell most of their products, cochlear implant is generally covered by national health programs. However, in developing countries without national health insurance, cochlear implant is unavailable and unaffordable to most patients. And the manual electrode fabrication process and the hermetic titanium packaging make mass production difficult and the device cost high. Thus, there are obvious needs for the development of a low-cost cochlear implant while maintaining current performance.

1.3 Proposed Cochlear Implant

Among the issues of cochlear implant described above, the following issues are under consideration in this dissertation.

- (1) Atraumatic insertion with thin intracochlear electrode array
- (2) Safe re-implantation procedure using implantable multi-channel connector

A thin and flexible intracochlear electrode array can be advantageous for minimizing the trauma likely to occur during electrode insertion. In this study, the development of a carbon nanotube (CNT) bundle-based thin intracochlear electrode array for atraumatic insertion is proposed. In addition, there is unavoidable explantation of an intracochlear electrode array during re-implantation, which

increases additional insertion trauma. In order to reduce the unconditional tissue trauma during the re-implantation procedure, an implantable multi-channel connector connecting the electrode array to the hermetic package is proposed.

1.3.1 CNT Bundle-based Thin Intracochlear Electrode Array

An atraumatic intracochlear electrode array is indispensable for high cochlear implant performance and EAS, in which the preservation of residual hearing is significant. The fundamental principle of the proposed CNT bundle-based electrode array is to substitute each metal wire used for conventional intracochlear electrode arrays with the CNT bundle. CNT, assembled microtubules of graphitic carbon, has been applied for numerous fields to date [57]. It is known that CNT is one of the numerous allotropes of carbon and exhibits a nanometric-level cylindrical structure as a sheet of graphene rolled into a cylinder. Owing to its extraordinary mechanical, electrical, thermal, and optical characteristics, the range of applications has been expanded to various fields in industry as well as for research. Microelectronics, energy storage, Fabrication of coating/film, and composite materials are currently major applications of CNT [58]. In addition, CNT has been widely studied for their potential in the biomedical fields [59-61]. In particular, there have been several trials to fabricate neural interface electrodes using CNT. The effectiveness of CNT-based microelectrode arrays or neural probes was demonstrated in both acute and chronic animal experiments [62-64]. CNT-based neural probes exhibited a lower stiffness than metal-based electrodes, resulting in enhanced mechanical characteristics for reduction of tissue damage [64]. These

previous results indicated that CNT could be used as a safe and efficient substitute for metal wires used in neural interface electrodes. In this study, multiple CNT bundles were assembled to form a multi-channel intracochlear electrode array as a substitute for metal wires. Fabricated by spinning methods, the CNT bundle has an entangled structure of numerous individual CNTs [65]. Due to the mechanical characteristics of the CNT bundle, it enables the development of a new intracochlear electrode array minimizing the insertion trauma. Mechanical and electrochemical characteristics of the proposed electrode were compared with a metal wire-based intracochlear electrode array. Moreover, the eABR of an SD rat was measured to demonstrate the feasibility of electrical stimulation delivered via the electrode array made from CNT bundles.

1.3.2 Implantable Multi-channel Connector

The implantable device of conventional cochlear implant is composed of an inductive coil, an electronic circuit, a titanium package, and an intracochlear electrode array. As the electronic circuit is hermetically sealed by the titanium package to protect from the body fluid, the electrode array is connected to the electronics via feedthrough, which makes cochlear implant an undetachable one-body system. Because the hermetic package, implanted in the temporal region of the head, is located close to the electrode array such that an extension cable is not necessary, an implantable connector has not been applied to cochlear implant device to date. Also, cochlear implant system having a one-body structure is advantageous to the long-term reliability of electronic circuits. However, if an implantable

connector is used for connection between the electrode array and the hermetic package, it can contribute to a safer and more flexible re-implantation procedure of cochlear implant [31, 32]. Definitely, the implantable connector for cochlear implant needs to ensure implant stability and long-term reliability comparable to those of a one-body system.

Many implantable connectors have been presented with different structures and materials for assembly and de-assembly of connection components. A ‘Craggs connector’, which is a plug-and-socket type connector, was introduced for a lumbar anterior root stimulator system. After being insulated by silicone rubber adhesive, the Craggs connector was disconnected by cutting the adhesive sealant for device replacement. The Craggs connector showed high leakage path impedance in saline solution for three months, and the stimulator implanted with the connectors had worked successfully for two years [66, 67]. A two-male-plug type connector, called ‘in-line connector’, was also used with an implantable stimulator system for neuromuscular excitation [68]. The junction between the male pins was made within a center spring for proper electrical contact, and a silicone elastomer cuff covered the entire connection part by being closed with surgical suture. No leakage currents from the in-line connector were detected in *in vitro* and *in vivo* experiments for 38 months and 49 months, respectively. An implantable connector with circular-shaped contact pads is being used for pacemaker or deep brain stimulation devices [69, 70]. As a connector pin having several contact pads was inserted, silicone elastomer o-rings were located between the pin and cavity to prevent body fluid leakage from reaching to the contact pads. The circular contact type connector has been widely

used with pacemaker or deep brain stimulation devices for patients in many clinical applications and operated successfully and safely for years. Owing to good electrical contact characteristics and hermetic seal capable of multiple usages, these connectors have been able to stand the continuous passing of stimulation current pulses during entire implantation and replacement of the implanted devices have been easily accomplished.

However, although there have been many studies and researches for implantable connectors, previous connectors had low channel numbers with metal pin-based contacts, time-consuming procedure for opening & reassembly, or lack of long-term reliability evaluation. In this study, a prototype of an implantable and re-connectable multi-channel connector with high channel density is proposed and evaluated in terms of the mechanical characteristics and the sealing performance. The bidirectional female type connector and male type cable were fabricated using liquid crystal polymer (LCP). Using LCP as substrate material, metal contact pads were fabricated by a micro-patterning process, and the three-dimensional connector structure was formed through thermal press bonding. After the female connector and the male cable were connected, the connector was sealed by metal cases to tighten silicone elastomer packings. The metal cases were assembled by a screw on the metal cases, which enables the simple replacement process and reduces the diameter of the connector. Repeated connection tests and acceleration leakage tests were performed to demonstrate the durability and the long-term reliability of the fabricated connectors.

1.4 Dissertation Outline

This dissertation is addressing the fabrication and evaluation of a CNT bundle-based intracochlear electrode array and an implantable multi-channel connector.

In the chapter 2, materials and methods for the electrode array and the implantable connector are shown. The fabrication and evaluation of the intracochlear electrode array are introduced in the chapter 2.1. The fabrication process of the CNT bundle-based electrode is devised, and *in vivo* animal test & measurement of the physical and electrochemical characteristics is detailed. Next, the design and assessment of the implantable multi-channel connector are explained in the chapter 2.2. The configuration of the bidirectional LCP-based connector is suggested, and repeated connection tests and *in vitro* accelerated soak tests are detailed.

In the chapter 3, results are arranged in a similar order as the chapter 2. The fabricated intracochlear electrode array and the implantable multi-channel connector are shown in the chapter 3.1 and the chapter 3.2, respectively. The feasibility and mechanical characteristics of the electrode array are demonstrated in the subsections of chapter 3.1. And, the following subsections in chapter 3.2 present the re-connectability and the long-term reliability of the connector.

In the chapter 4, discussions explore the capability of the electrode array and the implantable connector developed in this study and deals with their further development potentials.

The dissertation is finished with a concluding paragraph for summary and future work in the chapter 5.

Chapter II

Materials & Methods

2.1 Carbon Nanotube (CNT) Bundle-based Thin intracochlear Electrode Array

2.1.1 Electrode Array Configuration

The configuration of the proposed CNT bundle-based intracochlear electrode array is depicted in Figure 2.1. The CNT bundles have a shape similar to that of a ribbon with numerous carbon nanotubes entangled with an average cross-section of $115\ \mu\text{m}$ width and $9.94\ \mu\text{m}$ height (Figure 2.2). Gold and parylene C layers are coated on the CNT bundles as a protection layer for a laser ablation process and an insulation layer, respectively. After eight bundles are arranged at fixed spatial interval of 2 mm and encapsulated with silicone elastomer, the 8-channel intracochlear electrode array can cover 16 mm of active stimulation region along the cochlea. And, each bundle is attached to an electrode lead part for connection to an external stimulating electronics.

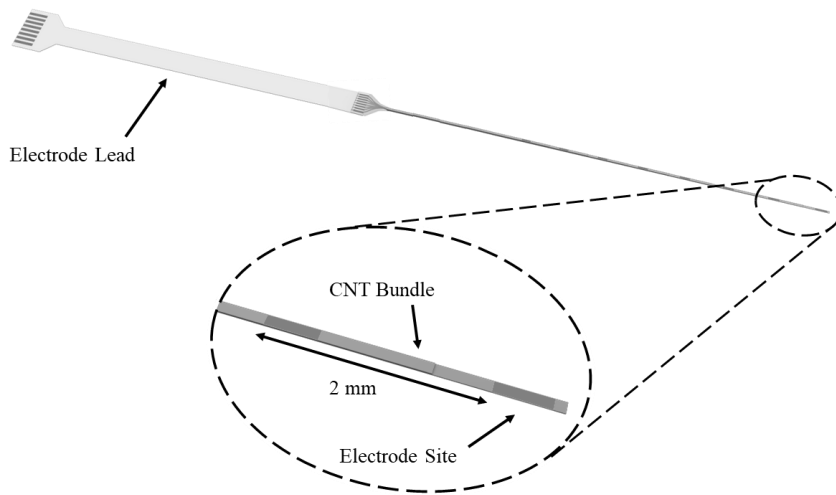


Figure 2.1 CNT bundle-based intracochlear electrode array.

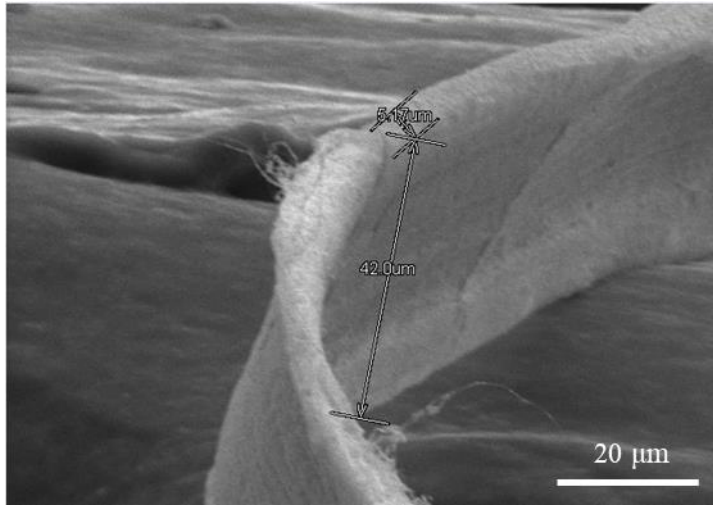


Figure 2.2 A SEM image of CNT bundle having ribbon-shape.

2.1.2 Fabrication Process

Figure 2.3 illustrates the detailed procedure to fabricate the intracochlear electrode array with CNT bundles. The CNT bundle (provided by Carbon Composite Materials Research Center, Institute of Advanced Composite Materials, Korea Institute of Science and Technology) was synthesized using a direct spinning process [71, 72]. The detailed procedure is as follows: First, the surface of the CNT bundles was electroplated with a 10 μm thick gold layer. The gold layer was used to protect the surface of the CNT bundles from following laser ablation process for site opening. Potassium gold cyanide ($\text{KAu}(\text{CN})_2$, SME trading Co. Seoul, Korea) was used as electroplating solution, and electroplating was performed at - 4 V DC voltage for 5 sec for each CNT bundle. To prevent the pliable CNT bundles from being curled up during the gold electroplating process, the CNT bundles were immersed in the electroplating solution with both ends fixed to square frame (Figure 2.4). Subsequently, 3 μm thickness of parylene C was evaporated on the electroplated

CNT bundles using a vapor deposition system (SCS Labcoter 2, PDS 2010, Specialty Coating Systems, IN, USA). To conformally coat the parylene C layer on every surface of the bundles, the electroplated CNT bundles were fixed at a height of 0.5 mm via double-sided adhesive tapes (NEM tape, Nisshin EM Co., Ltd., Tokyo, Japan) from the surface of a silicon wafer (Figure 2.5). Then, the coated CNT bundles were cut to fit each channel length considering the inter-channel distance (2 mm) and channel number (8-channel). After the cutting, the parylene C layer of the bundle was ablated with a UV laser machining system (355 nm wavelength, Samurai UV Laser Marking System, DPSS Lasers, CA, USA) to expose the electrode sites and connection pads. The electrode sites were placed at the end of each bundle and have a length of 0.5 mm and the width of each bundle. Then, the CNT bundles were stacked vertically with the inter-channel distance and encapsulated within medical-grade silicone elastomer (MED 6233, Nusil Silicone Technology, CA, USA). Finally, the connection on the opposite side of the electrode sites was attached to the electrode lead by using conductive epoxy (H20E Epotek, Epoxy Technology, MA, USA) and encapsulated with the silicone elastomer.

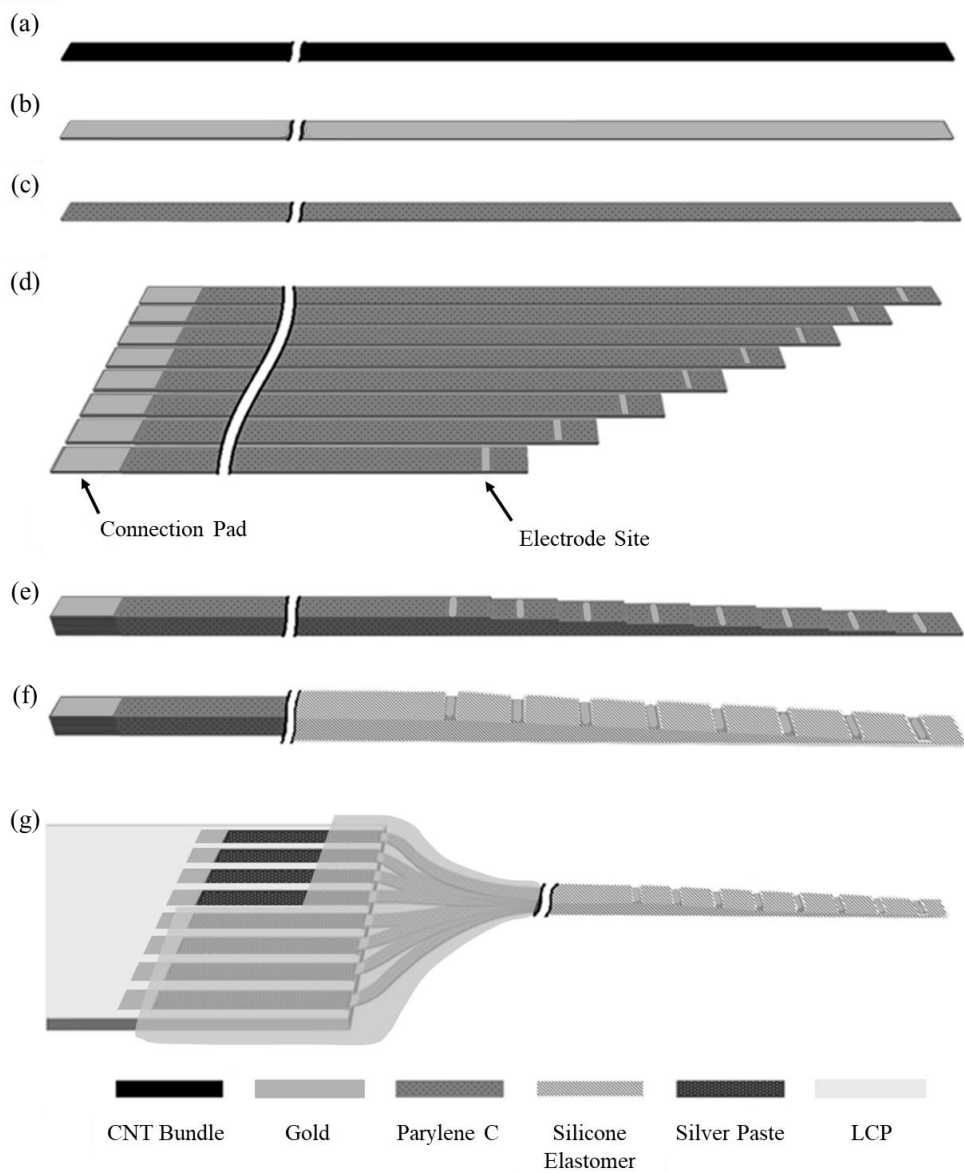


Figure 2.3 Fabrication of CNT-bundle based intracochlear electrode array. (a)-(c) Each CNT bundle is electroplated with gold, and then parylene C is coated on the surface of electroplated CNT bundle. (d) 8 CNT bundles are cut to fit the lengths of different channels and electrode sites & connecting pads are exposed by laser ablation. (e)-(f) All the CNT bundles are vertically stacked up and encapsulated with silicone elastomer. (g) Electrical contacts with external electronics are made using silver epoxy.

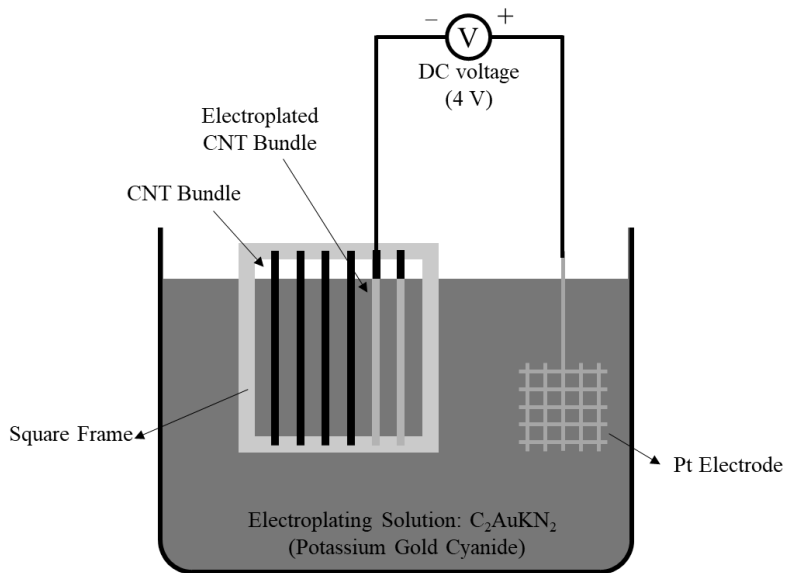


Figure 2.4 Gold electroplating of CNT bundles. The CNT bundles are fixed on a square frame to avoid being curled up. Gold electroplating process is performed at -4 V DC voltage for 5 sec.

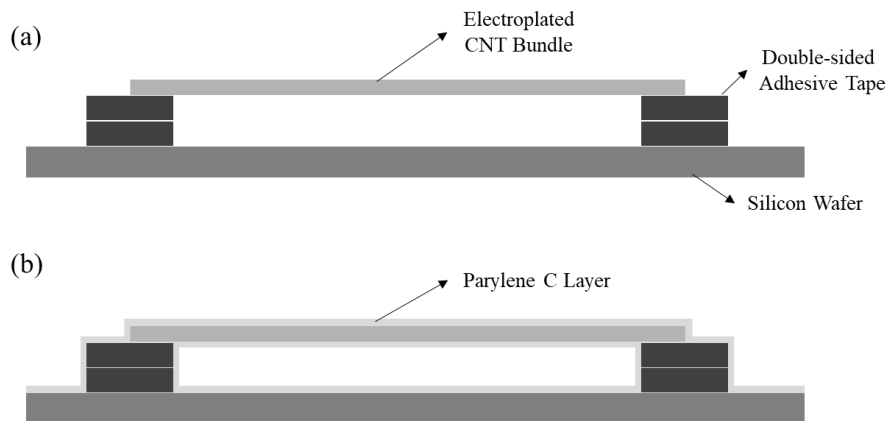


Figure 2.5 Parylene C evaporation process. Gold electroplated CNT bundles are attached at a height of 0.5 mm by double-sided adhesive tapes for conformal coating.

The fabrication of the 8-channel electrode lead is based on previously reported LCP fabrication processes [50, 51, 73-75]. The silicone elastomer was spin-coated on a silicon wafer as an adhesion layer (2000 rpm, 70 sec) and cured at 120 °C for 1 hour. And, an LCP film (Vecstar CTZ-25, Kuraray, Tokyo, Japan) was fixed on the silicon wafer using the silicone elastomer. The LCP film fixed on the silicon wafer was immersed sequentially in acetone, methanol, and isopropyl alcohol for 1 min each for surface cleaning of the LCP film. Also, the surface of the LCP film was cleaned and activated by oxygen plasma (150 W, 100 sccm, 3 min; Plasmalab 80 plus, Oxford Instruments, U.K.). Afterward, 50 nm of titanium and 150 nm of gold were evaporated on the activated LCP films with an E-gun evaporator (ZZS550-2/D, Maestech Co., Ltd., Pyungtaek, South Korea) as metal seed layers for following electroplating process. Subsequently, a 10- μm -thick photoresist mask layer (AZ4620, Clariant, USA) was patterned onto the metal seed layer using an aligner (MA6/BA6, SUSS MicroTec, Garching, Germany) and a 10 μm of gold layer was electroplated. After the photomask was removed, the seed layer was wet-etched with aqua regia and hydrofluoric acid. The metal-patterned LCP film was detached from the silicon wafer and cut to the size of a planar pressing jig with the UV laser machining system. An additional LCP film (Vecstar CTF-25, Kuraray, Tokyo, Japan) was also cut for a cover layer. Then, the metal-patterned layer and the cover layer were aligned in the pressing jig and laminated together using a thermal press machine (15 min, 295 °C, 1 MPa; Model 4122, Carver, Wabash, IN, USA). After the lamination, connection pads were opened by the laser ablation and the electrode lead outline was decided by final laser cutting. The connection pads had 250 μm of pitch at the electrode side and

500 μm of pitch at the electronics side, which is the same as that of a commercial 8-pin connector (5034800800_sd, Molex Incorporated, IL, USA), as shown in Figure 2.6.

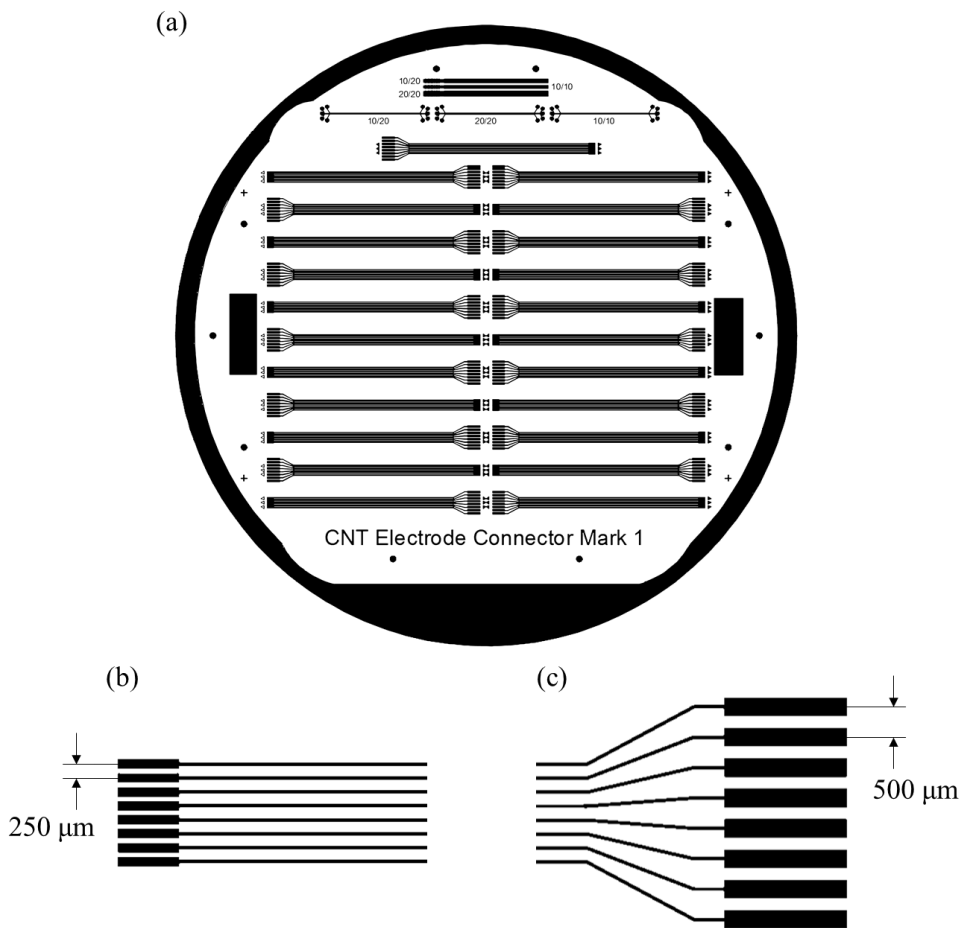


Figure 2.6 (a) Electrode lead CAD drawing of 4-inch photolithography mask. (b) Enlarged view of connection pads at electrode side (pitch: 250 μm). (c) Enlarged view of connection pads at electronics side (pitch: 500 μm).

2.1.3 Evaluations

2.1.3.1 Insertion and Extraction Force Measurement

In order to examine the insertion and extraction forces exerted by the fabricated intracochlear electrode array, a plastic human ST model was employed in combination with a custom-made force measurement system (Figure 2.7). The fabricated electrode array was fixed on a force/torque sensor (Nano17, ATI, NC, USA) that was tethered to a motorized linear actuator (LTA-HS, Newport, CA, USA). By using the motorized linear actuator, the electrode was gradually inserted and extracted in a plastic human ST model. The insertion and extraction speeds were fixed at 0.6 mm/s. 50% glycerin aqueous solution was filled in the ST model as a lubricant mimicking the viscosity of the fluid in the human cochlea [50, 51, 76-78]. During the insertion and extraction processes, a customized LabVIEW-based program was used to record the displacements and the instantaneous forces caused by vertical deflection of the electrode array.

To compare with conventional metal wire-based intracochlear electrode array, a dummy electrode array was built with Pt/Ir alloy wires (90:10 wt%, bare diameter: 25 μm , coated diameter: 33 μm , AM Systems, Inc., WA, USA). Eight metal wires were arranged at the same spatial interval of the CNT bundle-based electrode array and encapsulated with the silicone elastomer. The developed dummy electrode array had a diameter of 0.3 mm at the apex and 0.75 mm at the base, respectively. Three electrodes with either CNT bundle or metal wire were tested 10 times and the average insertion or extraction forces were calculated.

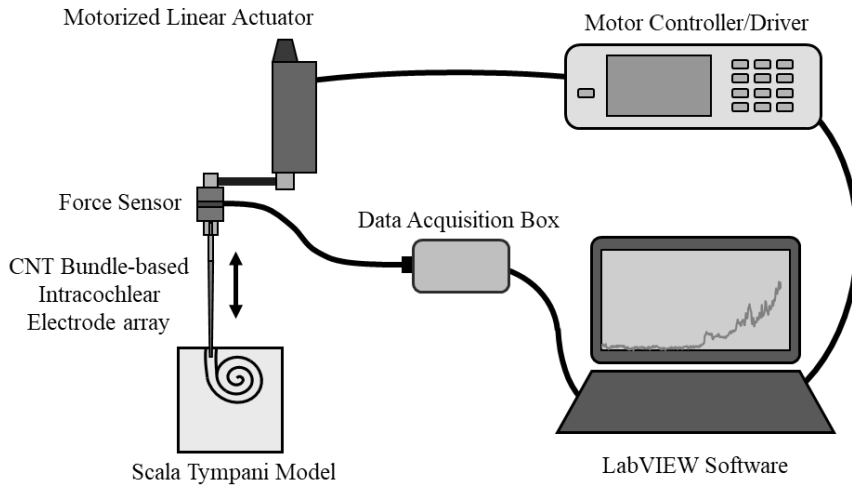


Figure 2.7 Schematic of the insertion/extraction force measurement setup.

2.1.3.2 Mechanical Simulation

Because the electrode array was fabricated with the CNT bundles having ribbon-shape, the CNT bundle-based electrode array had a rectangular cross-section. Therefore, it is expected to be a stiffness difference in vertical and horizontal directions. Finite element analysis software (Static Structural, ANSYS) was used to simulate the stiffness when the electrode array is bent in both vertical and horizontal directions. An electrode array model was generated based on the composition and dimension of the developed electrode array (Figure 2.8). Also, the stiffness of the dummy electrode array was simulated for comparison with conventional metal wire-based intracochlear electrode array. The young's modulus and Poisson's ratio of materials of the electrode arrays used for the stiffness simulation are listed in Table 2.1.

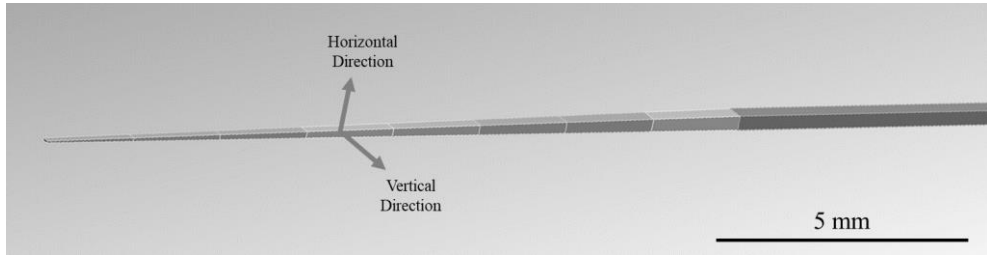


Figure 2.8 Modeling of CNT bundle-based electrode array.

Table 2.1 Properties of electrode materials used for mechanical simulation [79-90].

<i>Material</i>	<i>Young's modulus (GPa)</i>	<i>Poisson's ratio</i>
CNT	15	0.3
Gold	80	0.42
Parylene C	2.76	0.4
Silicone Elastomer	0.5	0.5
Pt/Ir 90:10	164	0.38
PTFE	2.25	0.42

2.1.3.3 Electrochemical Analysis

To assess the electrochemical characteristics of the fabricated CNT bundle-based electrode array, electrochemical impedance spectroscopy (EIS) was performed. An impedance analyzer (1260 and 1287A, Solartron Analytical, Farnborough, UK) and a three-cell electrochemical system with an Ag/AgCl reference electrode and a platinum counter electrode were used. The electrolyte was a phosphate-buffered saline (PBS) solution (#10010-023, Gibco, ThermoFisher Scientific, MA. USA) of pH 7.4. The root-mean-square magnitude of the applied voltage was 10 mV, and the excitation frequency range was 1 Hz to 100 kHz. Also, cyclic voltammetry (CV) curve was obtained to calculate the cathodic charge storage capacitance (CSCc)

using a potentiostat (1287A, Solartron Analytical, Farnborough, UK) and the three-cell electrochemical system. In order to obtain the CV, current density was measured and plotted while the electrochemical potential of the electrode array was swept in the range between -0.6 V and 0.8 V versus the Ag/AgCl reference electrode at a sweep rate of 50 mV/s. The CSCc value was calculated by integrating the negative area of the obtained CV.

In addition, the EIS and CV curves before and after the gold electroplating were obtained to ascertain the change in the electrochemical characteristics due to the electroplating. Identical electrochemical analyses of gold-sputtered CNT bundles (Gold: 500 nm, Titanium as adhesion layer: 20 nm) were also performed to determine if there are dissimilarities in the gold deposition method. Finally, the electrochemical properties of Pt/Ir alloy wires were measured before and after gold electroplating. To directly compare the impedances of various electrode materials regardless of their surface areas, the area-specific impedance is reported. The area-specific impedance is defined as the impedance multiplied by the geometrical area of the exposed region on the electrode array.

2.1.3.4 *In Vivo* Animal Test

In order to verify the effectiveness of the developed CNT bundle-based intracochlear electrode array, the eABR was recorded after delivering electrical stimulation via the electrode array. Ten-week-old Sprague-Dawley (SD) rat (weight: 330 g) was anesthetized by an intramuscular injection of a mixture of tiletamine /zolazepam (30 mg/kg) and xylazine (5 mg/kg). Then, the tip of the electrode array

was acutely implanted through the cochleostomy opening of the right ear up (Figure 2.9). Owing to the short cochlear length of the SD rat, only the first three electrode sites at the apex were inserted into the cochlea (5 mm in depth). A custom-made stimulation pulse generator was used to generate electrical current pulses, and the cathodic first biphasic current pulses (amplitude: 0 – 500 μ A, duration: 100 μ s, rate: 20 Hz) were applied in a soundproof shielding room (Figure 2.10). After applying the electrical stimuli through the electrode array, the eABR waves were obtained using the smartEP USB Box system (Intelligent Hearing Systems, Miami, FL, USA) [51, 91]. The eABR threshold was determined as the minimum stimulation level required to evoke recognizable waves. This work has been collaborated with Doo Hee Kim & Prof. Seung Ha Oh of Department of Otorhinolaryngology-Head and Neck Surgery in Seoul National University Hospital for eABR measurement, and Shinyong Shim of Department of Electrical and Computer Engineering in Seoul National University for preparing the pulse generator. All the procedures were approved by the Institutional Animal Care and Use Committee of Seoul National University (IACUC no. 15-0190-C1A1).

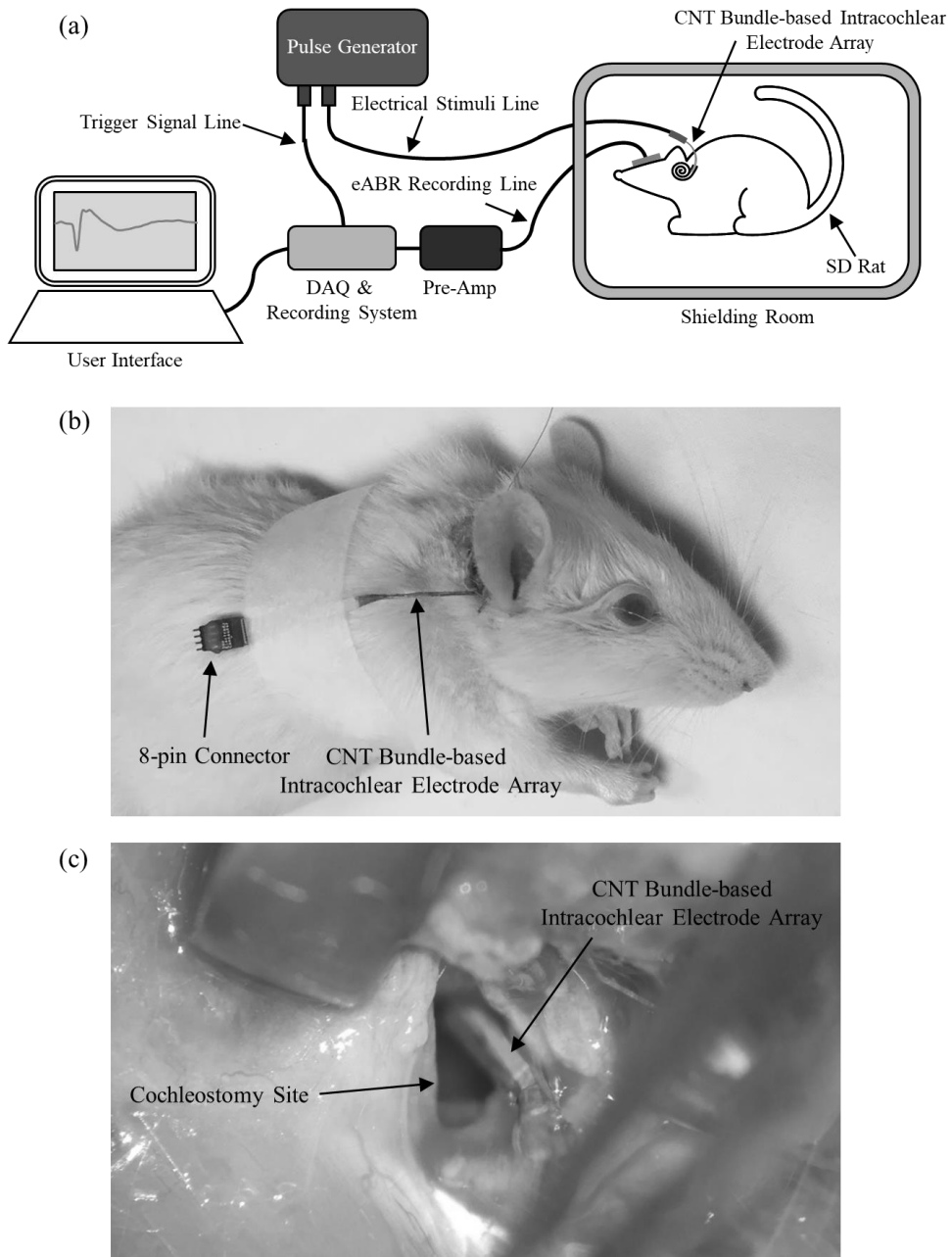


Figure 2.9 Experimental setup for eABR recording. (a) Illustration of the eABR recording setup. (b)-(c) Photograph of anesthetized rat with inserted CNT bundle-based electrode array and cochleostomy opening site.

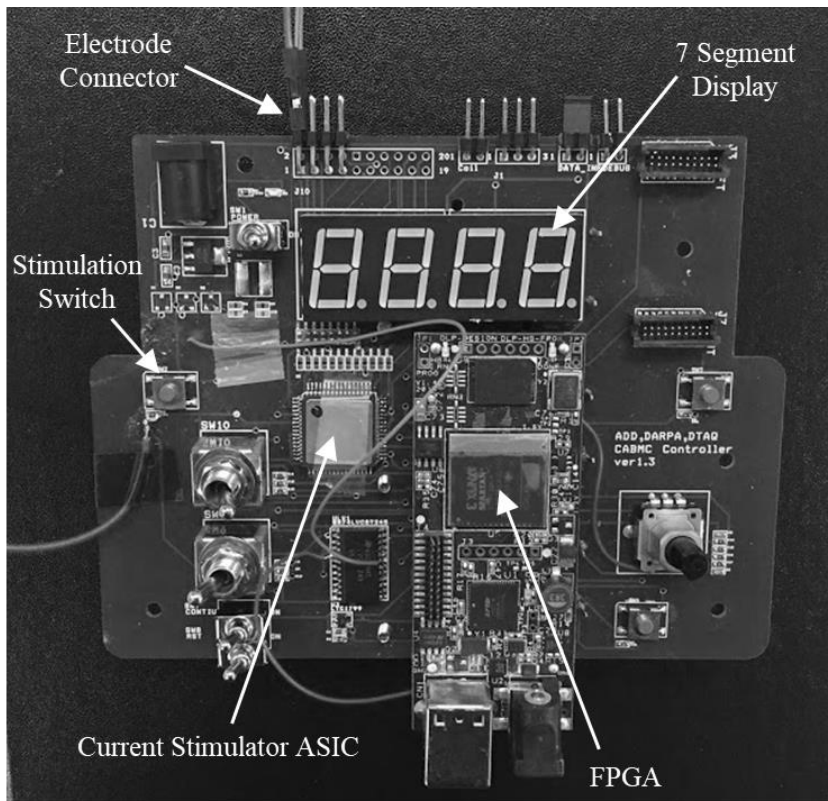


Figure 2.10 A photograph of stimulation pulse generator [92].

2.2 Implantable Multi-channel Connector

2.2.1 Connector Design

LCP, one of the widely used biocompatible polymers such as polyimide, parylene-C, SU-8, and silicone elastomer, has been applied for many biomedical fields due to its good mechanical and chemical stability [73, 74, 93-98]. LCP exhibits numerous advantages, including the compatibility with micro-fabrication processes, suitable magnetic permeability, high thermal deformation capacity, and lower water absorption rate (<0.04 %) than other biocompatible polymers such as parylene-C (0.06 – 4 %) and polyimide (0.24 – 4 %) [90, 98-100]. With the characteristics described above, LCP has been used for implantable devices like deep-brain stimulation [74, 75, 101, 102], retinal implant [73, 100], and cochlear implant [50, 51, 99]. In addition, studies on long-term evaluations are conducted not only *in vitro* but also *in vivo*, which shows superior reliability to polyimide and parylene-C [103, 104].

One of the important characteristics of LCP for biomedical applications is its compatibility with micro-fabrication processes. LCP is chemically inert and not damaged by commonly used micro-fabrication processes such as cleaning with organic solvents, development/removal of photoresist, and metal etching using acidic etchants. Therefore, micron-scale metal patterns can be formed on the LCP film for microelectrode arrays [50, 51, 74, 75, 101]. Another important property of LCP is high thermal deformation capacity. Multiple LCP films can be thermally laminated together without adhesive layers, which enables manufacturing of three-dimensional structures, monolithic biomedical devices, and multilayered electrode

array through simple thermal press process [100, 105-107].

The configuration of the LCP-based connector with cables and the metal cases is shown in Figure 2.11. The bidirectional female type connector based on LCP is fabricated using the thermal bonding press process with a micro-patterned LCP film and additional LCP films. The contact pads are on both bottom side of the connector. Bump structures are located upside of the contact pads to apply the contact pressure between the contact pads of the connector and the inserted cables. After the connection, ring-shape and block-shape packings, which are made of silicone elastomer, are placed to seal the gaps between the joint of outer metal cases and between the connector & the cable, respectively, for prevention of water passage. And, the metal cases are assembled by a screw thread parts to tighten the silicone elastomer packings. The block-shape packings have inclines helping the easy insertion into the metal case. The LCP-based cables pass through the slits in the metal cases. The cables have thick insertion part and thin lead part. As the slit of the metal case has a thickness that allows the thin lead part to pass but not the thick insertion part, the slit prevents the thick insertion part of the cable from passing through so that the cable can be fixed after the insertion into the connector.

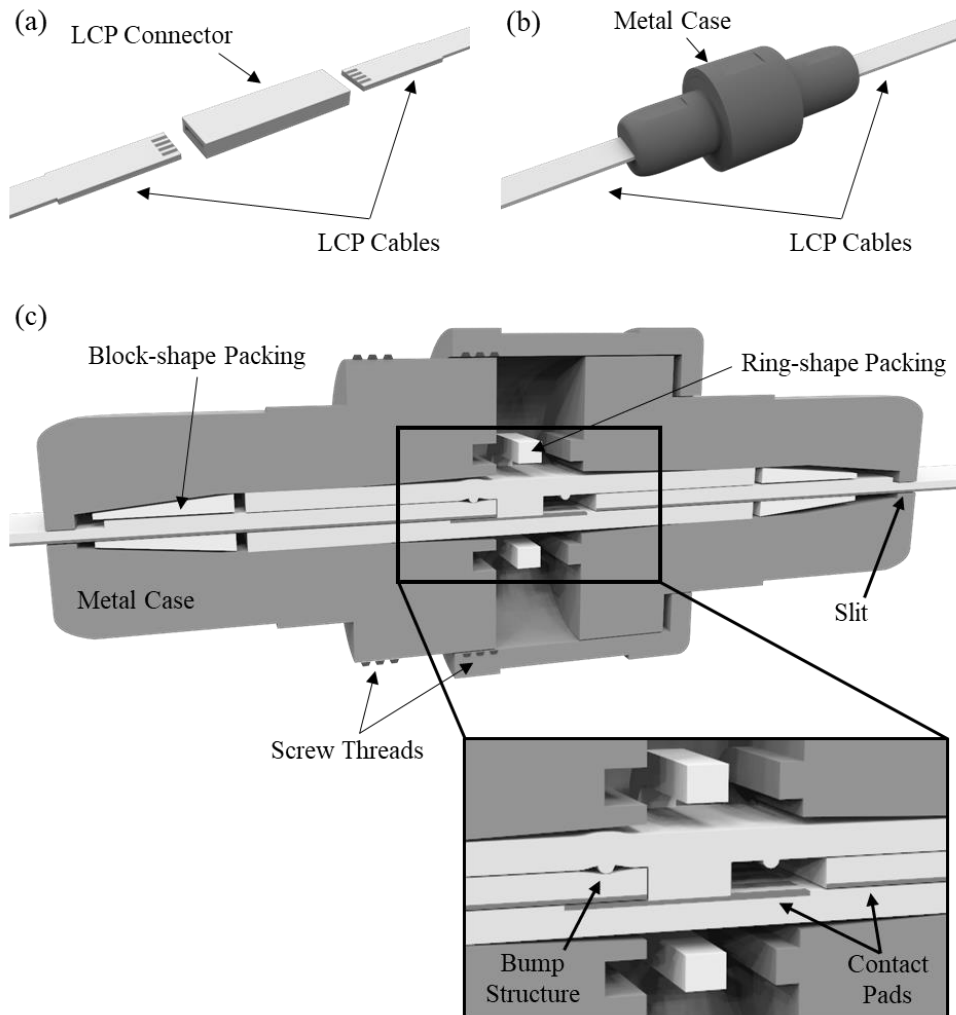


Figure 2.11 Overall configurations of implantable multi-channel connector. (a) LCP-based bidirectional connector and cable. (b) Assembled connector with metal cases. (c) Detailed cross-sectional image of the implantable connector: bump structure for contact pad junction, silicone elastomer packings for prevention of water leakage, and the metal cases to apply mechanical pressure to the packings. Block-shape packings are in both sides of the metal cases to seal the gap between the connector and the cable. Ring-shape packing is placed in the groove of the metal case to seal the gap between the joint of the metal cases.

2.2.2 Fabrication Process

The fabrication process of the LCP-based connector and cable is similar to the process described in the section 2.1.2. Figure 2.12 shows the detailed fabrication process schematically. The metal-patterned LCP films for the four & eight-channel connector and cable were fabricated by the micro-fabrication process and cut to the size of pressing jigs with the laser machining system (Figure 2.13 and Figure 2.14). Additional LCP films (Vecstar CTF-25 & CTF-100, Kuraray, Tokyo, Japan) were also cut and aligned with the metal-patterned LCP films in pressing jigs to form the structures of the connector and cable. A 3-stage pressing jig was used for the lamination of the LCP-based connector (Figure 2.15). The metal-patterned LCP film was located at the first stage with additional LCP films. At the second stage parts, additional LCP films were placed with protruding plates so that spaces for the cables are generated. And, the second stage parts can be detached after the thermal lamination so that the connector formed inside the jig can be taken out. Also, the second stage parts have empty spaces filled with melted additional LCP films during the thermal lamination to form the bump structures. Lastly, additional LCP films were located on the third stage. On the other hand, a planar pressing jig was used for the thermal lamination of the LCP-based cable. After LCP films were aligned in each pressing jig, the LCP-based connector and cable were laminated with the thermal press lamination. Subsequently, the connector and cable were fabricated by cutting the outlines with the laser machining system. In the case of the cable, further laser ablation processes were performed to open the contact pad and to make the thin lead part.

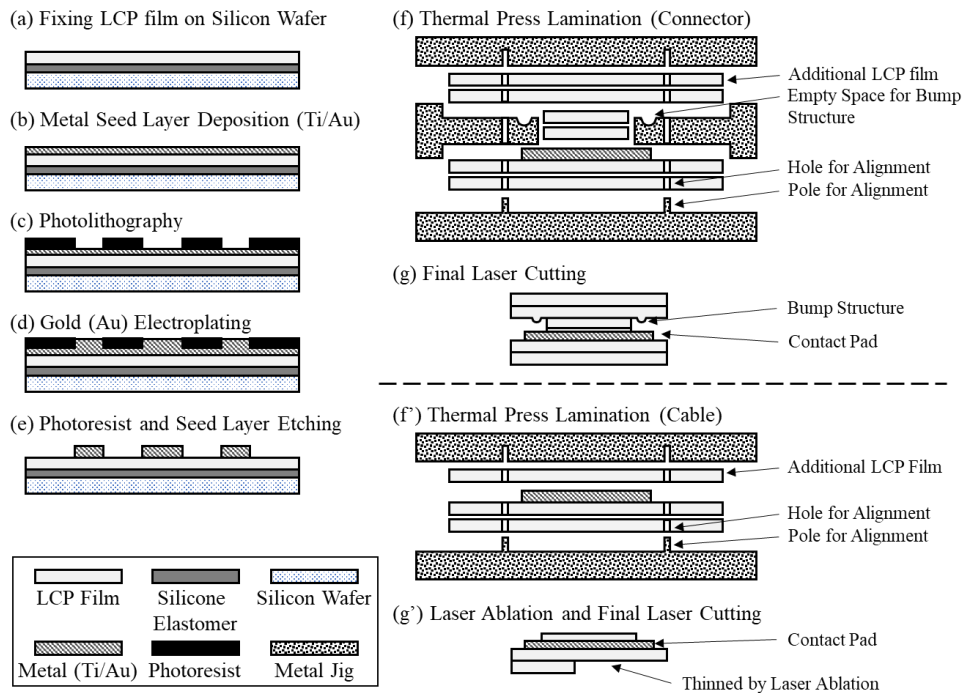


Figure 2.12 Fabrication process of LCP-based connector and cable. (a) Attachment of LCP film on silicon wafer. (b) Metal seed layer deposition. (c) Photolithography. (d) Electroplating of gold layer. (e) Wet etching of the photoresist and the metal seed layer. (f) 3-stage and (f') Planar pressing jig for thermal press lamination of the LCP films. (g) and (g') Laser micro-machining for outline cutting and laser ablation (for the case of cable).

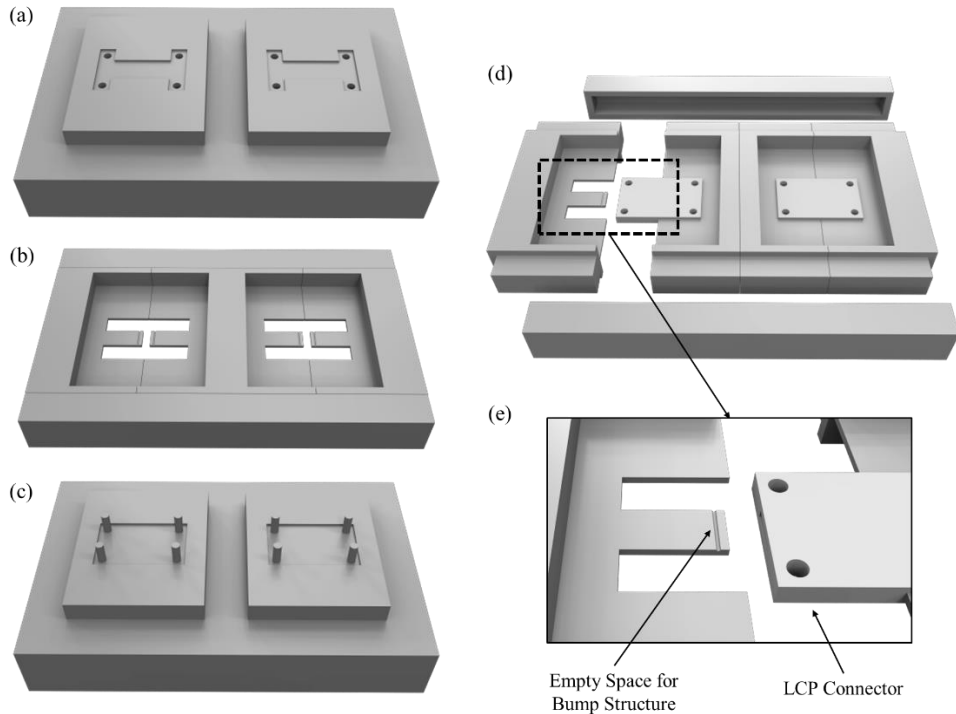


Figure 2.15 3-stage pressing jig for thermal lamination of LCP-based connector. (a)-(c) third, second, and first stage. (d) detaching procedure of the second stage. (e) Enlarged view of protruding plate with empty space for bump structure.

The ring-shape and block-shape packings were fabricated by curing the medical-grade silicone elastomer (MED-6233) with custom molds (Figure 2.16). The ring-shape packing has 400 μm width and 500 μm thickness, which is 100 μm thicker than the groove in the metal case. The block-shape packings were fabricated with 125, 137, and 150 % of volume inside the metal case to decide the optimal design for the prevention of water leakage (Figure 2.17). The silicone elastomer packings and the metal case were assembled on the fabricated connector and the cable (Figure 2.18). After the cables were inserted into the connector, the block-shape packings were located at both sides of the connector. The metal cases were

fastened to tighten the block-shape packings through the cables, and the ring-shape packing was placed between the metal cases. Finally, the metal cases were assembled with screw threads applying mechanical pressures to the block-shape and ring-shape packings. The opening & disassembly of the connector is performed in the reverse of the above assembly procedure. Additionally, if the LCP connector or the silicone elastomer packings are damaged, they can be replaced with new parts during the reassembly procedures.

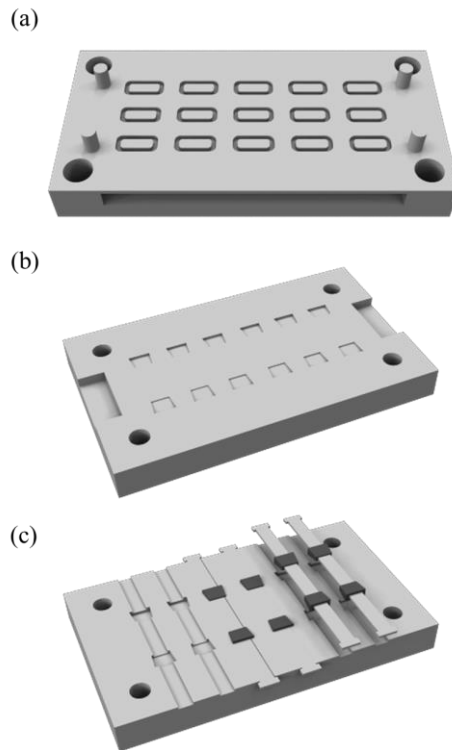


Figure 2.16 Silicone elastomer molds for (a) ring-shape and (b)-(c) block-shape packings.

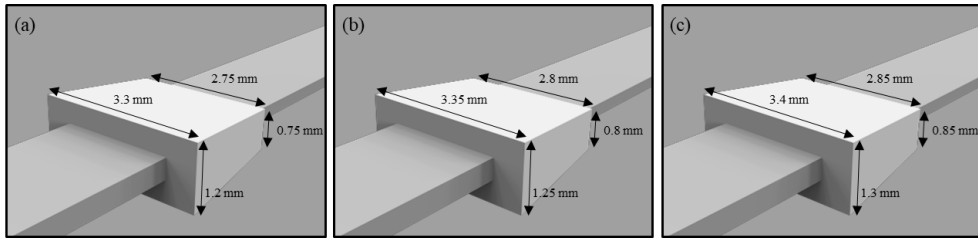


Figure 2.17 Block-shape packings with (a) 125 %, (b) 137 %, and (c) 150 % volume ratio to internal space of metal case.

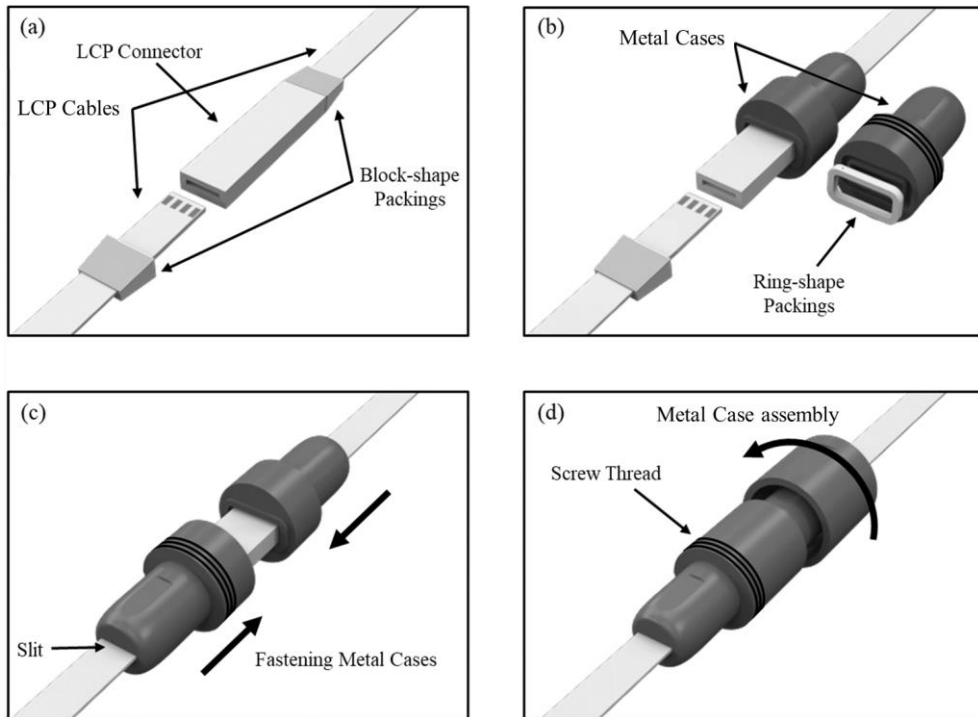


Figure 2.18 Assembly procedure of entire connector parts. (a) Insertion of LCP cables into LCP connector with block-shape packings. (b) Metal cases and ring-shape packing (c) Fastening metal cases through cables. (d) Assembly of metal case with screw threads.

2.2.3 Evaluations

2.2.3.1 Measurements of Electrical Characteristics

The resistance of each conductor line was measured after the assembly of the LCP-based connector and cable. Figure 2.19 shows the measurement setup for

the assembled connector resistance (R_{Total}) and the contact resistance (R_{Contact}) of the connector. The low resistance of the assembled connector was calculated with the current (I) through the load resistor (R_{Load}) and the voltage (V_{Total}) across the assembled connector. Also, the contact resistance of the connector was determined based on the transmission line method. The assembled connector resistance and the sum of the cable & connector resistances can be expressed as follows:

$$2R_{\text{Cable}} + R_{\text{Connector}} = \rho \frac{L}{A}, (L = L_1 + L_2 + L_3)$$

$$R_{\text{Total}} = 2R_{\text{Cable}} + R_{\text{Connector}} + 2R_{\text{Contact}} = \rho \frac{L}{A} + 2R_{\text{Contact}}$$

(ρ : Resistivity of conductor,

L: Length of conductor line,

A: Cross-sectional area of conductor line)

As the assembled connector resistance depends on the cable length, several measurements were made with different cable lengths (L_1 , L_2 : Length of the cable, L_3 : Length of the conductor line in the connector). Then, a plot of the assembled connector resistance versus the length of the conductor line was obtained. In the limit of a zero-length connector, the residual resistance is twice the contact resistance by extrapolating the plot back to $L = 0$ mm.

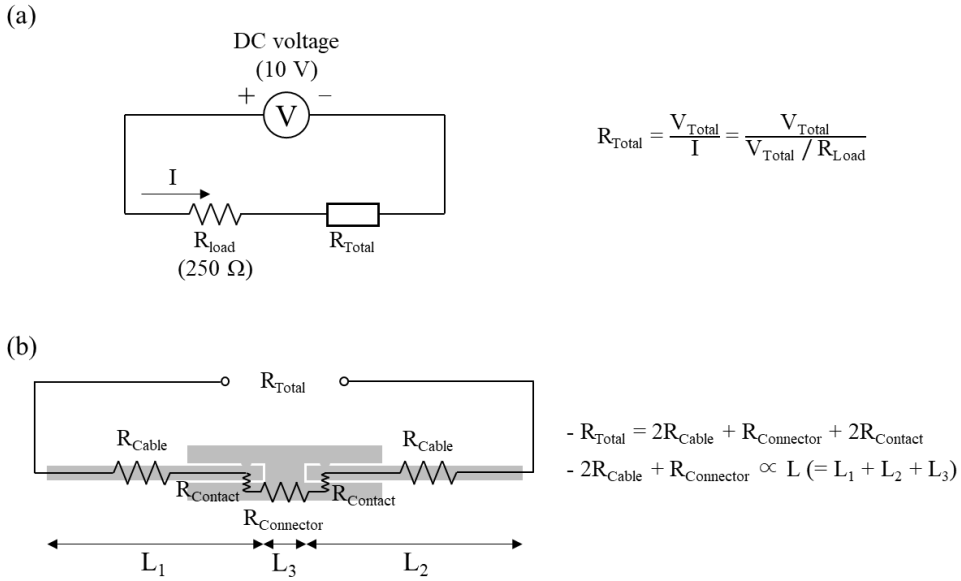


Figure 2.19 Electrical characteristic measurement of LCP-based connector. (a) Measurement of assembled connector resistance. (R_{Total} : Assembled connector resistance, R_{Load} : Load resistance, I : Current through load resistor, V_{Total} : Voltage across the assembled connector) (b) Measurement of contact resistance between the connector and cable (R_{Cable} : Cable resistance, $R_{Connector}$: Connector resistance, $R_{Contact}$: Contact resistance).

2.2.3.2 Repeated Connection Test

In order to examine the re-connectability of the proposed connector, repeated connection tests were performed. The LCP-based cables were inserted into both ends of the bidirectional LCP-based connectors, and one cable was repeatedly disconnected & connected. The assembled connector resistance (R_{Total}) and the contact resistance ($R_{Contact}$) were measured for each connection. Three connectors with four & eight-channels were tested for 50 cycles of connections, and the average of the assembled connector and contact resistance were obtained.

2.2.3.3 *In Vitro* Accelerated Soak Test

Accelerated soak tests were conducted to evaluate the long-term reliability of the assembled connector (Figure 2.20). The four-channel connector samples were immersed in 75°C PBS solution (10010–023, pH 7.4, Gibco, Thermo Fisher Scientific, MA, USA) which mimics salty body fluid, and deionized water was supplied to maintain the water level and the ion concentration. The water leakage was determined through the presence of leakage currents between each conductor line & a platinum-rod reference electrode, and the crosstalk was determined by the presence of crosstalk currents between the contact pads resulted from water penetration into the connector. The leakage and crosstalk currents were measured daily using a pico-ammeter (Model 6485, Keithley Instruments, Inc., OH, USA) with 2 V of DC bias voltage. Switching boards were used to change the conductor lines being under measurement and the current mode between the leakage & crosstalk current (Figure 2.21). LabView-based software was used to control the pico-ammeter with a GPIB controller (GPIB-USB-HS, National Instruments, TX, USA). The failure criterion (threshold level) of the connector samples was set to one hundredth of the maximum leakage current level [108, 109].

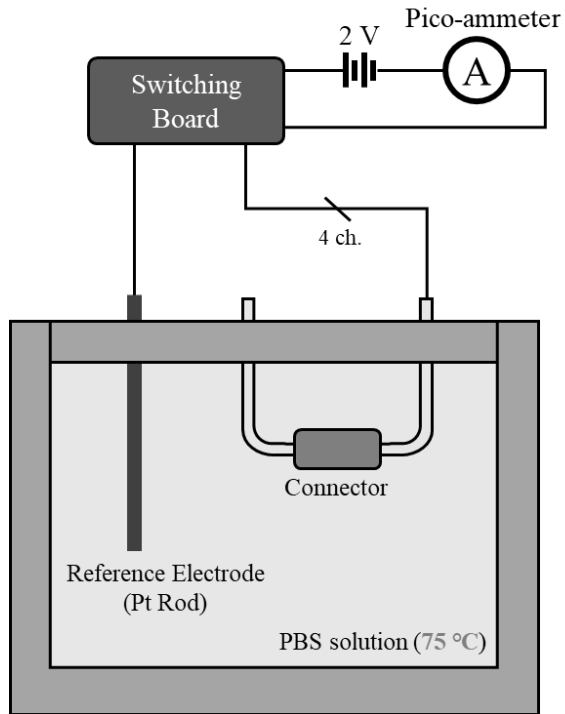


Figure 2.20 *In vitro* leakage test setup. Sample groups are immersed in PBS solution at 75 °C. Leakage and crosstalk current are measured using a pico-ammeter and a switching board for changing of measurement mode.

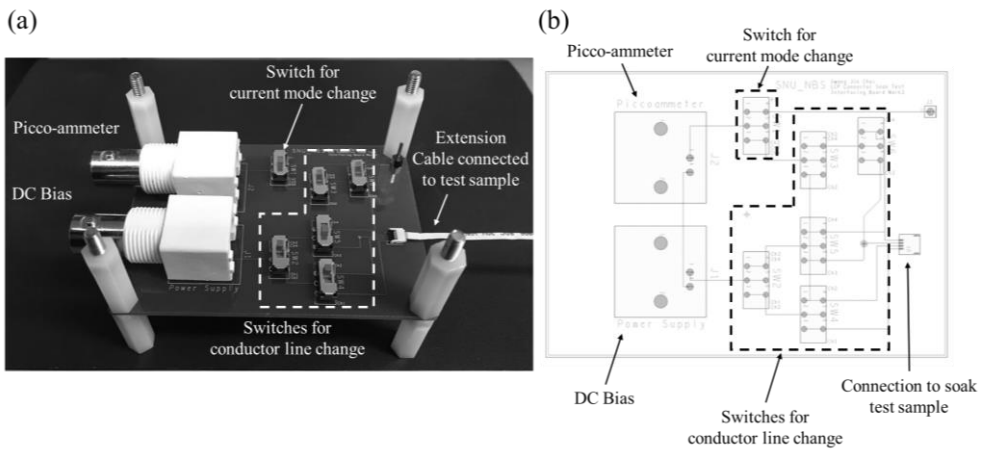


Figure 2.21 Switching board with switches for line and mode conversion. (a) Photograph of the switching board. (b) Outline of the switching board.

The threshold level can be determined theoretically by modeling the different impedances involved in the stimulation path. Figure 2.22 shows the equivalent circuits of connector channels with leakage and crosstalk current. In these models, $Z_{\text{Electrode}}$ represents the interface impedance, Z_{Shunt} the wire shunt impedance to ground, Z_{Seal} the sealing impedance to the outer solution, and Z_{Coupling} the coupling impedance between two channels due to the leakage. Assuming $Z_{\text{Shunt}} \gg Z_{\text{Electrode}}$ and 1% crosstalk is considerable, the stimulation current (I_1) and the crosstalk current (I_2) have the following relationship:

$$I_2 < \frac{I_1}{100} = \frac{V_{\text{in}}}{100 \times Z_{\text{Electrode}}}$$

Based on the same 1% criterion, the leakage current (I_3) is also limited as follow:

$$I_3 < \frac{I_1}{100} = \frac{V_{\text{in}}}{100 \times Z_{\text{Electrode}}}$$

Thus, the threshold level of the leakage and crosstalk current is determined by the $Z_{\text{Electrode}}$. In this study, it was assumed that an electrode with a gold site having the same area of the contact pad of the cable is used.

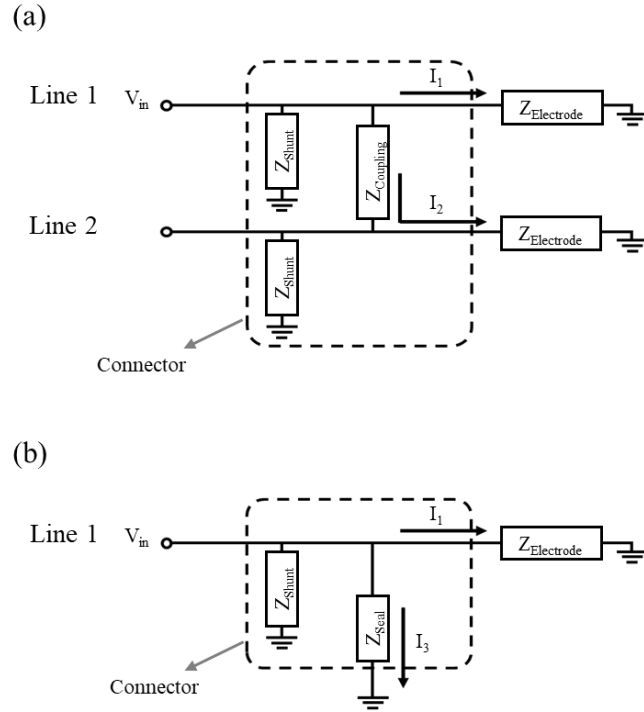


Figure 2.22 Equivalent circuits of (a) two parallel conductor lines for crosstalk current model and (b) a conductor line for leakage current model. Conductor lines of the same length and width are assumed.

If the mean time to failure (MTTF) of the test groups is measured at the accelerated temperature, the lifetime at the body temperature (37°C) can be estimated by the following common ten-degree rule.

$$f = 2^{\frac{\Delta T}{10}}, \text{ where } \Delta T = T - T_{ref}$$

f: increased rate of aging

T: elevated temperature (75°C)

T_{ref} : reference temperature (37°C)

Chapter III

Results

3.1 CNT Bundle-based Thin Intracochlear Electrode Array

3.1.1 Fabricated Electrode Array

The fabricated CNT bundle-based intracochlear electrode array is shown in Figure 3.1. The surface of the CNT bundle was electroplated with gold (10 μm thick) to protect the electrode sites during the laser ablation of insulation layers. After parylene C layer was conformally coated on the surface of the bundles, each electrode site was exposed through laser ablation. Finally, eight different CNT bundles were aligned at fixed spatial intervals (2 mm) and encapsulated with the silicone elastomer. The average cross-sectional dimensions of the CNT bundle are approximately $115 \mu\text{m} \times 9.94 \mu\text{m}$ (Figure 3.2). The exposed electrode sites by laser ablation have a length of 0.5 mm and the width of each bundle (average electrode site area of 0.073 mm^2). The developed CNT bundle-based intracochlear electrode array consisting of eight CNT bundles has maximum diameters, or thicknesses, of $135 \mu\text{m}$ and $395 \mu\text{m}$ at the apex and the base, respectively. Because the CNT bundle has the ribbon-shape, the maximum thickness is considered in this study. Despite the manual fabrication with the CNT bundles and encapsulation of the silicone elastomer, the proposed electrode array is significantly thinner than conventional intracochlear electrode arrays (Table 3.1) [7, 14, 45-47]. For comparison with the thinnest conventional intracochlear electrode array, Slim Straight (Cochlear, Australia), the thickness of 22-channel CNT bundle-based electrode array is estimated. The proportionally estimated thickness of the CNT bundle-based electrode array with the 22 channels is $915 \mu\text{m}$. The CNT bundle-based electrode array has a thickness more than two times less than Slim Straight at its apex.

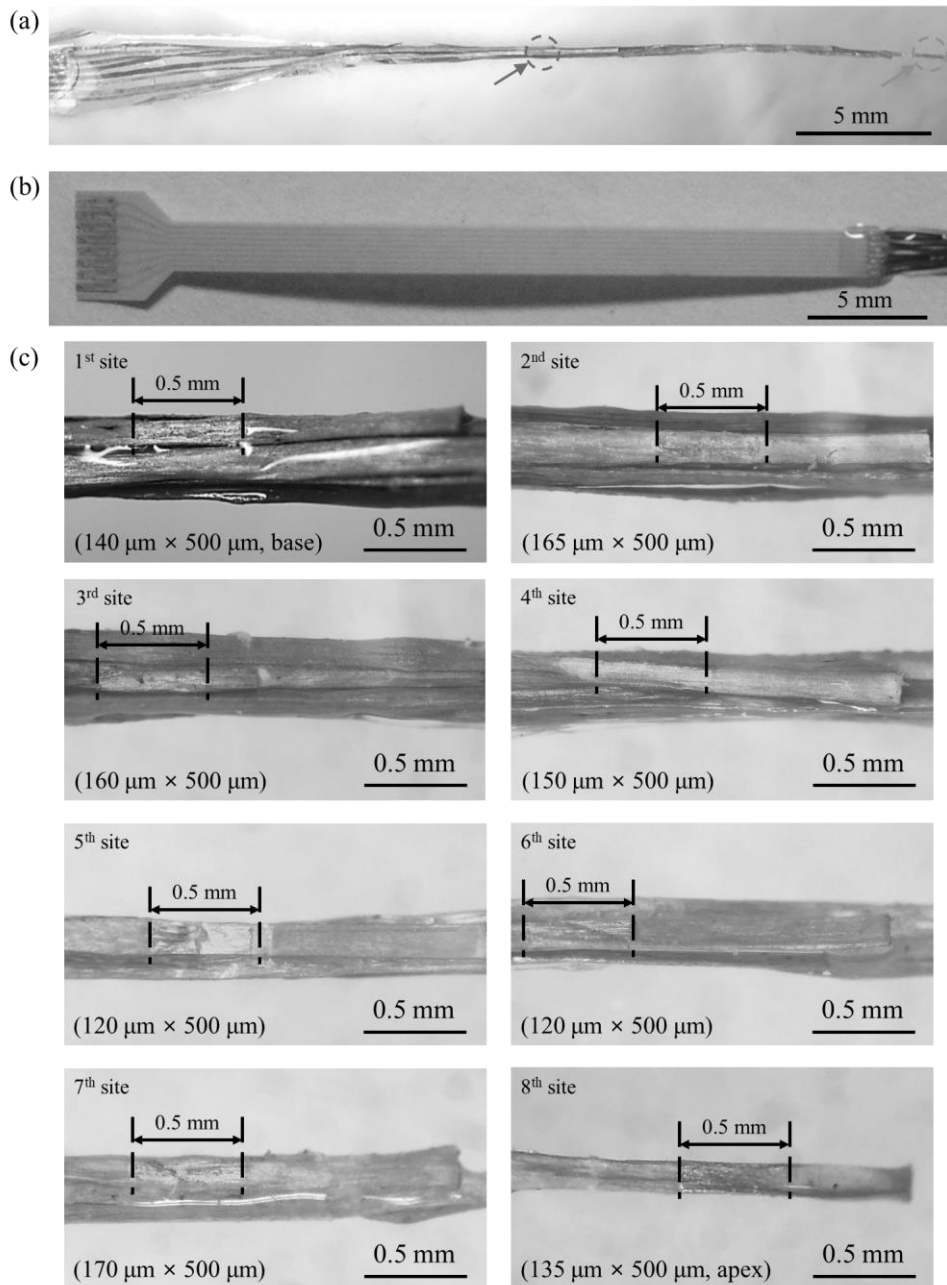


Figure 3.1 CNT bundle-based intracochlear electrode array. (a) Photograph of the fabricated intracochlear electrode. Arrows at left and right indicate electrode sites at its base and apex, respectively. (b) LCP-based electrode lead (c) Electrode sites from base (1st site) to apex (8th site). Bidirectional arrows indicate each corresponding electrode site.

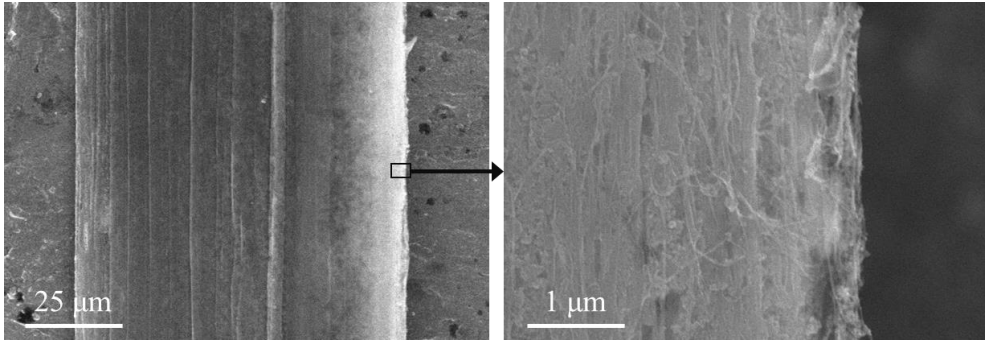


Figure 3.2 SEM images of CNT bundle with numerous CNTs entangled.

Table 3.1 Manufacturers and dimensions of intracochlear electrode arrays [7, 14, 45-47].

<i>Manufacturer</i>	<i>Electrode Array</i>	<i>Apex (mm)</i>	<i>Base (mm)</i>	<i>Number of Channels</i>
Adv. Bionics	HiFocus 1J	0.4	0.8	16
Cochlear	Contour Advance	0.5	0.8	22
Cochlear	Slim Straight	0.3	0.6	22
Med-El	Standard	0.5	1.3	12
Med-El	Flex (20, 24, 28)	0.5/0.3	0.8	12
Nurobiosys	Nurobiosys	0.5	0.7	16
This study	-	0.135	0.395	8
This study (*: estimated)	-	0.135	0.915*	22

3.1.2 Insertion and Extraction Force in Scala Tympani Model

To quantitatively assess the force exerted by the CNT bundle-based intracochlear electrode array on the cochlea, the insertion and extraction forces in the plastic human ST model were measured (Figure 3.3). For comparison, the insertion and extraction forces of the 8-channel Pt/Ir wire-based dummy electrode array were also measured (inter-channel distance: 2 mm, electrode diameter: 0.3 mm at the apex and 0.75 mm at the base). During the entire insertion process, the CNT bundle-based intracochlear electrode array was inserted smoothly into the helical structure of the human ST model and exerted smaller forces than the metal wire-based dummy electrode array (Figure 3.4 and Figure 3.5). For example, the insertion force of the CNT bundle-based electrode array was 0.343 mN, at 8 mm from the round window (entrance of cochlea), and the maximum extraction force was approximately 8.07 mN. In contrast, for the metal wire-based electrode array that has the same number of channels, the insertion force at 8 mm displacement was 2.09 mN and the maximum extraction force was 72.3 mN. For both insertion and extraction, the CNT bundle-based electrode array required smaller forces compared to the metal wire-based intracochlear electrode array.

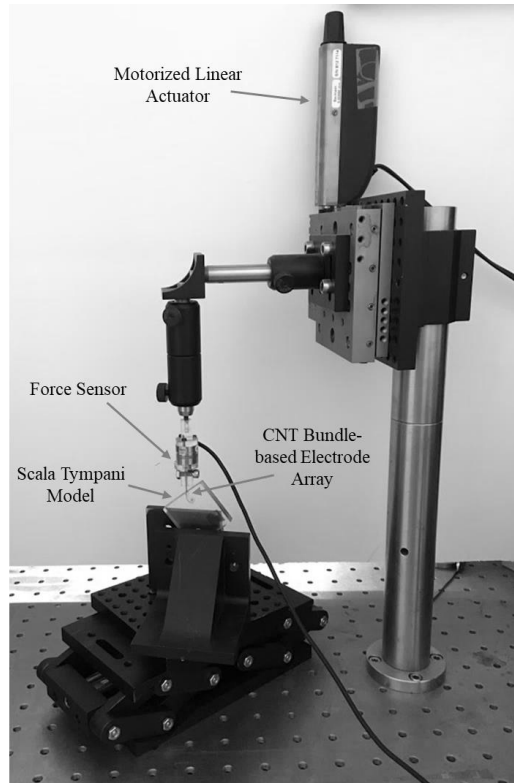


Figure 3.3 Experimental setup of insertion and extraction force measurements of 8-channel CNT bundle-based intracochlear electrode array in scala tympani model.

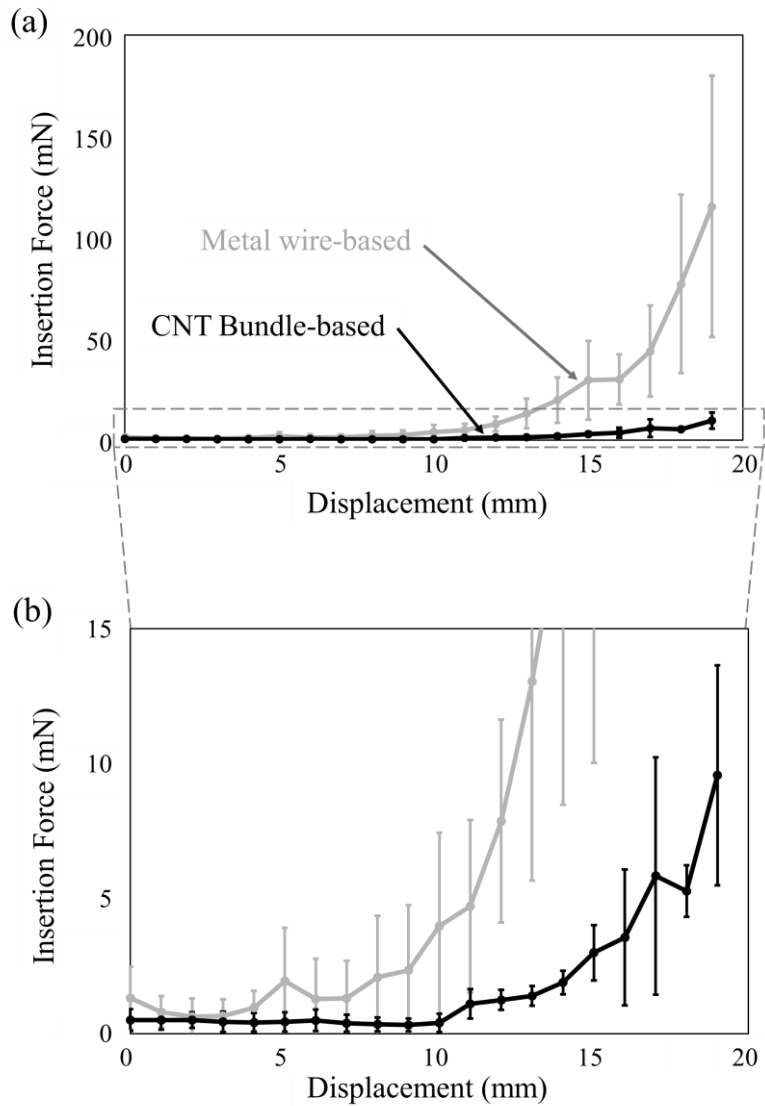


Figure 3.4 (a) Insertion force measurements of 8-channel CNT bundle-based intracochlear electrode array and metal wire-based dummy electrode array. (b) Enlarged view of a dashed rectangle portion in (a). Average and standard deviation of measured values are shown.

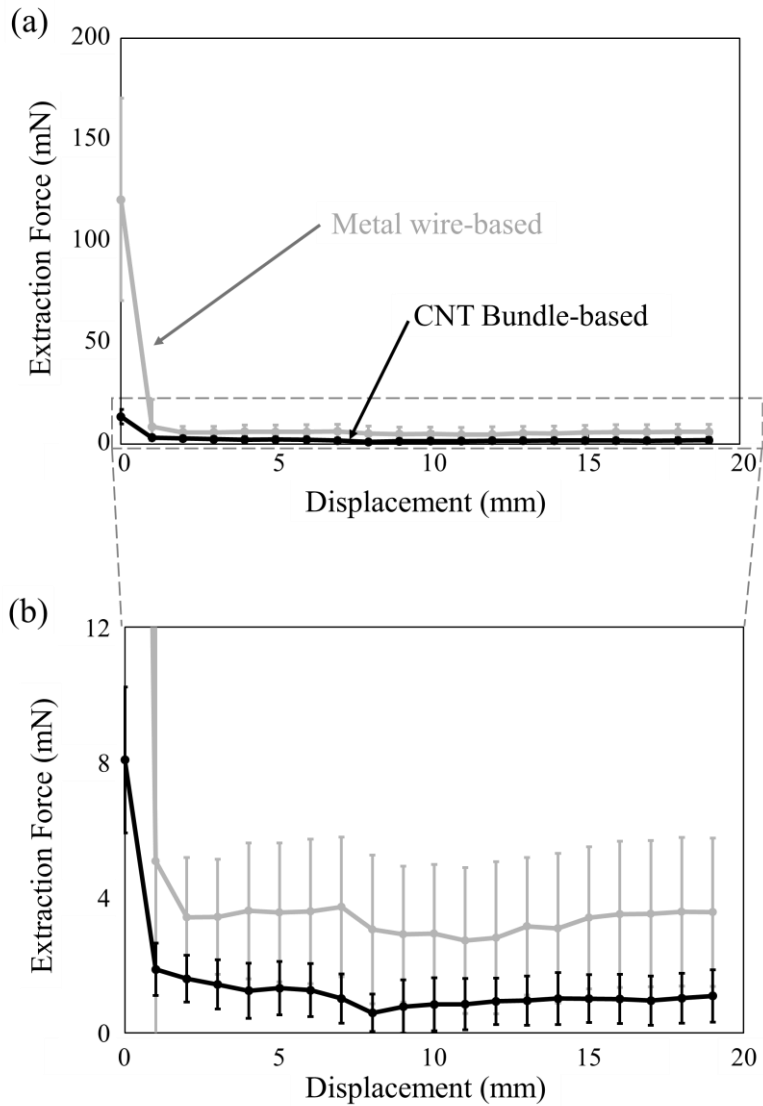


Figure 3.5 (a) Extraction force measurements of 8-channel CNT bundle-based intracochlear electrode array and metal wire-based dummy electrode array. (b) Enlarged view of a dashed rectangle portion in (a). Average and standard deviation of measured values are shown.

3.1.3 Simulation of Horizontal and Vertical Deflection

Figure 3.6 shows the stiffness simulation results of the CNT bundle-based electrode array according to directions of deflection. The obtained stiffnesses in the horizontal and vertical direction were 9.03 N/m and 24.7 N/m, respectively. According to the simulation, the developed electrode array showed better flexibility in the horizontal direction than in the vertical direction. However, the stiffness of the metal wire-based dummy electrode array was calculated as 22.8 N/m, which is a lower value than that of the CNT bundle-based electrode array in the horizontal direction.

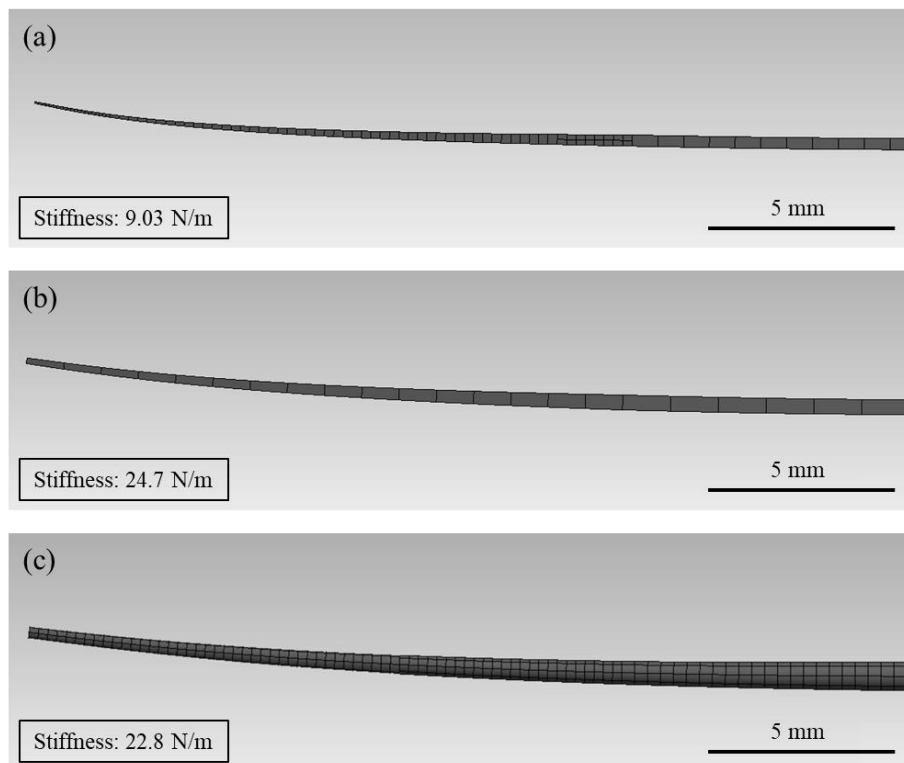


Figure 3.6 Simulation results of (a) horizontal and (b) vertical stiffness of CNT bundle-based electrode array. (c) Simulation result of metal wire-based dummy electrode array.

3.1.4 Electrochemical Characteristics

To evaluate the electrochemical characteristics of the electrode array, the EIS and CV were measured as described in the section 2.1.3.2. Generally, lower impedance and higher CSCc indicate that more electrical charges can be delivered to target nerves through electrode sites. The average values of the impedance magnitude and phase angle of the electrode array were $2.70 \pm 0.756 \text{ k}\Omega$ and $-20.4 \pm 10.4^\circ$ at 1 kHz, and the average CSCc was $-708 \pm 201 \text{ mC/cm}^2$ (Figure 3.7). Before the gold electroplating, the average impedance magnitude and the average phase angle of the bare CNT bundles were $0.632 \pm 0.104 \text{ k}\Omega$ and $-28.8 \pm 16.6^\circ$ at 1 kHz, respectively, and the CSCc was $-1.28 \pm 0.306 \text{ mC/cm}^2$. Considering the measured area (1 mm^2) of the bare CNT bundles, the gold electroplating induced an approximately five-fold decrease in area-specific impedance and a five-hundred-fold increase in CSCc (Figure 3.8).

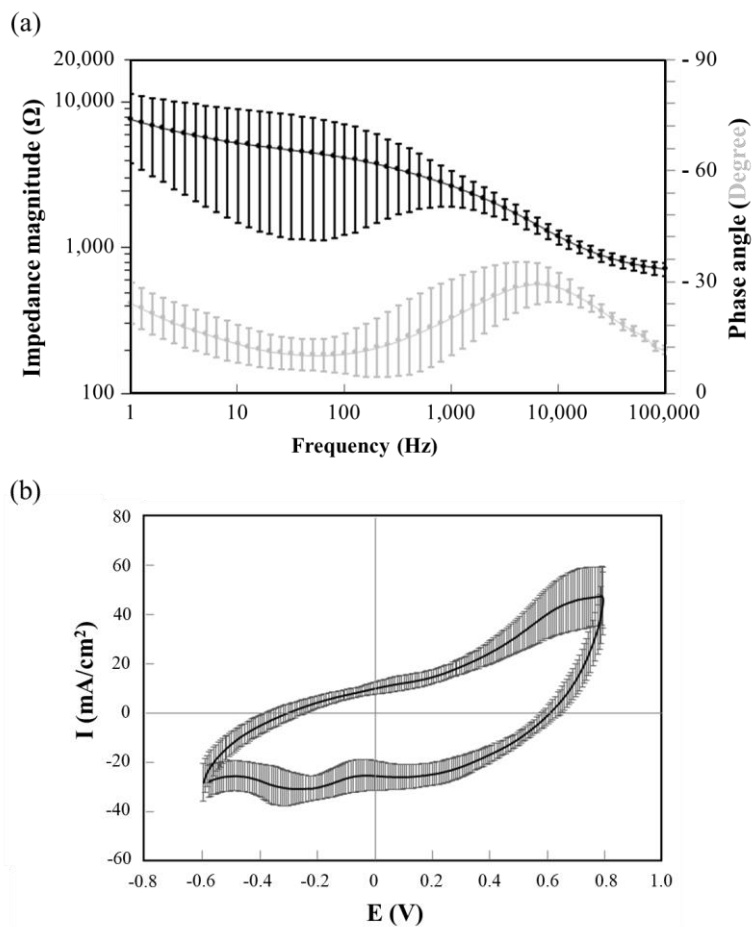


Figure 3.7 Electrochemical properties of CNT bundle-based electrode array. (a) EIS: impedance magnitude (black) and phase angle (grey) are shown over frequency. (b) CV of the electrode array is measured in the range of -0.6 – 0.8 V. Average and standard deviation of measured values are shown.

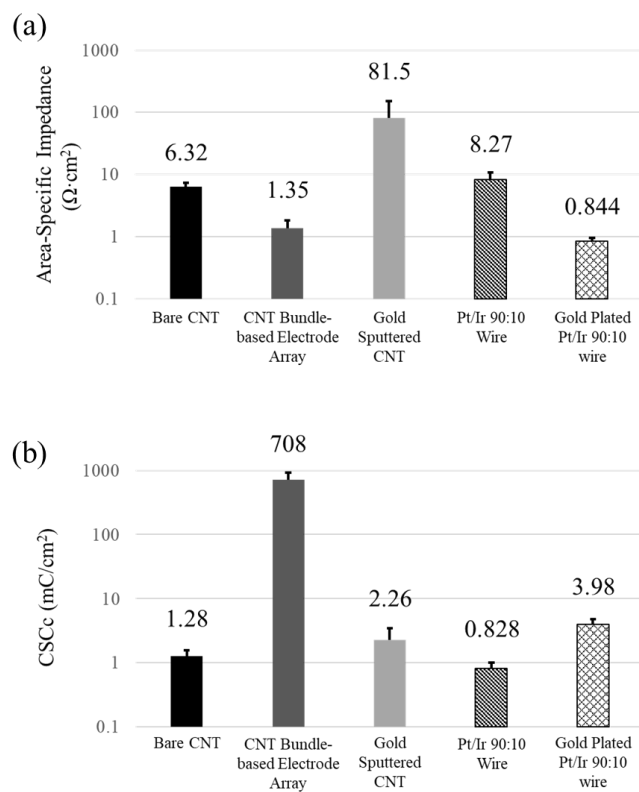
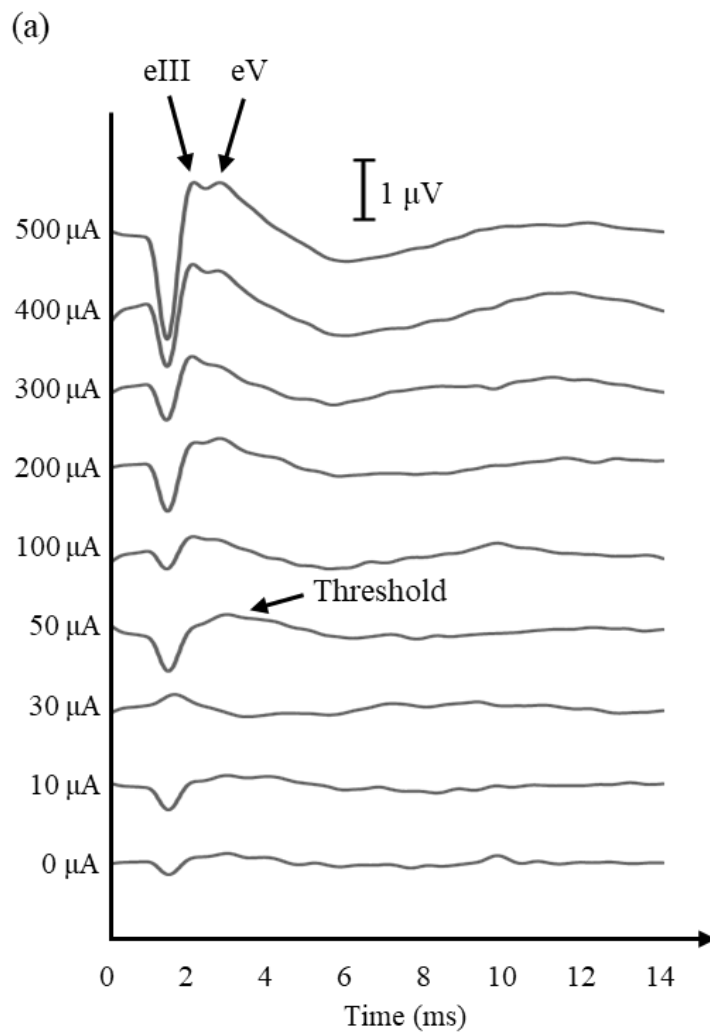


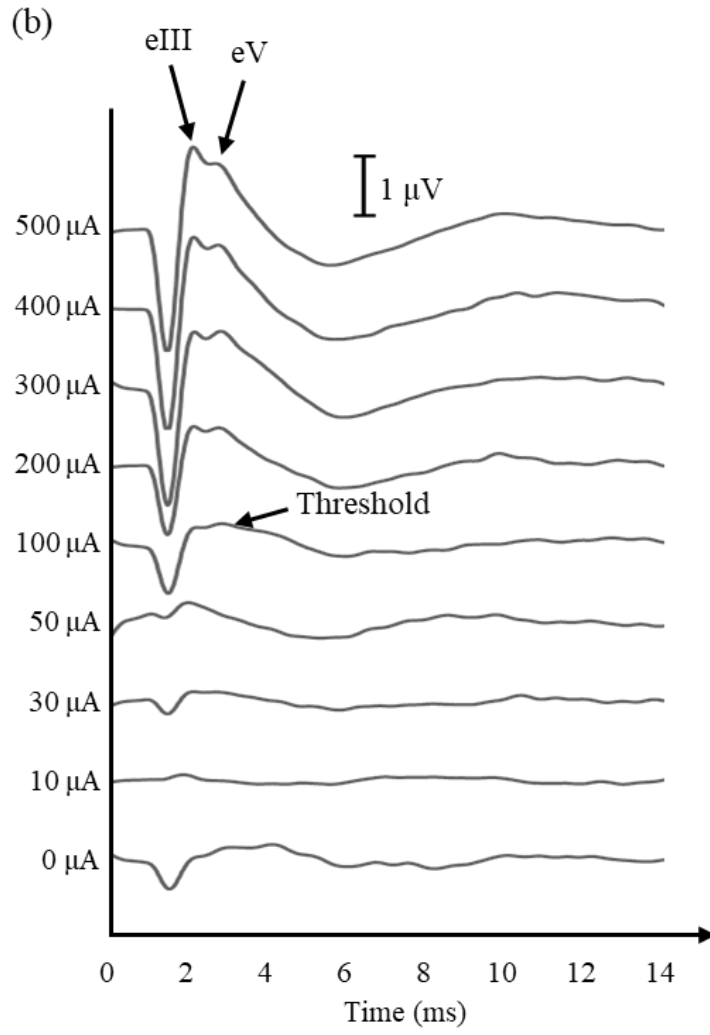
Figure 3.8 Electrochemical properties of various electrode materials. (a) Area-specific impedances and (b) CSCc magnitudes of various electrode materials are shown.

The gold-sputtered CNT bundle had $81.5 \Omega \cdot \text{cm}^2$ of area-specific impedance and -2.26 mC/cm^2 of CSCc. Also, the area-specific impedance and the CSCc of the Pt/Ir wire were $8.27 \Omega \cdot \text{cm}^2$ and -0.828 mC/cm^2 , respectively. However, after the gold electroplating, the area-specific impedance and the CSCc of the Pt/Ir wire were $0.844 \Omega \cdot \text{cm}^2$ and -3.98 mC/cm^2 , respectively.

3.1.5 Electrical Auditory Brainstem Response (eABR) Recording

The CNT bundle-based electrode array was implanted into the SD rat's cochlea and the eABR waves were obtained (Figure 3.9). Owing to the SD rat's cochlear length (approximately 7 mm), which is shorter than that of a human, only the first three electrode sites at the tip (approximately 5 mm in length) were inserted into the cochlea, and the remaining channels were retained outside [110]. Therefore, electrical current pulses were engaged to nerve cells through the electrode sites, and the eABR waves were recorded at different levels of electrical current. The recorded eABR responses showed different waveforms as the magnitude of the electrical current stimulation varied from $0 \mu\text{A}$ to $500 \mu\text{A}$. Especially, the waves III and V were observed in the recorded eABR waves above the $50 \mu\text{A}$, $100 \mu\text{A}$, and $30 \mu\text{A}$ current stimulation levels at 1st, 2nd, and 3rd electrode sites, respectively.





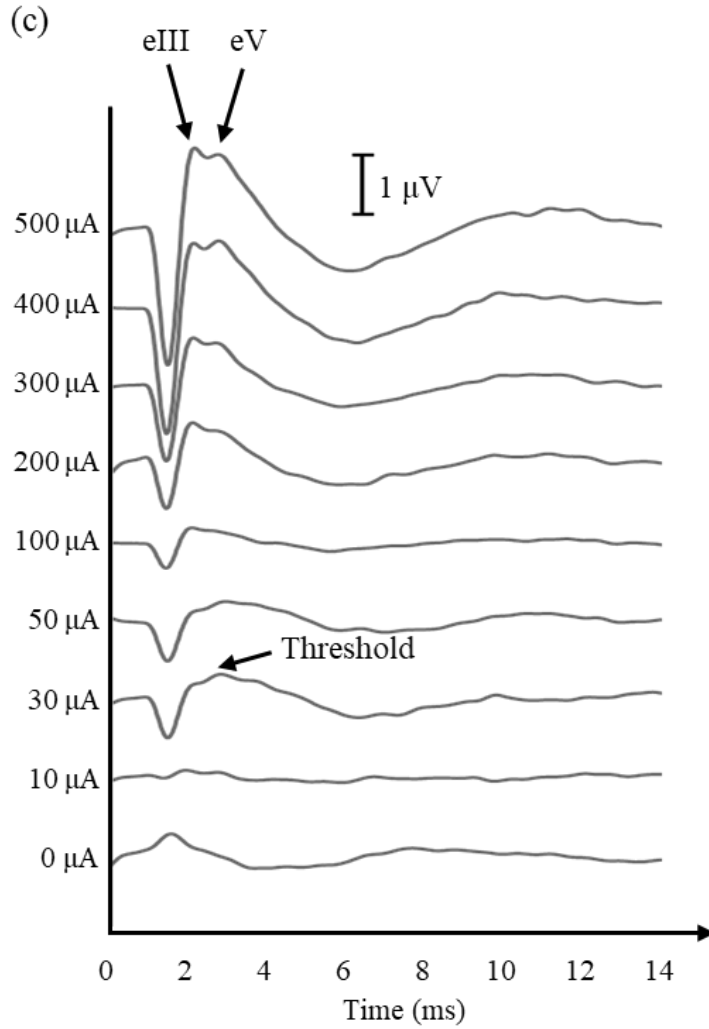


Figure 3.9 Recorded eABR waves at (a) 1st, (b) 2nd, and (c) 3rd electrode sites. The recorded eABR voltage waveforms corresponding to different magnitudes of electrical stimulation current are combined in each graph.

3.2 Implantable Multi-channel Connector

3.2.1 Fabricated Connector

The fabricated LCP-based connector and the cable are shown in Figure 3.10. The developed LCP connector have a gap of 400 μm thick and a wall of 350 μm thick. The bump structures inside the bidirectional connector have a 100 μm radius, and four & eight contact pads are on the opposite sides. The LCP cables were also fabricated to have the same number of conductor lines as the LCP connectors. The cables have two parts with different thicknesses; the thick insertion part inserted into the connector has a thickness of 450 μm and the thin & flexible lead part has a thickness of 250 μm . Two cables were inserted into each side of the bidirectional connector, and the electrical connections were confirmed at all conductor lines.

Figure 3.11 shows the metal cases which have spaces for the block and ring-shape packings. The ring-shape packing was designed to be 100 μm thicker than the groove in the metal case to fill the gap between the joint of the metal cases. In addition, the block-shape packing was made in larger volumes than the internal space of the metal case. As each block-shape packing was fastened into the cable, the clamping force was applied by the metal case wall to close and seal the gap between the cable and the connector. The ring-shape packing was also located between the metal cases and clamped when the connector was assembled by threads located on the metal cases. After the assembly with the metal cases, the connector has a diameter of 6 mm and a length of 17 mm.

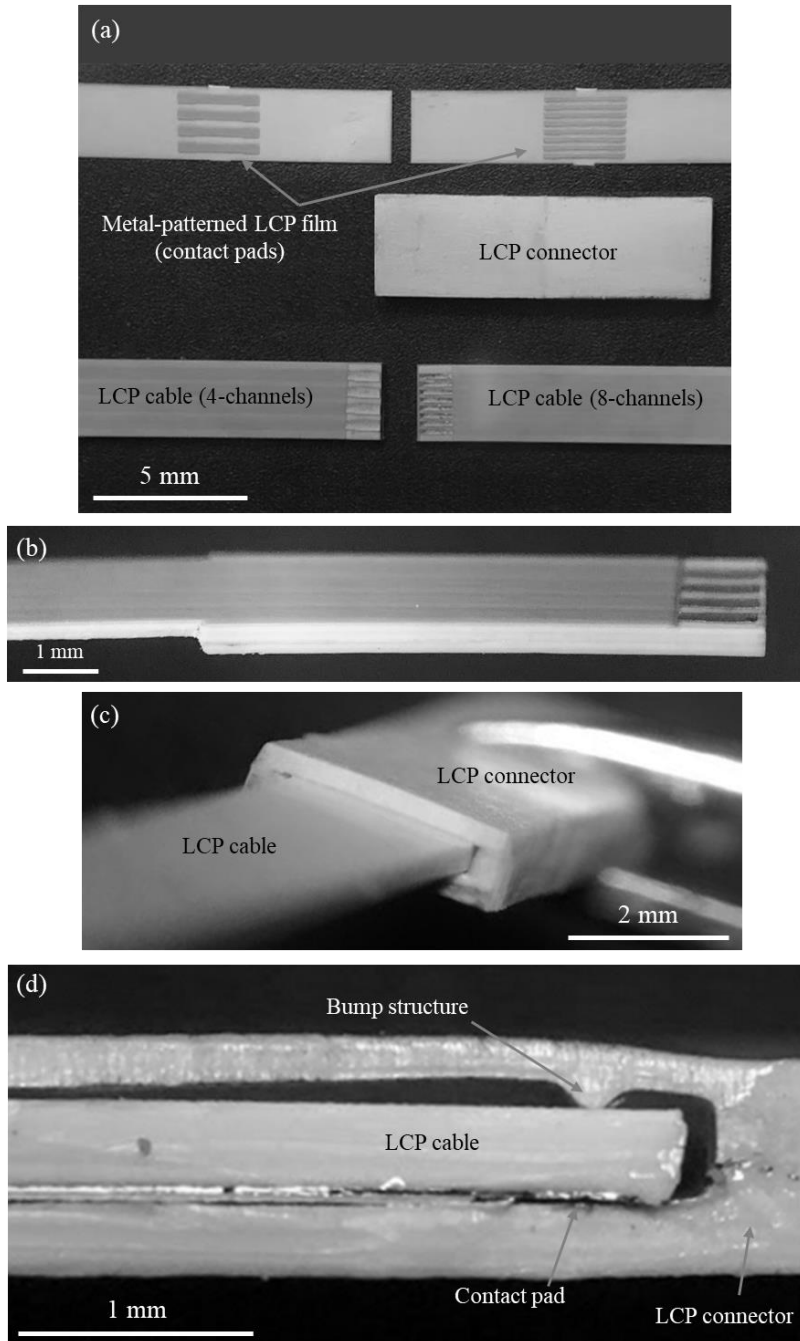


Figure 3.10 (a) Fabricated 4 & 8-channel LCP connector and cable. Contact pads with a width of $300\ \mu\text{m}$ (4-channel) and $150\ \mu\text{m}$ (8-channel). (b) Side view of the 4-channel LCP cable: thick insertion part inserted into the connector with a thickness of $450\ \mu\text{m}$ and thin lead part with a thickness of $250\ \mu\text{m}$. (c) The LCP connector and inserted LCP cable. (d) Cross-sectional view of the LCP connector and cable. The bump structure applying the contact pressure to the contact pads.

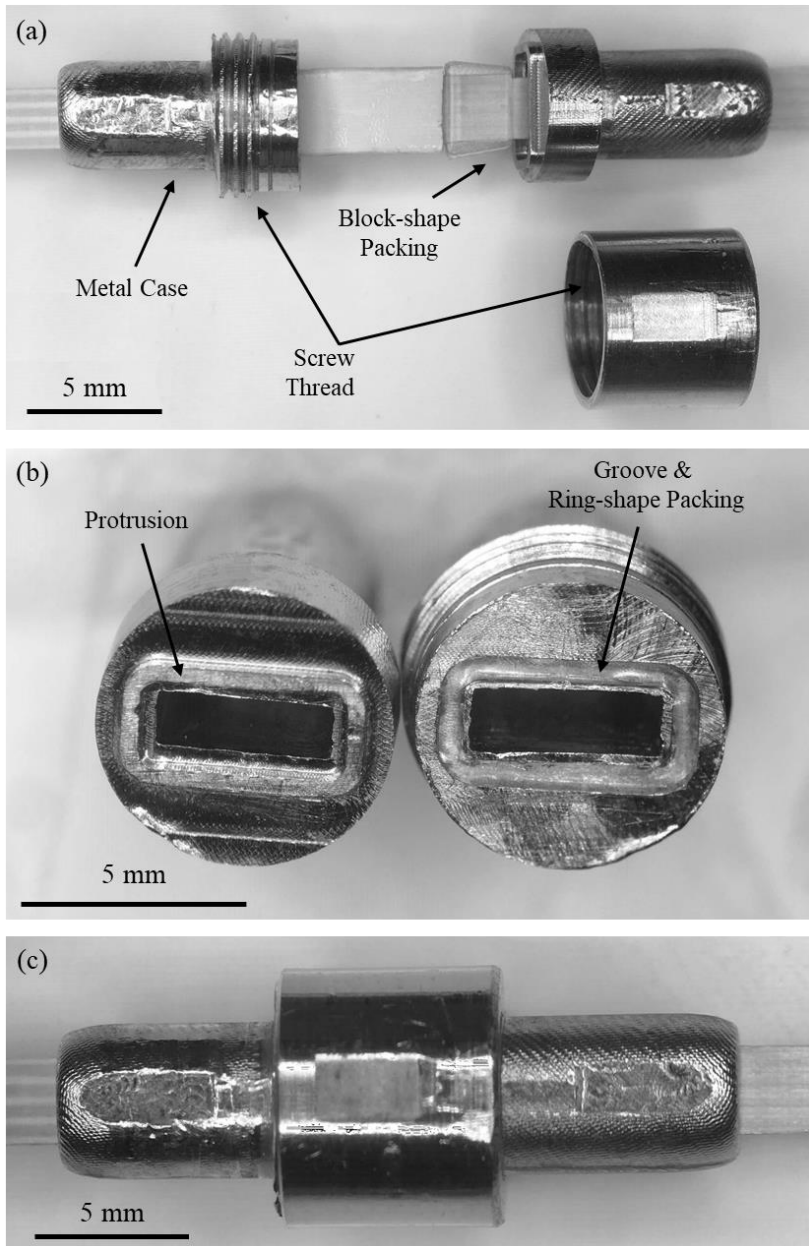


Figure 3.11 (a) LCP-based connector, cable, and metal cases. (b) Protrusion and groove structure of the metal cases with a width of $400\ \mu\text{m}$. Ring-shape packing is located at the groove of the metal case. (c) the assembled connector with the metal cases.

3.2.2 Measurement of Contact Resistance

Figure 3.12 shows plots of the assembled connector resistance versus the length of the conductor line obtained from the 4-channel and 8-channel connectors. In the limit of the zero-length ($L = 0$ mm), the contact resistances of the 4-channel and 8-channel connectors were $53.2 \text{ m}\Omega$ and $75.2 \text{ m}\Omega$, respectively.

3.2.3 Repeated Measurements of Electrical Characteristics

Each time the cables were inserted into the four and eight-channel connectors, the assembled connector resistances, resistances at both ends of the cables, were measured. At first connection, the average resistances were $1.01 \text{ }\Omega$ for the four-channel connector and $1.85 \text{ }\Omega$ for the eight-channel connector. The contact resistances were calculated at each repeated connection. After 50 cycles, there was no significant change in measured resistance (Figure 3.13). Also, there was no apparent damage to the contact pads of the connectors and cables after the repeated tests.

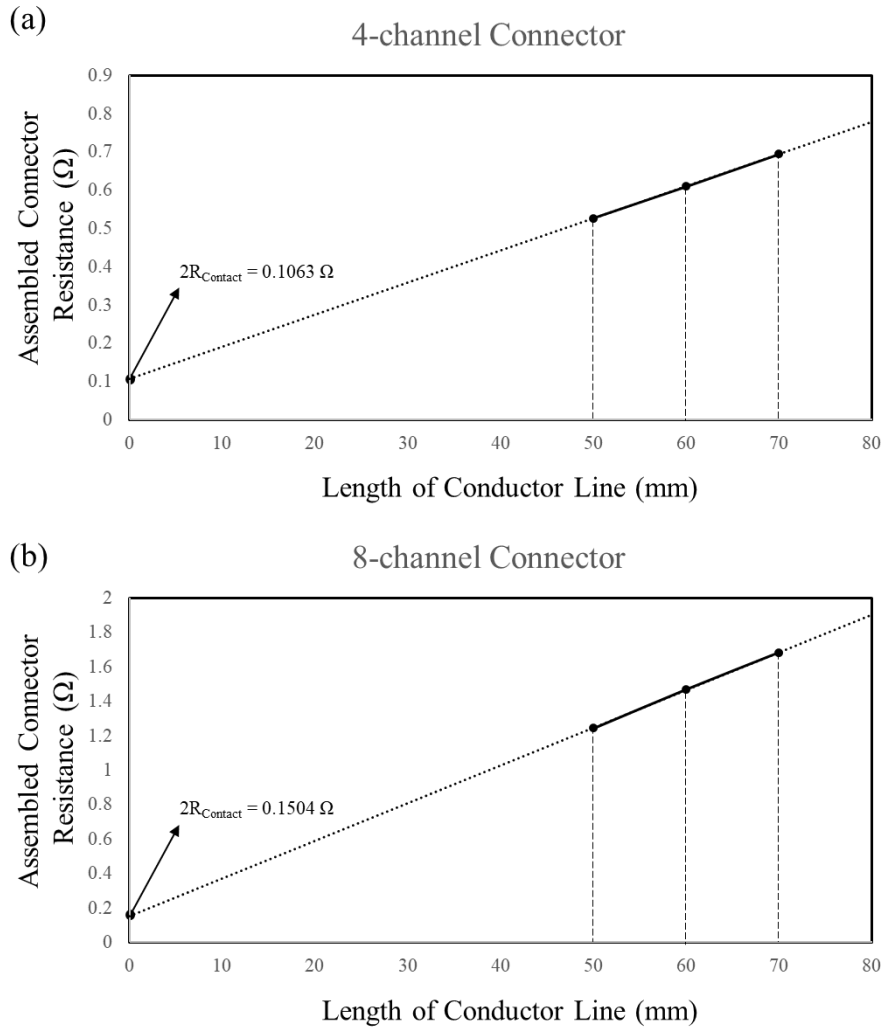


Figure 3.12 Assembled connector resistance of (a) 4-channel connector and (b) 8-channel connector with 50, 60, and 70 mm of conductor line length. Contact resistances are obtained in the limit of the zero-length ($L = 0$ mm).

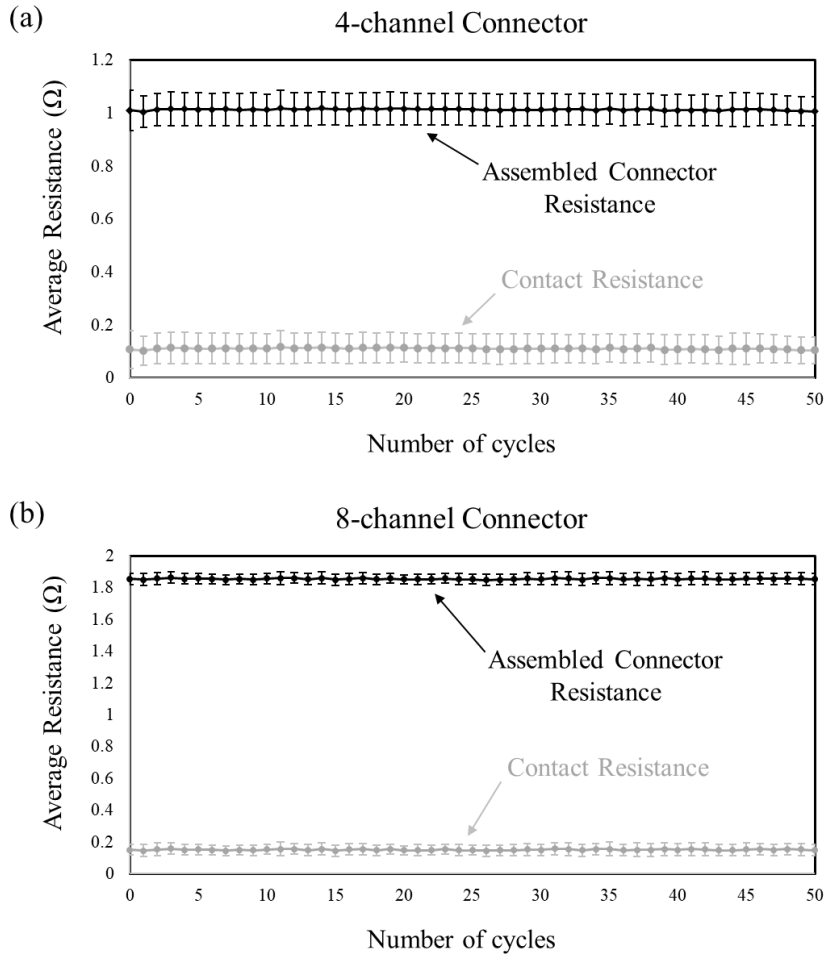


Figure 3.13 Repeated resistance measurements of the fabricated LCP connector. Average and standard deviation of measured resistances are shown.

3.2.4 Accelerated Soak Test and Lifetime Estimation

The leakage and crosstalk currents were measured under the 75°C soak test of the four-channel connector sample groups using different designs of the block-shape packing. To compare with other sealing methods, the currents from connector samples, which were sealed only by covering dental resin (Charmfil Flow A3, ELI-DENT Group SpA, Fiorentino, Italy) or curing silicone elastomer around the connector, were also measured in the same accelerated soak test (Figure 3.14) [107].

The stimulation current (I_1) measured using the gold electrode, which has the same site area ($0.3 \text{ mm} \times 1 \text{ mm}$) as the cable contact pad, was $73.1 \text{ } \mu\text{A}$, and the threshold level was decided by 1% of the stimulation current (threshold level = $0.731 \text{ } \mu\text{A}$). Figure 3.15 shows the maximum values of the leakage and crosstalk currents measured in each channel of the sample groups. The time of device failure was determined when either the leakage current or the crosstalk current exceeded the threshold level. The MTTF due to water penetration into the connector was 2 days for the resin sealing and 25 days for the silicone elastomer sealing. For the connector groups using the block-shape packings having 125 %, 137 %, and 150 % volume ratios to the internal space of the metal case, water penetration occurred in 14 days, 79 days, and 14 days. If the ten-degree rule is applied, the estimated lifetimes of the five groups are approximately 27, 347, 194, 1098, and 194 days, respectively.

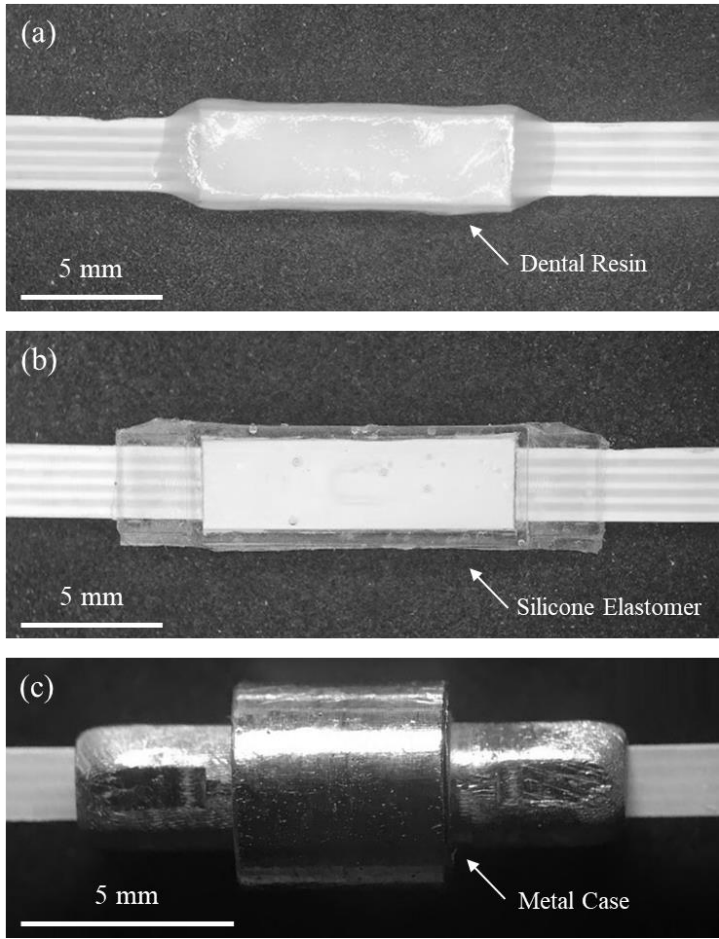
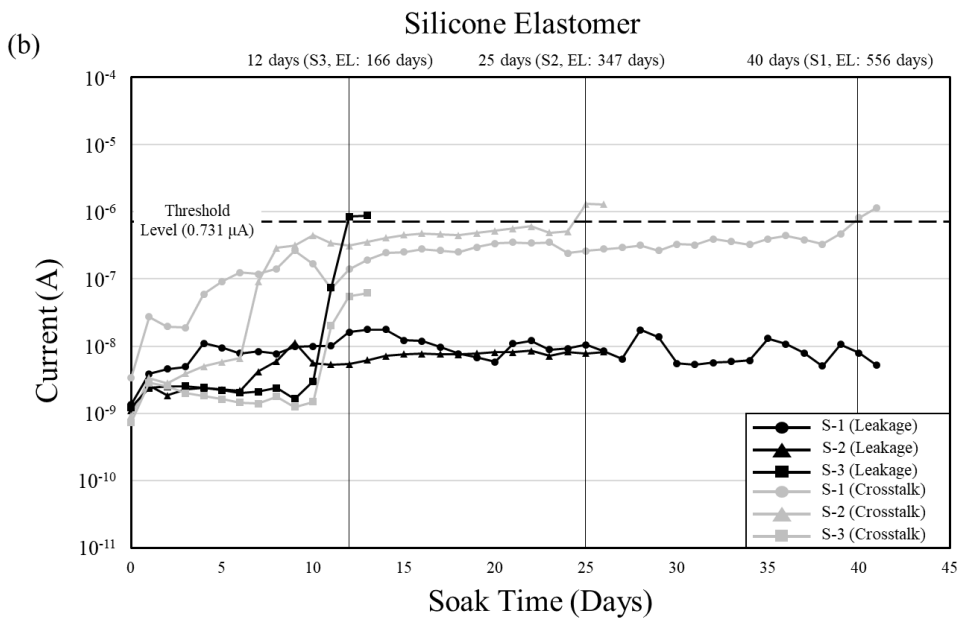
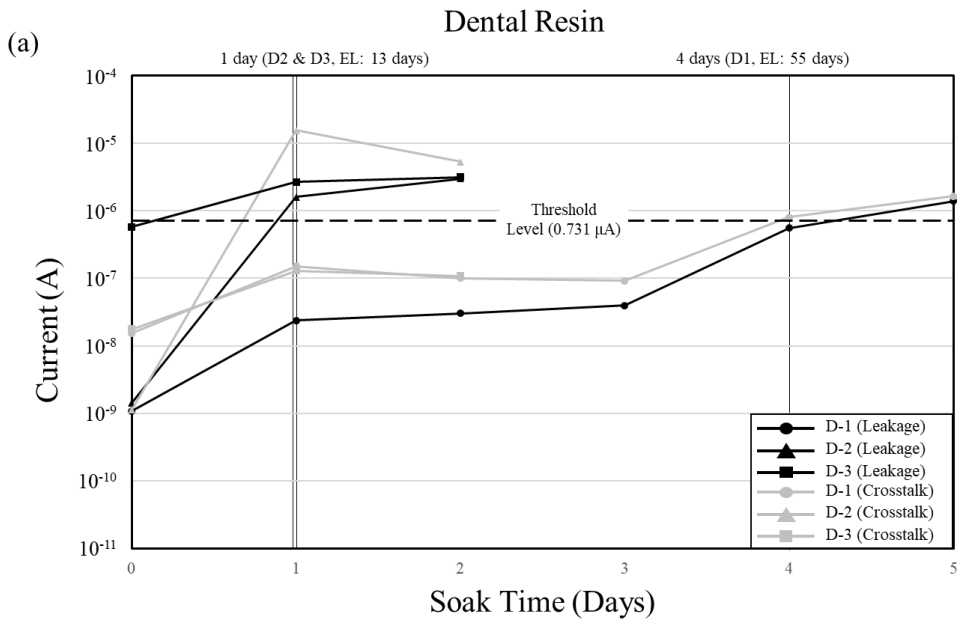
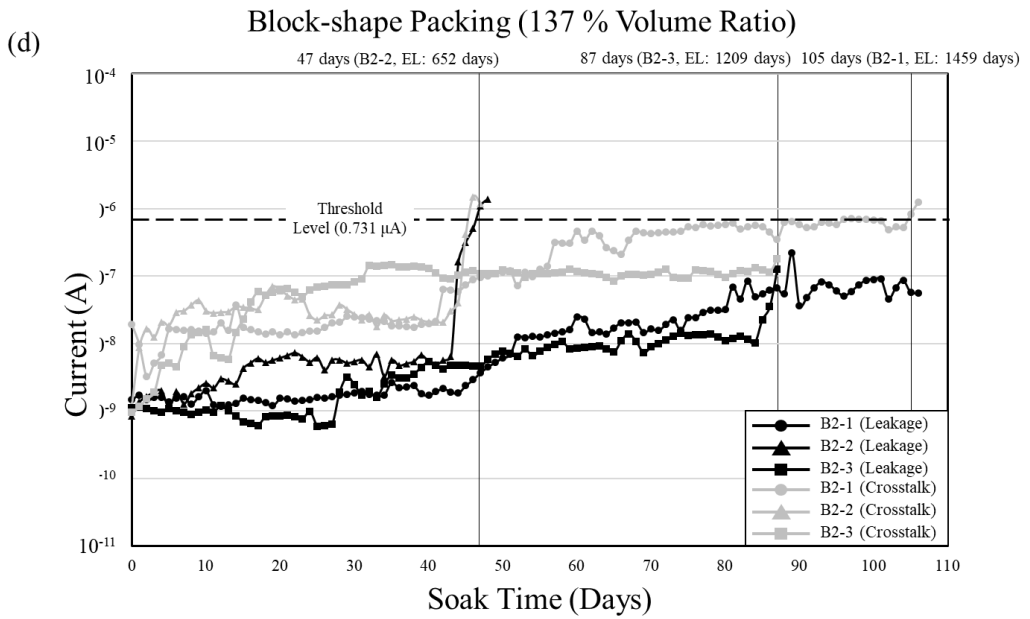
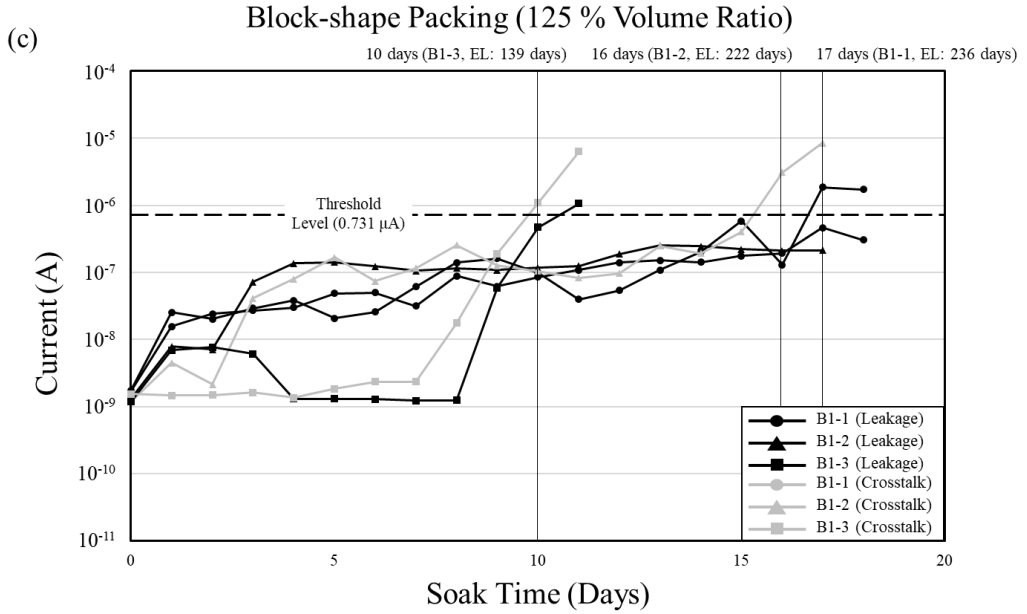


Figure 3.14 Four-channel connector samples sealed with (a) dental resin, (b) silicone elastomer, and (c) metal cases & packings. The thickness of the covered dental resin and silicone elastomer is 0.5 mm.





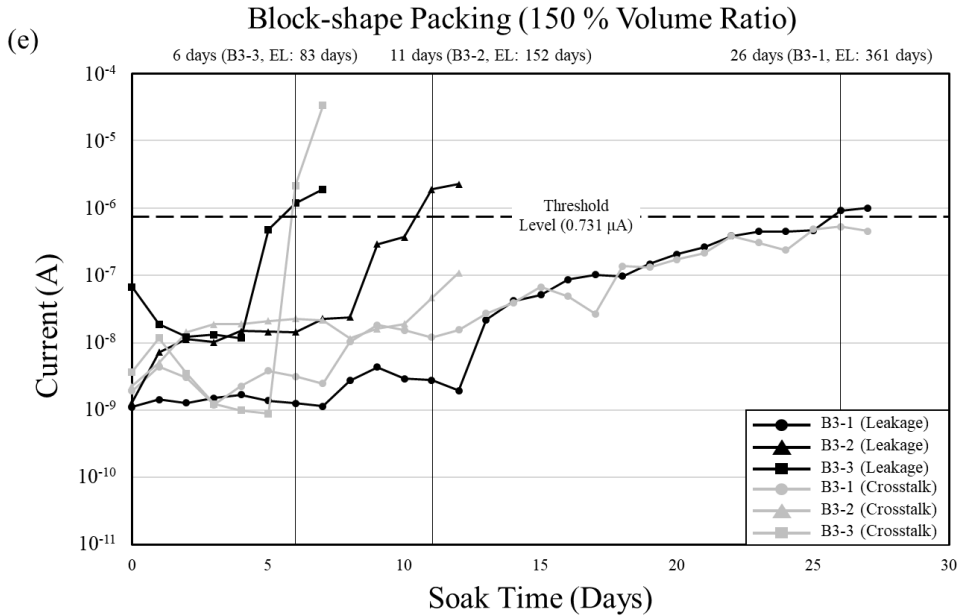


Figure 3.15 Leakage and crosstalk current measurements during the *in vitro* accelerated soak test. Connector samples sealed with (a) dental resin (D-1, D-2, and D-3) and (b) silicone elastomer (S-1, S-2, and S-3). Connector samples assembled with metal cases and block-shape packings having (c) 125 % (B1-1, B1-2, and B1-3), (d) 137 % (B2-1, B2-2, and B2-3), and (e) 150 % (B3-1, B3-2, and B3-3) volume ratios. (Threshold level: 0.731 μ A, EL: estimated lifetime, Measurement of B2-3 is still in progress)

Chapter IV

Discussion

4.1 CNT Bundle-based Intracochlear Electrode Array

4.1.1 Comparison of Proposed Electrode Array to Conventional Devices

It is essential to make an intracochlear electrode array thinner and more flexible, which can reduce the insertion trauma in the cochlea and preserve the function of residual hair cells after the implantation [17]. In this study, a new conducting material, CNT, is applied to reduce the size and the stiffness of an electrode array. The electrochemical properties indicate that the new material is suitable for stimulating intracochlear electrode after the gold electroplating on the surface of the CNT bundle. Despite the manual encapsulation of the CNT bundles using the silicone elastomer, the proposed electrode array has a significantly smaller thickness than conventional intracochlear electrode arrays (Figure 3.1). The developed CNT bundle-based intracochlear electrode array consists of eight CNT bundles and has thicknesses of 135 μm and 395 μm at the apex and the base, respectively. For comparison to conventional intracochlear electrode arrays with higher channel numbers, the thickness of the CNT bundle-based electrode array at the base is linearly estimated in terms of the channel number. The thickness of the 22 channel CNT bundle-based electrode array, proportionally estimated by the measured thicknesses, is 915 μm at the base (Figure 4.1). The estimation shows that the proposed intracochlear electrode array could have a similar thickness at the base compared with commercially available electrode arrays (Table 3.1). Also, because the intracochlear electrode array is inserted into the tapered cochlea, the thickness of the electrode array at the apex is closely related to the atraumatic insertion. Slim Straight electrode, which is the thinnest conventional electrode array, has a diameter

of 300 μm at the apex. The CNT bundle-based intracochlear electrode array has a thickness more than two times less than Slim Straight at its apex, which can be advantageous for minimizing the insertion trauma.

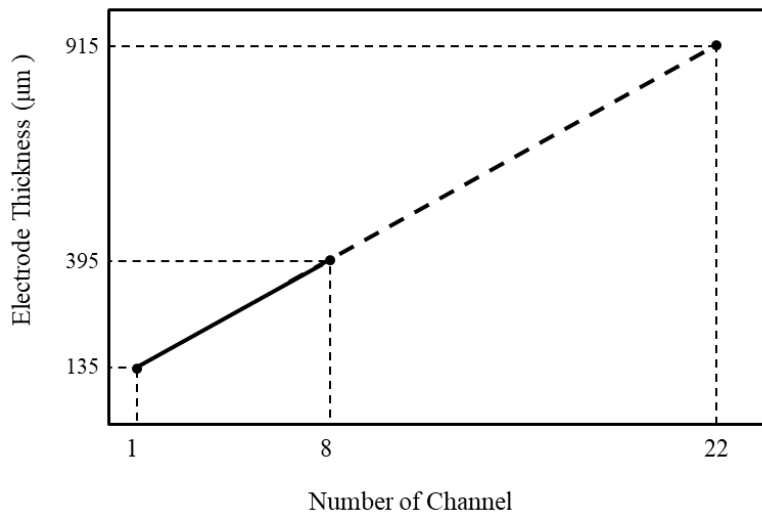


Figure 4.1 Linear estimation of the proposed electrode array. The thickness of the 22 channel CNT bundle-based electrode array is estimated based on the thicknesses at the apex (135 μm) and the base (395 μm).

The high enhancements of the electrochemical properties appear to be related to the changes in the surface condition after the gold electroplating. The electrochemical properties of the CNT bundle were significantly enhanced after the gold electroplating (Figure 3.8). The enhancement of the electrochemical properties could be results of the large effective surface area of the electrode array. The SEM images shown in Figure 3.2 and Figure 4.2 indicate that a large amount of minute grains of gold particles (diameter appears to be approximately 500 nm) was formed on the surface and possibly in-between the CNT bundles. As a result, the surface of the gold electroplated CNT bundle becomes highly porous and this could result in a

substantial decrease in the impedance and increase in the CSC value [111-113].

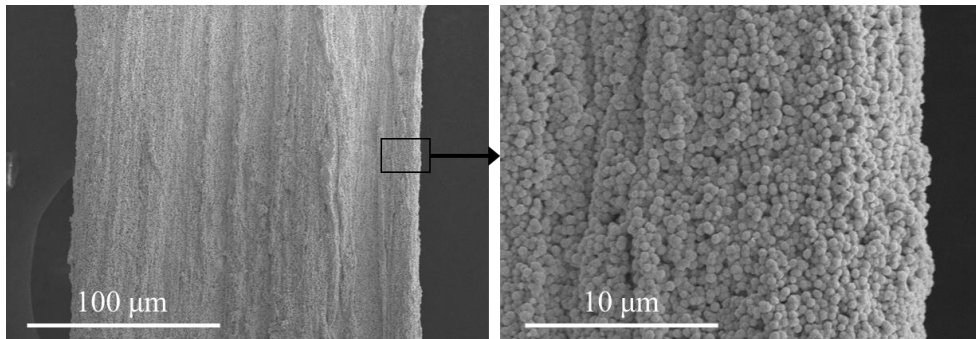


Figure 4.2 SEM images of the gold electroplated CNT bundle with numerous gold particles.

To determine if these enhancements are results of the material property or the surface geometry of the electroplated gold, it was attempted (1) to directly coat the CNT bundle with gold by sputtering and (2) to electroplate a Pt/Ir wire with gold following the electroplating procedure identical to that described in the subsection 2.1.2. For comparison of impedances with various site areas, the area-specific impedance is introduced as the impedance multiplied by the geometrical electrode site area. The presence of sputtered gold on the CNT bundle increases the impedance of the electrode array and results in insignificant changes in the CSCc value. This indicates that the dramatic increase in the CSCc values after the gold-electroplating of the CNT bundle is not likely to have been induced by the electroplated material.

In order to compare with electrode site materials of conventional metal wire-based cochlear electrode arrays, the electrochemical properties of the Pt/Ir alloy wire were measured. Conventional metal wire-based intracochlear electrode arrays commonly use Pt/Ir alloy as conductor line and electrode sites. The SEM image

shown in Figure 4.3 (b) also shows that a large amount of gold particles was formed on the surface of the Pt/Ir wire after the gold electroplating. And, the impedance of the Pt/Ir wire was lowered and the CSCc value increased as in the case of the CNT bundle. However, the enhancement of the electrochemical properties before and after the gold electroplating was greater in the CNT bundle than in the Pt/Ir wire. As a result, the enhanced electrochemical properties of the electrode array can be explained by the formation of gold particles via gold electroplating in the rough surface of the bundles with entangled CNTs.

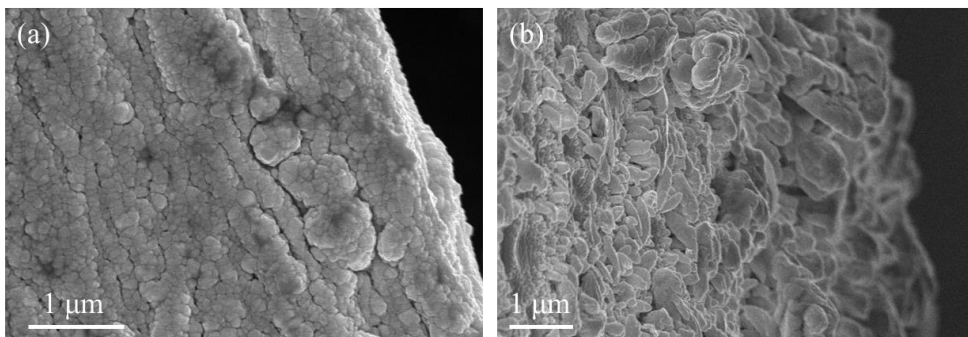


Figure 4.3 SEM images of (a) gold sputtered CNT bundle and (b) gold electroplated Pt/Ir wire.

These electrochemical characteristics of the CNT bundle-based electrode array could lead to the smaller electrode sites and the thinner thickness than conventional intracochlear electrode arrays. Compared to conventional intracochlear electrode arrays with electrode site areas of 0.12–1.5 mm², the CNT bundle-based electrode array has a smaller site with the average area of 0.073 mm², which could also decrease the thickness of the electrode array. [7].

4.1.2 Atraumatic Insertion of CNT Bundle-based Intracochlear Electrode Array

Insertion trauma can be caused by frictional forces generated between an electrode array and the cochlear inner wall. Basically, the frictional force increases as the stiffness of an electrode array increases, thus increasing the risk of trauma [14, 23]. And the exerted insertion force also increases as the insertion depth increases. For the deep insertion into middle or apical turn, the insertion forces should not exceed the mechanical tolerability of the cochlear inner wall during the entire insertion surgical procedure. Structural trauma, such as rupturing the basilar membrane & spiral ligament or penetrating the basilar membrane/osseous spiral lamina, can result in oxidative stress and inflammation that propagate through the cochlea and lead to a loss of the hair cells [18, 114-116]. The extraction force is another significant factor to be considered because the revision and re-implantation of cochlear implant system may be required throughout the patient's lifetime or at the same surgery [117, 118]. For the CNT bundle-based electrode array, the insertion force at 8 mm displacement and maximum extraction force were measured as 0.343 mN and 8.07 mN, respectively. The 8 mm displacement is the first contact between the electrode array and the inner wall of the ST model, which exhibits high risk of insertion trauma. In contrast, the metal wire-based dummy intracochlear electrode array had 2.09 mN of insertion force at displacement of 8 mm and 72.3 mN of maximum extraction force. It indicates that the replacement of the conventional metal wires with the CNT bundles and the decrease of electrode thickness could dramatically reduce the insertion forces exerted on the cochlea inner wall during

insertion as well as extraction. Given that trauma during electrode insertion surgery is contingent upon the insertion force and the electrode size, it is likely that the CNT bundle-based electrode array will significantly reduce trauma in the cochlea during surgery [17, 19-21].

The fabricated CNT bundle-based electrode array has 16 mm of active stimulation region and shows 19 mm of insertion displacement, in other words, 270° of insertion angle, during the insertion test [119]. Therefore, the electrode array was inserted into the basal turn of the ST model and bent in the horizontal direction only. However, for the improved perception of music and the recognition in noise, deeper insertion of the electrode array into the cochlea is required [77, 120]. Because an intracochlear electrode array is inserted into the spiral-shaped cochlea structure, the stiffness in vertical and horizontal directions needs to be considered for the deeper insertion (Figure 4.4). In addition, electrode arrays with greater stiffness in the vertical direction are likely to induce severe insertion trauma, such as penetration of the basilar membrane and/or osseous spiral lamina [17]. According to the simulation results, the CNT bundle-based intracochlear electrode array has greater stiffness in the vertical direction than in the horizontal direction. But, compared to the simulation result of the metal wire-based dummy electrode array, the proposed electrode array shows less stiffness in the horizontal direction and similar stiffness in the vertical direction. Given the values of the calculated stiffnesses, the CNT bundle-based electrode array can be expected to have the vertical flexibility similar to that of a metal wire-based electrode array in the middle and apical turn of cochlea. However, the stiffness values are calculated by the simulation of the electrode array bent simply

in the horizontal and vertical directions, respectively. Further experiments should be implemented to verify the stiffness and flexibility of the fabricated electrode array implanted into the spiraled three-dimensional cochlea structure.

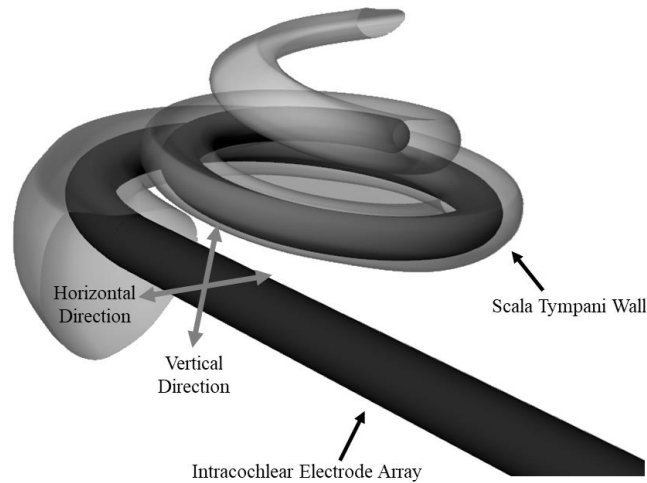


Figure 4.4 Scala tympani model with inserted intracochlear electrode array. Directions of horizontal and vertical deflection are described.

For the deep electrode insertion, a CNT-based thin and flexible intracochlear electrode array with longer active stimulation region and higher channel numbers can be considered. In order to fabricate an intracochlear electrode array with higher channel numbers based on CNT, a precise micro-fabrication process using CNT material is required. The channel number of conventional intracochlear electrode arrays is ranging from 12 to 22. Because the number of encapsulated CNT bundles determines the total stimulation channel numbers, current manual process of aligning and encapsulating the CNT bundles is not suitable for the increase of the channel number. To address the limitation, it could be used to deposit a CNT thin-film via

catalytic growth or chemical vapor deposition on full wafer scale [121, 122]. Also, a micro-fabrication process using CNT thin-film and biocompatible polymers can be advantageous to the development of a thin, flexible, and multi-layered high channel electrode array.

But, the low stiffness of the electrode array can cause less insertion depth and increase the risk of electrode malposition [17, 77]. Although the fabricated CNT bundle-based electrode array maintained the correct electrode position in the human ST model during the insertion test, additional stiffness measurements like flexural bending tests or buckling tests are required [123]. Also, it is necessary to clinically test whether or not such high flexibility of the CNT bundle-based electrode array could lower the risk of trauma and electrode malposition during insertion into the human cochlea.

4.1.3 *In Vivo* Implantation

Recording of eABR waves have been widely used to analyze the auditory neural survival and measure the efficacy of cochlear implant systems [124]. To ascertain if the proposed electrode array can be used for stimulation of the auditory nerves, the electrode array was inserted into the cochlea of the SD rat, and the electrically evoked neural responses were recorded. Although the cross-sectional area of the SD rat's scala tympani is much smaller (0.1 mm^2 at insertion depth greater than 3 mm) than that of human's, the fabricated thin electrode array could be inserted into the SD rat's cochlea without difficulty [110, 125]. Because the total depth of the cochlea of the SD rat is 7 mm, the electrode array was inserted with the depth of up

to 5 mm, which corresponds to the length up to the first three electrode sites of the developed electrode array. Electrical current pulses were addressed through each electrode sites and the eABR waves were recorded. Based on the pattern of recorded waves, the eABR threshold can be determined at 50 μA , 100 μA , and 30 μA for 1st, 2nd, and 3rd electrode sites because the waves III and V were observed above the current stimulation levels [124]. The waves III and V of the eABR recordings are associated with the activity of the mid and upper brainstem within the auditory pathway [126]. And, the negative damping of the eABR wave indicates the cochlear microphonic potential, which is generated by the vector sum of the hair cells [127]. These results clearly verified that the fabricated electrode array could evoke the brainstem responses electrically by delivering stimulation pulses through the auditory pathway and serve as an intracochlear electrode array.

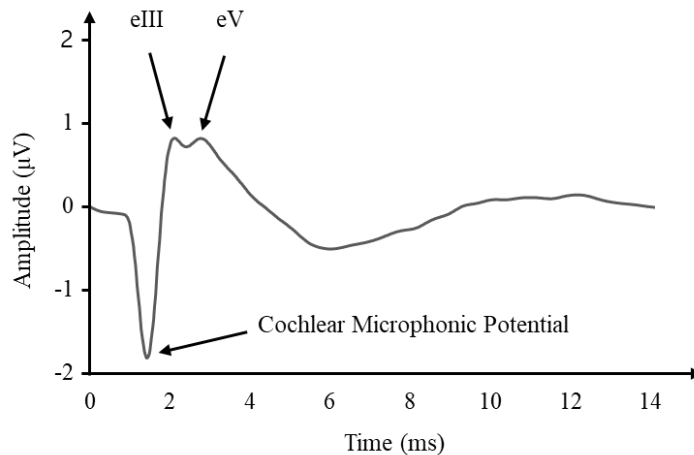


Figure 4.5 Recorded eABR wave at the 1st electrode site at 500 μA of current stimulation level.

There is no doubt that the biocompatibility and toxicity of CNT-based

materials should be evaluated prior to their long-term implantation into the human body. Previously, the biocompatibility of CNT was investigated through long-term neural recordings and vein injection method [128-130]. Studies on neurons, osteoblast cells, and vein injection support the biocompatibility of CNT-based materials. Long-term *in vivo* stability was demonstrated by neural recording and stimulation using CNT-based microelectrodes in the brain [64]. In contrast, notwithstanding the evidence of the biocompatibility, there exist several previous studies which reported the toxicity of CNT-based materials, causing the inflammations of lung, abdominal, subcutaneous, and skin [128-130]. These studies indicate that CNT-based materials can exhibit varying degrees of biocompatibility depending on the implanted part of the body. It is also likely that the released nanostructures of CNTs induce the cellular toxicity. In this study, in the electrode fabrication process, the entire surface of the electrode array was electroplated using gold. Because gold is a biocompatible material and the CNT bundles are not directly exposed to the lymph fluid in the scala tympani, it is likely that the proposed electrode array may not be toxic to tissues in the cochlea.

4.2 Implantable Multi-channel Connector

4.2.1 Miniaturized Re-connectable Connector

To fabricate the implantable connector with high channel density, micro-fabrication and thermal lamination processes were used with LCP films. Table 4.1 shows the characteristics of biocompatible polymer materials which is compatible with micro-fabrication process. The proposed connector is designed to apply the

contact pressures between the contact pads by tensions of the connector wall, which is stretched through the bump structure of the connector and the inserted cable. As the connector is made of polymer materials with higher young's modulus, greater contact pressures can be applied. Also, the three-dimensional bidirectional connector with the bump structures inside should be fabricated using micro-patterned polymer materials. A spin coating process is used for fabrication of multi-layer structure, and a vacuum deposition technique is used to stack up multiple layers with parylene-C. However, these processes require photolithography or etching process to be followed for development of three-dimensional structure such as cavity or bump. LCP has the advantage that three-dimensional structures can be easily fabricated with the thermal lamination process using the pressing jig. In addition, LCP has a much lower moisture absorption rate than those of polyimide and parylene-C, which is highly related to the long-term reliability of the cable [100, 104].

Table 4.1 Characteristics of biocompatible polymer materials [90, 131-135].

<i>Material</i>	<i>Resistivity</i> ($\Omega \cdot \text{cm}$)	<i>Melting temperature</i> ($^{\circ}\text{C}$)	<i>Young's modulus</i> (MPa)	<i>Water absorption rate</i> (%)
Polyimide	$1.0 - 1.5 \times 10^{17}$	>400	2,280 - 2,620	0.24 - 4
Parylene-C	8.8×10^{16}	290	2,760	0.06 - 4
Silicone elastomer	$1 - 10 \times 10^{14}$	200 - 250	100 - 500	0.1 - 1.3
LCP	3×10^{16}	280 - 335 (Thermal deformable)	2,000-40,000	<0.04

It is essential to make an implantable connector re-connectable and re-usable for simplification of implantation surgery and safe replacement of implanted devices. The fabricated LCP-based connector and the cable maintained the contact resistance consistent during 50 trials of the repeated connection test. Also, after the entire repeated connection test, there was no apparent damage to the LCP-based connector, the cable, and the contact pads (Figure 4.6). The LCP-based connector was electrically connected to the cables and sealed by the metal case & the silicone elastomer packings to block water penetration. And, the metal cases were made of sus 304 stainless steel, a biocompatible metal used for biomedical applications [136, 137]. As sus 304 has the good wear resistance characteristic, the screw thread parts of the metal cases are expected to withstand the repeated opening and reassembly during re-implantation procedures [138]. It is likely that the fabricated implantable connector has good mechanical stability and re-connectability for replacements of neural implant devices in a lifetime. However, the re-connectability and re-usability need to be further investigated to verify that the sealing performance is maintained after the opening and reassembly procedure of the connector during long-term implantation.

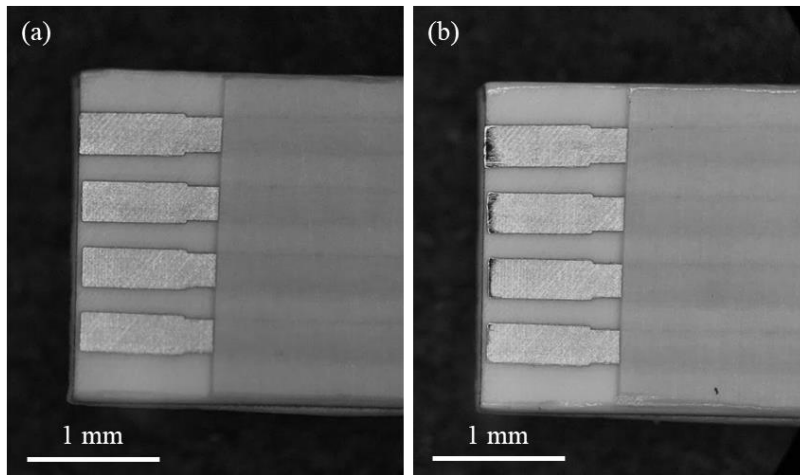


Figure 4.6 Contact pads of the LCP-based cable (a) before and (b) after the repeated connection test.

For minimal invasive implantation surgery, a miniaturized implantable multi-channel connector with high channel density is needed. In this study, the micro-patterned LCP films were used for the fabrication of the multi-channel connector with high channel density. The developed four and eight-channel implantable connectors have channel densities of $14.2 \text{ channel/cm}^2$ and $28.3 \text{ channel/cm}^2$, respectively, and a length of 17 mm after assembled with the metal cases. The channel density of a connector is defined as the ratio of the total number of connector channels to the cross-sectional area of the assembled connector, and the length of connector is the total length of the parts combined for connection and sealing. The fabricated implantable connector has a similar channel density to the circular contact pad connector. And the connector shows the shortest connector length compared with other implantable connectors used for connection and extension of cables (Table 4.2). These high channel density and miniaturized size can be achieved not only by the bump structures enabling the electrical contacts

between contact pads established without extra housing parts, but also the application of the micro-fabrication process for the contact pad generation. It is expected that an implantable connector with increased channel density than the developed connector can be fabricated by forming finer metal patterns. And, with increases of channel number and channel density, the suggested implantable connector could be applied to more various neural implant systems.

However, further consideration should be given for the proposed connector to be used with cochlear implant. Cochlear implant is implanted in a space secured by grinding the temporal bone, and a 1 mm thick hole is drilled in the temporal bone for insertion of an electrode array. For the fabricated connector to be implanted with cochlear implant in its current size, the drilled hole or the space on the temporal bone has to be secured, which requires the verification of post-surgical stability. In order to avoid additional grinding and drilling of the temporal bone, the connector size itself needs to be reduced and minimized. In addition, magnetic resonance imaging (MRI) compatibility of the metal cases used for the fabricated connector needs to be contemplated. SUS 304 stainless steel, a material of the metal cases, is basically a paramagnetic material. However, any process which can change the crystal structure can cause ferromagnetism of SUS 304 [139]. Because MRI machines use superconducting magnets for large static magnetic field generation, ferromagnetic materials implanted into the body are the most harmful factor causing the missile effect in the magnetic resonance environment [99]. Medical grade titanium, a paramagnetic material widely used in cochlear implant packages, can be used as a material for the metal cases to increase the MRI compatibility.

Table 4.2 Dimensions of implantable multi-channel connectors [67-70, 140].

<i>Type</i>	<i>Number of Channels</i>	<i>Diameter (mm)</i>	<i>Channel Density (# of channel/cm²)</i>	<i>Length (mm)</i>	<i>Sealing Method</i>	<i>Long-term Reliability</i>	<i>Usage</i>
Craggs connector	1, 3	7.5	2.26, 6.79	60	Adhesive sealant	2 years (implant)	Lumbar anterior root stimulator
In-Line Lead connector	1	3.5	10.4	30	Silicone elastomer suturing	49 months (implant)	Custom neural stimulator
Circular contact pad connector	1 – 4	4.06	7.72 – 30.9	30	Silicone elastomer packing	Application in the patient (pacemaker, DBS)	DBS, Bladder stimulator
Proposed connector	4, 8	6	14.2, 28.3	17	Silicone elastomer packing	< 4 years (<i>in vitro</i> , estimated)	-

4.2.2 Long-term Reliability

The leakage and crosstalk current measurements during the *in vitro* accelerated soak test showed that the group with the block-shape packing having 137% of volume ratio was more reliable than the other sample groups. The difference in the soak time until device failure between the dental resin and the silicone elastomer sealing groups can be caused by the mechanical characteristics of the sealing materials. Because the dental resin has rigid mechanical property compared with the silicone elastomers, water can be easily penetrated through the separated interface between the sealing material and the covered cable. The soak times of sample groups with the silicone elastomer packings and the metal cases can be explained by the difference in packing volumes. The block-shape packing with 125% of volume ratio, which is relatively small, has insufficient clamping force applied by the tightened metal cases, and it is likely that block-shape packing having 150% of volume ratio is malpositioned with an excessively large size during the assembly of the metal cases. As a result, the block-shape packing having 137% of volume ratio might be properly placed inside the metal cases while applying sufficient clamping force, which results in the effective sealing and the longest soak time. The results of the soak test indicate the possibility that the fabricated connector can be used to provide the modularity of implant systems and flexible implantation surgery in short-term *in vivo* experiments.

However, the estimated lifetime of 1098 days (approximately 3 years) is still short to be used in clinical practice with conventional neural implants systems. And, the estimated lifetime of the connector is too short to be applied to cochlear implant,

which is implanted into the body for more than 10 years until the device revision [27, 28]. If the enhancement of the sealing performance is not ensured, the use of the proposed connector can increase the risk of water leakage and device failure. A potential source of device failure is water penetration through the silicone elastomer packings, which has high water-vapor permeability. Previously, controlling the permeability of silicone elastomer was investigated by synthesizing composites with different materials, such as collagen, carbon black, and carbon nanotube [141-143]. These studies indicate that silicone elastomer packings with lower water-vapor permeability can be fabricated, which may increase the long-term reliability and lifetime of the assembled connector.

Chapter V

Conclusion

In the present study, the CNT Bundle-based thin intracochlear electrode array and the implantable multi-channel connector are proposed for the possible development of improved cochlear implant system. The CNT Bundle-based electrode array is fabricated by replacing the metal wires used for conventional intracochlear electrode array with the CNT bundles. And, the re-connectable and miniaturized implantable multi-channel connector are fabricated using the LCP-based micro-fabrication and the thermal lamination processes.

The 8-channel CNT Bundle-based intracochlear electrode array is fabricated with eight CNT bundles. The electrode array has a thickness of 135 μm at the apex and 395 μm at the base which has a smaller thickness than conventional intracochlear electrode arrays. The electroplated gold layer on the surface of the CNT bundle results in the enhancement of electrochemical characteristics, which leads to the smaller electrode sites and the thinner electrode thickness than conventional intracochlear electrode arrays. Also, the replacement of conventional metal wires with the CNT bundles significantly reduces the insertion and extraction force exerted on the cochlea model. These indicate that insertion trauma which is related to the insertion force and electrode thickness can be lowered with the CNT bundle-based electrode array. And, the simulation results show the possibility of deeper insertion into spiral-shaped cochlea with longer stimulation region. The feasibility of the electrode array is demonstrated via acute electrical stimulation in the SD rat model. The CNT Bundle-based intracochlear electrode array is inserted into the cochlea of the SD rat, which has a much smaller cross-sectional area of the scala tympani, and the eABR waves are evoked by the electrode array. It is expected that the developed

intracochlear electrode array can be used to reduce electrode insertion trauma by minimizing insertion force.

In addition, the experimental prototype of the re-connectable and miniaturized implantable multi-channel connector is proposed for contribution to simple and safe replacement of implanted electrode array. The bidirectional LCP-based connector is fabricated using the micro-patterning and the thermal lamination processes. The electrical connection is established at all conductor lines after the developed 4 and 8-channel connectors are connected to the LCP-based cables. The re-connectability of the connector is demonstrated by showing that the contact resistance between contact pads of the connector and the cable is maintained stable for 50 trials of repeated connection. The connector sealed by silicone elastomer packings and metal cases has higher channel density than previously reported implantable connectors. Finally, the sealing performance and the long-term reliability are verified in *in vitro* accelerated soak test. Also, with further increases in channel density, miniaturization, and sealing performance, it is likely that the proposed implantable connector can contribute to safe re-implantation surgery of cochlear implant.

References

- [1] A. Prochazka, V. K. Mushahwar, and D. B. McCreery, "Neural prostheses," *The Journal of physiology*, vol. 533, no. 1, pp. 99-109, 2001.
- [2] T. Stieglitz, M. Schuetter, and K. P. Koch, "Implantable biomedical microsystems for neural prostheses," *IEEE engineering in medicine and biology magazine*, vol. 24, no. 5, pp. 58-65, 2005.
- [3] S. F. Cogan, "Neural stimulation and recording electrodes," *Annu. Rev. Biomed. Eng.*, vol. 10, pp. 275-309, 2008.
- [4] B. J. Gantz, B. F. McCabe, and R. S. Tyler, "Use of multichannel cochlear implants in obstructed and obliterated cochleas," *Otolaryngology—Head and Neck Surgery*, vol. 98, no. 1, pp. 72-81, 1988.
- [5] B. S. Wilson, C. C. Finley, D. T. Lawson, R. D. Wolford, D. K. Eddington, and W. M. Rabinowitz, "Better speech recognition with cochlear implants," *Nature*, vol. 352, no. 6332, p. 236, 1991.
- [6] K. D. Brown and T. J. Balkany, "Benefits of bilateral cochlear implantation: a review," *Current opinion in otolaryngology & head and neck surgery*, vol. 15, no. 5, pp. 315-318, 2007.
- [7] F.-G. Zeng, S. Rebscher, W. Harrison, X. Sun, and H. Feng, "Cochlear implants: system design, integration, and evaluation," *IEEE reviews in biomedical engineering*, vol. 1, pp. 115-142, 2008.
- [8] M. S. Humayun, J. D. Dorn, L. D. Cruz, G. Dagnelie, J.-A. Sahel, P. E. Stanga, *et al.*, "Interim results from the international trial of Second Sight's visual prosthesis," *Ophthalmology*, vol. 119, no. 4, pp. 779-788, 2012.
- [9] E. Margalit, M. Maia, J. D. Weiland, R. J. Greenberg, G. Y. Fujii, G. Torress, *et al.*, "Retinal prosthesis for the blind," *Survey of ophthalmology*, vol. 47, no. 4, pp. 335-356, 2002.
- [10] A. L. Benabid, "Deep brain stimulation for Parkinson's disease," *Current opinion in neurobiology*, vol. 13, no. 6, pp. 696-706, 2003.
- [11] H. S. Mayberg, A. M. Lozano, V. Voon, H. E. McNeely, D. Seminowicz, C. Hamani, *et al.*, "Deep brain stimulation for treatment-resistant depression," *Neuron*, vol. 45, no. 5, pp. 651-660, 2005.
- [12] J. S. Perlmutter and J. W. Mink, "Deep brain stimulation," *Annu. Rev. Neurosci.*, vol. 29, pp. 229-257, 2006.

- [13] D. S. Kern and R. Kumar, "Deep brain stimulation," *The Neurologist*, vol. 13, no. 5, pp. 237-252, 2007.
- [14] C. James, K. Albegger, R. Battmer, S. Burdo, N. Deggouj, O. Deguine, *et al.*, "Preservation of residual hearing with cochlear implantation: how and why," *Acta otolaryngologica*, vol. 125, no. 5, pp. 481-491, 2005.
- [15] T. R. McRackan, M. Bauschard, J. L. Hatch, E. Franko-Tobin, H. R. Droghini, S. A. Nguyen, *et al.*, "Meta-analysis of quality-of-life improvement after cochlear implantation and associations with speech recognition abilities," *The Laryngoscope*, vol. 128, no. 4, pp. 982-990, 2018.
- [16] F.-G. Zeng, "Cochlear implants: Why don't more people use them?," *The Hearing Journal*, vol. 60, no. 3, pp. 48-49, 2007.
- [17] S. J. Rebscher, A. Hetherington, B. Bonham, P. Wardrop, D. Whinney, and P. A. Leake, "Considerations for the design of future cochlear implant electrode arrays: Electrode array stiffness, size and depth of insertion," *Journal of rehabilitation research and development*, vol. 45, no. 5, p. 731, 2008.
- [18] E. Bas, J. Bohorquez, S. Goncalves, E. Perez, C. T. Dinh, C. Garnham, *et al.*, "Electrode array-eluted dexamethasone protects against electrode insertion trauma induced hearing and hair cell losses, damage to neural elements, increases in impedance and fibrosis: A dose response study," *Hearing research*, vol. 337, pp. 12-24, 2016.
- [19] A. Aschendorff, T. Klenzner, B. Richter, R. Kubalek, H. Nagursky, and R. Laszig, "Evaluation of the HiFocus® electrode array with positioner in human temporal bones," *The Journal of Laryngology & Otology*, vol. 117, no. 7, pp. 527-531, 2003.
- [20] A. A. Eshraghi, N. W. Yang, and T. J. Balkany, "Comparative study of cochlear damage with three perimodiolar electrode designs," *The Laryngoscope*, vol. 113, no. 3, pp. 415-419, 2003.
- [21] P. Wardrop, D. Whinney, S. J. Rebscher, W. Luxford, and P. Leake, "A temporal bone study of insertion trauma and intracochlear position of cochlear implant electrodes. II: Comparison of Spiral Clarion™ and HiFocus II™ electrodes," *Hearing research*, vol. 203, no. 1, pp. 68-79, 2005.
- [22] F. A. Spelman, "Cochlear electrode arrays: past, present and future," *Audiology and Neurotology*, vol. 11, no. 2, pp. 77-85, 2006.
- [23] S. J. Rebscher, M. Heilmann, W. Bruszewski, N. H. Talbot, R. L. Snyder, and M. M. Merzenich, "Strategies to improve electrode positioning and safety in cochlear implants," *IEEE Transactions on Biomedical Engineering*, vol. 46, no. 3, pp. 340-352, 1999.

- [24] P. Busby, K. Plant, and L. Whitford, "Electrode impedance in adults and children using the Nucleus 24 cochlear implant system," *Cochlear implants international*, vol. 3, no. 2, pp. 87-103, 2002.
- [25] A. Henson, W. Luxford, and D. M. Mills, "Cochlear implant performance after reimplantation: a multicenter study," *The American journal of otology*, vol. 20, no. 1, pp. 56-64, 1999.
- [26] T. Sorrentino, M. Côté, E. Eter, M.-L Laborde, N. Cochard, O. Deguine, *et al.*, "Cochlear reimplantations: technical and surgical failures," *Acta oto-laryngologica*, vol. 129, no. 4, pp. 380-384, 2009.
- [27] A.-A. D. Lassig, T. A. Zwolan, S. A. Telian, "Cochlear implant failures and revision," *Otology & Neurotology*, vol. 26, no. 4, pp. 624-634, 2005.
- [28] M. Côté, P. Ferron, F. Bergeron, and R. Bussi eres, "Cochlear reimplantation: causes of failure, outcomes, and audiologic performance," *The Laryngoscope*, vol. 117, no. 7, pp. 1225-1235, 2007.
- [29] J. T. Wang, A. Y. Wang, C. Psarros, and M. Da Cruz, "Rates of revision and device failure in cochlear implant surgery: A 30-year experience," *The Laryngoscope*, vol. 124, no. 10, pp. 2393-2399, 2014.
- [30] J. B. Weise, J. Muller-Deile, G. Brademann, J. E. Meyer, P. Ambrosch, and S. Maune, "Impact to the head increases cochlear implant reimplantation rate in children," *Auris Nasus Larynx*, vol. 32, no. 4, pp. 339-343, 2005.
- [31] J. N. Fayad, T. Bairo, and S. C. Parisier, "Revision cochlear implant surgery: causes and outcome," *Otolaryngology—Head and Neck Surgery*, vol. 131, no. 4, pp. 429-432, 2004.
- [32] J. Ray, D. Proops, I. Donaldson, C. Fielden, and H. Cooper, "Explantation and reimplantation of cochlear implants," *Cochlear implants international*, vol. 5, no. 4, pp. 160-167, 2004.
- [33] M.-N. Calmels, I. Saliba, G. Wanna, N. Cochard, J. Fillaux, O. Dequine, *et al.*, "Speech perception and speech intelligibility in children after cochlear implantation," *International journal of pediatric otorhinolaryngology*, vol. 68, no. 3, pp. 347-351, 2004.
- [34] S.-C. Peng, J. B. Tomblin, and C. W. Turner, "Production and perception of speech intonation in pediatric cochlear implant recipients and individuals with normal hearing," *Ear and hearing*, vol. 29, no. 3, pp. 336-351, 2008.
- [35] B. S. Wilson, C. C. Finley, D. T. Lawson, R. D. Wolford, D. K. Eddington, and W. M. Rabinowitz, "Better speech recognition with cochlear implants," *Nature*, vol. 352, no. 6332, pp. 236-238, 1991.

- [36] B. Wilson, C. C. Finley, B. A. Weber, M. W. White, J. C. Farmer Jr, R. D. Wolford, *et al.*, "Comparative studies of speech processing strategies for cochlear implants," *The Laryngoscope*, vol. 98, no. 10, pp. 1069-1077, 1988.
- [37] B. Somek, S. Fajt, A. Dembitz, M. Ivković, and J. Ostojić, "Coding strategies for cochlear implants," *AUTOMATIKA: časopis za automatiku, mjerenje, elektroniku, računarstvo i komunikacije*, vol. 47, no. 1-2, pp. 69-74, 2006.
- [38] C. T. Choi and Y.-H. Lee, "A review of stimulating strategies for cochlear implants," *Cochlear Implant Research Updates*, Intechopen, 2012.
- [39] C. W. Turner, L. A. Reiss, and B. J. Gantz, "Combined acoustic and electric hearing: preserving residual acoustic hearing," *Hearing research*, vol. 242, no. 1-2, pp. 164-171, 2008.
- [40] W. Gstoettner, J. Kiefer, W.-D. Baumgartner, S. Pok, S. Peters, and O. Adunka, "Hearing preservation in cochlear implantation for electric acoustic stimulation," *Acta otolaryngologica*, vol. 124, no. 4, pp. 348-352, 2004.
- [41] C. von Ilberg, J. Kiefer, J. Tillein, T. Pfenningdorff, R. Hartmann, E. Stürzebecher, *et al.*, "Electric-acoustic stimulation of the auditory system," *ORL: Journal for Oto-Rhino-Laryngology and Its Related Specialties*, vol. 61, no. 6, p. 334, 1999.
- [42] K. D. Brown and T. J. Balkany, "Benefits of bilateral cochlear implantation: a review," *Current opinion in otolaryngology & head and neck surgery*, vol. 15, no. 5, pp. 315-318, 2007.
- [43] J. B. Nadol, "Histological considerations in implant patients," *Archives of Otolaryngology*, vol. 110, no. 3, pp. 160-163, 1984.
- [44] S. A. Khalifa, P. Björk, C. Vieider, M. Ulfendahl, and E. Scarfone, "Neuronal polarity mediated by micro-scale protein patterns and Schwann cells in vitro," *Tissue Engineering and Regenerative Medicine*, vol. 10, no. 5, pp. 266-272, 2013.
- [45] S. K. An, S. I. Park, S. B. Jun, C. J. Lee, K. M. Byun, J. H. Sung, *et al.*, "Design for a simplified cochlear implant system," *IEEE Transactions on Biomedical Engineering*, vol. 54, no. 6, pp. 973-982, 2007.
- [46] H. Skarzynski, A. Lorens, M. Matusiak, M. Porowski, P. H. Skarzynski, and C. J. James, "Cochlear implantation with the nucleus slim straight electrode in subjects with residual low-frequency hearing," *Ear and hearing*, vol. 35, no. 2, pp. e33-e43, 2014.
- [47] S. Helbig, Y. Adel, T. Rader, T. Stöver, and U. Baumann, "Long-term Hearing Preservation Outcomes After Cochlear Implantation for Electric-Acoustic Stimulation," *Otology & Neurotology*, vol. 37, no. 9, pp. e353-e359, 2016.
- [48] K. D. Wise, P. T. Bhatti, J. Wang, and C. R. Friedrich, "High-density cochlear implants

- with position sensing and control," *Hearing research*, vol. 242, no. 1-2, pp. 22-30, 2008.
- [49] S. Herwik, S. Kisban, A. A. A. Aarts, K. Seidl, G. Girardeau, K. Benchenane, *et al.*, "Fabrication technology for silicon-based microprobe arrays used in acute and sub-chronic neural recording," *Journal of Micromechanics and Microengineering*, vol. 19, no. 7, p. 074008, 2009.
- [50] K. S. Min, S. H. Oh, M.-H. Park, J. Jeong, and S. J. Kim, "A polymer-based multichannel cochlear electrode array," *Otology & Neurotology*, vol. 35, no. 7, pp. 1179-1186, 2014.
- [51] T. M. Gwon, K. S. Min, J. H. Kim, S. H. Oh, H. S. Lee, M. H. Park, *et al.*, "Fabrication and evaluation of an improved polymer-based cochlear electrode array for atraumatic insertion," *Biomedical microdevices*, vol. 17, no. 2, pp. 1-12, 2015.
- [52] B. H. Bonham and L. M. Litvak, "Current focusing and steering: modeling, physiology, and psychophysics," *Hearing research*, vol. 242, no. 1-2, pp. 141-153, 2008.
- [53] C. K. Berenstein, L. H. Mens, J. J. Mulder, and F. J. Vanpoucke, "Current steering and current focusing in cochlear implants: comparison of monopolar, tripolar, and virtual channel electrode configurations," *Ear and hearing*, vol. 29, no. 2, pp. 250-260, 2008.
- [54] D. M. Landsberger and A. G. Srinivasan, "Virtual channel discrimination is improved by current focusing in cochlear implant recipients," *Hearing research*, vol. 254, no. 1-2, pp. 34-41, 2009.
- [55] Z. Zhu, Q. Tang, F.-G. Zeng, T. Guan, and D. Ye, "Cochlear-implant spatial selectivity with monopolar, bipolar and tripolar stimulation," *Hearing research*, vol. 283, no. 1-2, pp. 45-58, 2012.
- [56] C. Nadège, G. Valérie, F. Laura, D. B. Hélène, B. Vanina, D. Olivier, *et al.*, "The cost of cochlear implantation: a review of methodological considerations," *International journal of otolaryngology*, vol. 2011, 2011.
- [57] S. Iijima, "Helical microtubules of graphitic carbon," *Nature*, vol. 354, no. 6348, pp. 56-58, 1991.
- [58] M. F. De Volder, S. H. Tawfick, R. H. Baughman, and A. J. Hart, "Carbon nanotubes: present and future commercial applications," *Science*, vol. 339, no. 6119, pp. 535-539, 2013.
- [59] X. Li, Y. Fan, and F. Watari, "Current investigations into carbon nanotubes for biomedical application," *Biomedical Materials*, vol. 5, no. 2, p. 022001, 2010.
- [60] A. Bianco, K. Kostarelos, C. D. Partidos, and M. Prato, "Biomedical applications of functionalised carbon nanotubes," *Chemical Communications*, no. 5, pp. 571-577, 2005.
- [61] W. Yang, P. Thordarson, J. J. Gooding, S. P. Ringer, and F. Braet, "Carbon nanotubes for biological and biomedical applications," *Nanotechnology*, vol. 18, no. 41, p. 412001, 2007.

- [62] K. Wang, H. A. Fishman, H. Dai, and J. S. Harris, "Neural stimulation with a carbon nanotube microelectrode array," *Nano letters*, vol. 6, no. 9, pp. 2043-2048, 2006.
- [63] R. A. Parker, S. Negi, T. Davis, E. W. Keefer, H. Wiggins, P. A. House, *et al.*, "The use of a novel carbon nanotube coated microelectrode array for chronic intracortical recording and microstimulation," *2012 Annual International Conference of the IEEE Engineering in Medicine and Biology Society*, 2012, pp. 791-794: IEEE.
- [64] F. Vitale, S. R. Summerson, B. Aazhang, C. Kemere, and M. Pasquali, "Neural stimulation and recording with bidirectional, soft carbon nanotube fiber microelectrodes," *ACS nano*, vol. 9, no. 4, pp. 4465-4474, 2015.
- [65] H. Choo, Y. Jung, Y. Jeong, H. C. Kim, and B. C. Ku, "Fabrication and applications of carbon nanotube fibers," *Carbon letters*, vol. 13, no. 4, pp. 191-204, 2012.
- [66] P. E. Donaldson, "The craggs connector; a termination for cooper cable," *Medical and Biological Engineering and Computing*, vol. 23, no. 2, pp. 195-196, 1985.
- [67] D. Rushton, A. Tromans, N. de N Donaldson, "A reconnectable multiway implantable connector," *Medical engineering & physics*, vol. 24, no. 10, pp. 691-694, 2002.
- [68] J. E. Letechipia, P. H. Peckham, M. Gazdik, and B. Smith, "In-line lead connector for use with implanted neuroprosthesis," *IEEE transactions on biomedical engineering*, vol. 38, no. 7, pp. 707-709, 1991.
- [69] H. G. Mond, J. R. Helland, A. V. I. Fischer, "The evolution of the cardiac implantable electronic device connector," *Pacing and Clinical Electrophysiology*, vol. 36, no. 11, pp. 1434-1446, 2013.
- [70] S.-W. Lee, M.-K. Lee, I. Seo, H.-S. Kim, J.-H. Kim, and Y.-S. Kim, "A Groove Technique for Securing an Electrode Connector on the Cranial Bone: Case Analysis of Efficacy," *Journal of Korean Neurosurgical Society*, vol. 56, no. 2, p. 130, 2014.
- [71] Y.-L. Li, I. A. Kinloch, and A. H. Windle, "Direct spinning of carbon nanotube fibers from chemical vapor deposition synthesis," *Science*, vol. 304, no. 5668, pp. 276-278, 2004.
- [72] K. Koziol, J. Vilatela, A. Moissala, M. Motta, P. Cunniff, M. Sennett, *et al.*, "High-performance carbon nanotube fiber," *Science*, vol. 318, no. 5858, pp. 1892-1895, 2007.
- [73] S. W. Lee, J. M. Seo, S. Ha, E. T. Kim, H. Chung, and S. J. Kim, *et al.*, "Development of microelectrode arrays for artificial retinal implants using liquid crystal polymers," *Investigative ophthalmology & visual science*, vol. 50, no. 12, pp. 5859-5866, 2009.
- [74] S. E. Lee, S. B. Jun, H. J. Lee, J. Kim, S. W. Lee, C. Im, *et al.*, "A flexible depth probe using liquid crystal polymer," *IEEE Transactions on Biomedical Engineering*, vol. 59, no. 7, pp. 2085-2094, 2012.

- [75] S. Shin, J.-H. Kim, J. Jeong, T. M. Gwon, S.-H. Lee, and S. J. Kim, "Novel four-sided neural probe fabricated by a thermal lamination process of polymer films," *Journal of neuroscience methods*, vol. 278, pp. 25-35, 2017.
- [76] J. J. Roland, T. M. Magardino, J. T. Go, D. E. Hillman, "Effects of glycerin, hyaluronic acid, and hydroxypropyl methylcellulose on the spiral ganglion of the guinea pig cochlea," *The Annals of Otology, Rhinology & Laryngology*, vol. 166, pp. 64-68, 1995.
- [77] P. Wardrop, D. Whinney, S. J. Rebscher, J. T. Roland Jr, W. Luxford, and P. A. Leake, "A temporal bone study of insertion trauma and intracochlear position of cochlear implant electrodes. I: Comparison of Nucleus banded and Nucleus Contour™ electrodes," *Hearing research*, vol. 203, no. 1-2, pp. 54-67, 2005.
- [78] J. Zhang, S. Bhattacharyya, and N. Simaan, "Model and parameter identification of friction during robotic insertion of cochlear-implant electrode arrays," *IEEE International Conference on Robotics and Automation*, pp. 3859-3864, 2009.
- [79] M. Miao, J. McDonnell, L. Vuckovic, and S. C. Hawkins, "Poisson's ratio and porosity of carbon nanotube dry-spun yarns," *Carbon*, vol. 48, no. 10, pp. 2802-2811, 2010.
- [80] P. J. Rae and D. M. Dattelbaum, "The properties of poly (tetrafluoroethylene)(PTFE) in compression," *Polymer*, vol. 45, no. 22, pp. 7615-7625, 2004.
- [81] (26 november 2019). MakeItFrom. Available: <https://www.makeitfrom.com/material-properties/90-Platinum-10-Iridium-Electrical-Contact-Alloy>
- [82] (26 november 2019). The PGM Database. Available: <http://www.pgmdatabase.com/jmpgm/index.jsp?record=1064>
- [83] (26 november 2019). Trebor International. Available: <https://www.treborintl.com/content/properties-molded-ptfe>
- [84] R. Samuel, C. M. Thacker, A. V. Maricq, B. K. Gale, "Simple and cost-effective fabrication of microvalve arrays in PDMS using laser cut molds with application to *C. elegans* manipulation in microfluidics," *Journal of Micromechanics and Microengineering*, vol. 24, no. 10, p. 105007, 2014.
- [85] T. A. Harder, T.-J. Yao, Q. He, C.-Y. Shih, and Y.-C. Tai, "Residual stress in thin-film parylene-C," *Technical Digest. MEMS 2002 IEEE International Conference. Fifteenth IEEE International Conference on Micro Electro Mechanical Systems (Cat. No. 02CH37266)*, pp. 435-438, 2002.
- [86] G. Yang, X. Liao, and Z. Zhang, "Young's modulus and residual stress of MEMS gold beams based on the GaAs MMIC process," *Journal of Micromechanics and Microengineering*, vol. 23, no. 4, p. 045002, 2013.

- [87] H. Gensler and E. Meng, "Rapid fabrication and characterization of MEMS Parylene C bellows for large deflection applications," *Journal of Micromechanics and Microengineering*, vol. 22, no. 11, p. 115031, 2012.
- [88] M. Motta, Y.-L. Li, I. Kinloch, and A. Windle, "Mechanical properties of continuously spun fibers of carbon nanotubes," *Nano letters*, vol. 5, no. 8, pp. 1529-1533, 2005.
- [89] D. R. Mash and L. D. Hall, "Anelastic Behavior of Pure Gold Wire," *JOM*, vol. 5, no. 7, pp. 937-942, 1953.
- [90] T. M. Gwon, C. Kim, S. Shin, J. H. Park, J. H. Kim, and S. J. Kim, "Liquid crystal polymer (LCP)-based neural prosthetic devices," *Biomedical Engineering Letters*, vol. 6, no. 3, pp. 148-163, 2016.
- [91] M. Polak, A. A. Eshraghi, O. Nehme, S. Ahsan, J. Guzman, R. E. Delgado, *et al.*, "Evaluation of hearing and auditory nerve function by combining ABR, DPOAE and eABR tests into a single recording session," *Journal of neuroscience methods*, vol. 134, no. 2, pp. 141-149, 2004.
- [92] S. Shim, S. Yun, S. Kim, G. J. Choi, C. Baek, J. Jang, *et al.*, "A handheld neural stimulation controller for avian navigation guided by remote control," *Bio-medical materials and engineering*, no. Preprint, pp. 1-11, 2019.
- [93] E. C. Culbertson, "A new laminate material for high performance PCBs: Liquid crystal polymer copper clad films," *1995 Proceedings. 45th Electronic Components and Technology Conference*, pp. 520-523, 1995.
- [94] E. Y. Chow, A. L. Chlebowski, and P. P. Irazoqui, "A miniature-implantable RF-wireless active glaucoma intraocular pressure monitor," *IEEE Transactions on Biomedical Circuits and Systems*, vol. 4, no. 6, pp. 340-349, 2010.
- [95] K. Kang, I. S. Choi, and Y. Nam, "A biofunctionalization scheme for neural interfaces using polydopamine polymer," *Biomaterials*, vol. 32, no. 27, pp. 6374-6380, 2011.
- [96] I. M. Suthers, J. W. Young, M. E. Baird, M. Roughan, J. D. Everett, G. B. Brassington, *et al.*, "The strengthening East Australian Current, its eddies and biological effects—an introduction and overview," ed: Elsevier, 2011.
- [97] G. T. Hwang, D. Im, S. E. Lee, J. Lee, M. Koo, S. Y. Park, *et al.*, "In vivo silicon-based flexible radio frequency integrated circuits monolithically encapsulated with biocompatible liquid crystal polymers," *ACS Nano*, vol. 7, no. 5, pp. 4545-4553, 2013.
- [98] P. Sattayasoonthorn, J. Suthakorn, S. Chamnanvej, J. Miao, and A. Kottapalli, "LCP MEMS implantable pressure sensor for intracranial pressure measurement," *The 7th IEEE International Conference on Nano/Molecular Medicine and Engineering*, pp. 63-67, 2013.

- [99] J. H. Kim, K. S. Min, S. K. An, J. S. Jeong, S. B. Jun, M. H. Cho, *et al.*, "Magnetic resonance imaging compatibility of the polymer-based cochlear implant," *Clinical and experimental otorhinolaryngology*, vol. 5, no. Suppl 1, p. S19, 2012.
- [100] J. Jeong, S. H. Bae, K. S. Min, J.-M. Seo, H. Chung, and S. J. Kim, "A miniaturized, eye-conformable, and long-term reliable retinal prosthesis using monolithic fabrication of liquid crystal polymer (LCP)," *IEEE Transactions on Biomedical Engineering*, vol. 62, no. 3, pp. 982-989, 2015.
- [101] S. Shin, J. Kim, J. Jeong, T. M. Gwon, G. J. Choi, S. E. Lee, *et al.*, "High charge storage capacity electrodeposited iridium oxide film on liquid crystal polymer-based neural electrodes," *Sensor Mater*, vol. 28, no. 3, pp. 243-60, 2016.
- [102] K. S. Min, C. J. Lee, S. B. Jun, J. Kim, S. E. Lee, J. Shin, *et al.*, "A Liquid Crystal Polymer-Based Neuromodulation System: An Application on Animal Model of Neuropathic Pain," *Neuromodulation: Technology at the Neural Interface*, vol. 17, no. 2, pp. 160-169, 2014.
- [103] T. M. Gwon, J. H. Kim, G. J. Choi, and S. J. Kim, "Mechanical interlocking to improve metal-polymer adhesion in polymer-based neural electrodes and its impact on device reliability," *Journal of materials science*, vol. 51, no. 14, pp. 6897-6912, 2016.
- [104] S. W. Lee, K. S. Min, J. Jeong, J. Kim, and S. J. Kim, "Monolithic encapsulation of implantable neuroprosthetic devices using liquid crystal polymers," *IEEE Transactions on Biomedical Engineering*, vol. 58, no. 8, pp. 2255-2263, 2011.
- [105] G. J. Choi, J. Jang, S. Kim, C. Baek, S. Yun, S. Shim, *et al.*, "A Fully Implantable Wireless Stimulation System for Pigeon Navigation," *2019 41st Annual International Conference of the IEEE Engineering in Medicine and Biology Society (EMBC)*, pp. 5310-5313, 2019.
- [106] G. J. Choi, J. Jang, S. Kang, S. Shim, C. Baek, B. Kim, *et al.*, "Locomotion Control of Pigeons using Polymer-based Deep Brain Electrodes," *2018 40th Annual International Conference of the IEEE Engineering in Medicine and Biology Society (EMBC)*, pp. 1871-1874, 2018.
- [107] S. Yun, C. S. Koh, J. Jeong, J. Seo, S. H. Ahn, G. J. Choi, *et al.*, "Remote-Controlled Fully Implantable Neural Stimulator for Freely Moving Small Animal," *Electronics*, vol. 8, no. 6, p. 706, 2019.
- [108] R. H. Olsson, D. L. Buhl, A. M. Sirota, G. Buzsáki, and K. D. Wise, "Band-tunable and multiplexed integrated circuits for simultaneous recording and stimulation with microelectrode arrays," *IEEE transactions on biomedical engineering*, vol. 52, no. 7, pp.

1303-1311, 2005.

[109] C. M. Lopez, A. Andrei, S. Mitra, M. Welkenhuysen, W. Eberle, C. Bartic, *et al.*, "An implantable 455-active-electrode 52-channel CMOS neural probe," *IEEE Journal of Solid-State Circuits*, vol. 49, no. 1, pp. 248-261, 2013.

[110] M. Thorne, A. N. Salt, J. E. DeMott, M. M. Henson, O. Henson, and S. L. Gewalt, "Cochlear Fluid Space Dimensions for Six Species Derived From Reconstructions of Three-Dimensional Magnetic Resonance Images," *The Laryngoscope*, vol. 109, no. 10, pp. 1661-1668, 1999.

[111] V. Srinivasan and J. W. Weidner, "An electrochemical route for making porous nickel oxide electrochemical capacitors," *Journal of the Electrochemical Society*, vol. 144, no. 8, pp. L210-L213, 1997.

[112] X. Lang, A. Hirata, T. Fujita, and M. Chen, "Nanoporous metal/oxide hybrid electrodes for electrochemical supercapacitors," *Nature nanotechnology*, vol. 6, no. 4, p. 232, 2011.

[113] J. Kang, L. Chen, Y. Hou, C. Li, T. Fujita, X. Lang, *et al.*, "Electroplated thick manganese oxide films with ultrahigh capacitance," *Advanced Energy Materials*, vol. 3, no. 7, pp. 857-863, 2013.

[114] M. O. Hengartner, "The biochemistry of apoptosis," *Nature*, vol. 407, no. 6805, p. 770, 2000.

[115] H. Jia, J. Wang, F. François, A. Uziel, J. L. Puel, and F. Venail, "Molecular and cellular mechanisms of loss of residual hearing after cochlear implantation," *Annals of Otolaryngology & Laryngology*, vol. 122, no. 1, pp. 33-39, 2013.

[116] E. Bas, C. T. Dinh, C. Garnham, M. Polak, and T. R. Van de Water, "Conservation of hearing and protection of hair cells in cochlear implant patients' with residual hearing," *The Anatomical Record: Advances in Integrative Anatomy and Evolutionary Biology*, vol. 295, no. 11, pp. 1909-1927, 2012.

[117] A.-A. D. Lassig, T. A. Zwolan, and S. A. Telian, "Cochlear implant failures and revision," *Otology & Neurotology*, vol. 26, no. 4, pp. 624-634, 2005.

[118] C. Jolly, J. Mueller, S. Helbig, and S. Usami, "New trends with cochlear implant electrodes," *Otology Japan*, vol. 20, no. 3, pp. 239-246, 2010.

[119] B. Escudé, C. James, O. Deguine, N. Cochard, E. Eter, and B. Fraysse, "The size of the cochlea and predictions of insertion depth angles for cochlear implant electrodes," *Audiology and Neurotology*, vol. 11, no. Suppl. 1, pp. 27-33, 2006.

[120] R. Shepherd, K. Verhoeven, J. Xu, F. Risi, J. Fallon, and A. Wise, "An improved cochlear implant electrode array for use in experimental studies," *Hearing Research*, vol. 277,

no. 1–2, pp. 20-27, 7// 2011.

[121] Q. Cao, H. S. Kim, N. Pimparkar, J. P. Kulkarni, C. Wang, M. Shim, *et al.*, "Medium-scale carbon nanotube thin-film integrated circuits on flexible plastic substrates," *Nature*, vol. 454, no. 7203, p. 495, 2008.

[122] S. Miserendino, J. Yoo, A. Cassell, and Y.-C. Tai, "Electrochemical characterization of parylene-embedded carbon nanotube nanoelectrode arrays," *Nanotechnology*, vol. 17, no. 4, p. S23, 2006.

[123] H. N. Kha, B. K. Chen, G. M. Clark, and R. Jones, "Stiffness properties for Nucleus standard straight and contour electrode arrays," *Medical engineering & physics*, vol. 26, no. 8, pp. 677-685, 2004.

[124] S. Gallégo, B. Frachet, C. Micheyl, E. Truy, and L. Collet, "Cochlear implant performance and electrically-evoked auditory brain-stem response characteristics," *Electroencephalography and Clinical Neurophysiology/Evoked Potentials Section*, vol. 108, no. 6, pp. 521-525, 1998.

[125] S.-I. Hatsushika, R. K. Shepherd, Y. C. Tong, G. M. Clark, and S. Funasaka, "Dimensions of the scala tympani in the human and cat with reference to cochlear implants," *Annals of Otolaryngology, Rhinology & Laryngology*, vol. 99, no. 11, pp. 871-876, 1990.

[126] N. M. S. Abdelsalam and P. O. Afifi, "Electric auditory brainstem response (E-ABR) in cochlear implant children: effect of age at implantation and duration of implant use," *Egyptian Journal of Ear, Nose, Throat and Allied Sciences*, vol. 16, no. 2, pp. 145-150, 2015.

[127] R. Santarelli, P. Scimemi, E. Dal Monte, and E. Arslan, "Cochlear microphonic potential recorded by transtympanic electrocochleography in normally-hearing and hearing-impaired ears," *Acta otorhinolaryngologica italica*, vol. 26, no. 2, p. 78, 2006.

[128] S. Smart, A. Cassady, G. Lu, and D. Martin, "The biocompatibility of carbon nanotubes," *Carbon*, vol. 44, no. 6, pp. 1034-1047, 2006.

[129] H.-X. Ren, X. Chen, J.-H. Liu, N. Gu, and X.-J. Huang, "Toxicity of single-walled carbon nanotube: How we were wrong?," *Materials today*, vol. 13, no. 1, pp. 6-8, 2010.

[130] S. Tang, Y. Tang, L. Zhong, K. Murat, G. Asan, J. Yu, *et al.*, "Short-and long-term toxicities of multi-walled carbon nanotubes in vivo and in vitro," *Journal of Applied Toxicology*, vol. 32, no. 11, pp. 900-912, 2012.

[131] (28 october 2019). Kuraray. Available: https://www.kuraray.com.cn/Public/Uploads/image/product/20180925/20180925103609_83551.pdf

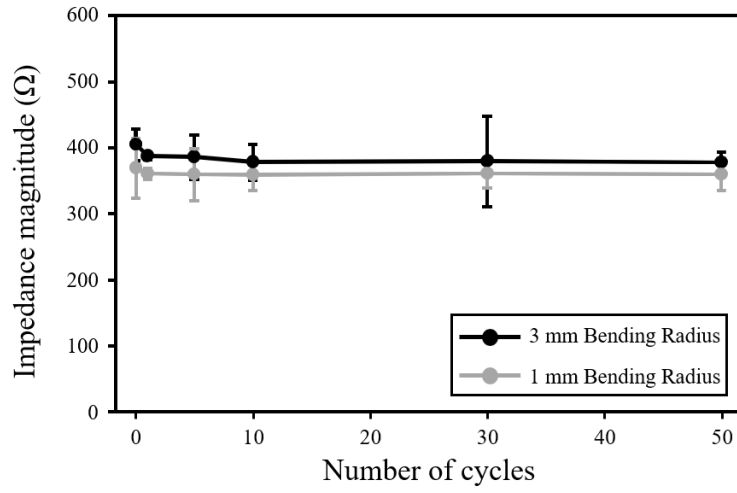
[132] A. C. Kuo, "Poly (dimethylsiloxane)," *Polymer data handbook*, pp. 411-435, 1999.

- [133] (28 october 2019). Specialty Coating Systems. Available: <https://scscoatings.com/wp-content/uploads/2017/09/02-SCS-Parylene-Properties-1016.pdf>
- [134] (28 october 2019). Dupont. Available: <https://www.dupont.com/content/dam/dupont/products-and-services/membranes-and-films/polyimide-films/documents/DEC-Kapton-summary-of-properties.pdf>
- [135] R. A. Serway and J. W. Jewett, *Principles of physics*. Saunders College Pub. Fort Worth, TX, 1998.
- [136] M. Uo, F. Watari, A. Yokoyama, H. Matsuno, and T. Kawasaki, "Tissue reaction around metal implants observed by X-ray scanning analytical microscopy," *Biomaterials*, vol. 22, no. 7, pp. 677-685, 2001.
- [137] S. Suzuki and Y. Ikada, "Devices for Bone Fixation," *Biomaterials for Surgical Operation: Springer*, pp. 131-144, 2012.
- [138] W. C. Oliver, R. Hutchings, and J. B. Pethica, "The wear behavior of nitrogen-implanted metals," *Metallurgical Transactions A*, vol. 15, no. 12, pp. 2221-2229, 1984.
- [139] S. Takahashi, J. Echigoya, T. Ueda, X. Li, and H. Hatafuku, "Martensitic transformation due to plastic deformation and magnetic properties in SUS 304 stainless steel," *Journal of Materials Processing Technology*, vol. 108, no. 2, pp. 213-216, 2001.
- [140] T. Akin, B. Ziaie, S. A. Nikles, and K. Najafi, "A modular micromachined high-density connector system for biomedical applications," *IEEE transactions on biomedical engineering*, vol. 46, no. 4, pp. 471-480, 1999.
- [141] Y. Zhang, M. Ishida, Y. Kazoe, Y. Sato, and N. Miki, "Water-vapor permeability control of PDMS by the dispersion of collagen powder," *IEEJ Transactions on Electrical and Electronic Engineering*, vol. 4, no. 3, pp. 442-449, 2009.
- [142] M. Nour, K. Berean, M. J. Griffin, G. I. Matthews, M. Bhaskaran, S. Sriram, *et al.*, "Nanocomposite carbon-PDMS membranes for gas separation," *Sensors and Actuators B: Chemical*, vol. 161, no. 1, pp. 982-988, 2012.
- [143] M. Nour, K. Berean, S. Balendhran, J. Z. Ou, J. Du Plessis, C. McSweeney, *et al.*, "CNT/PDMS composite membranes for H₂ and CH₄ gas separation," *International Journal of Hydrogen Energy*, vol. 38, no. 25, pp. 10494-10501, 2013.

Appendix

I. Bending Test of Gold Electroplated CNT Bundle

The impedance magnitudes of gold electroplated CNT bundles were measured during the bending test. The bending radii were 1 mm and 3 mm, and the number of cycles was 50. The same setup, described in the subsection 2.1.3.3, was used for the measurement of the impedance magnitudes. The measured area of the gold electroplated CNT bundles was 1 mm². Three bundles were used for each bending test with radius 1 mm and 3 mm,

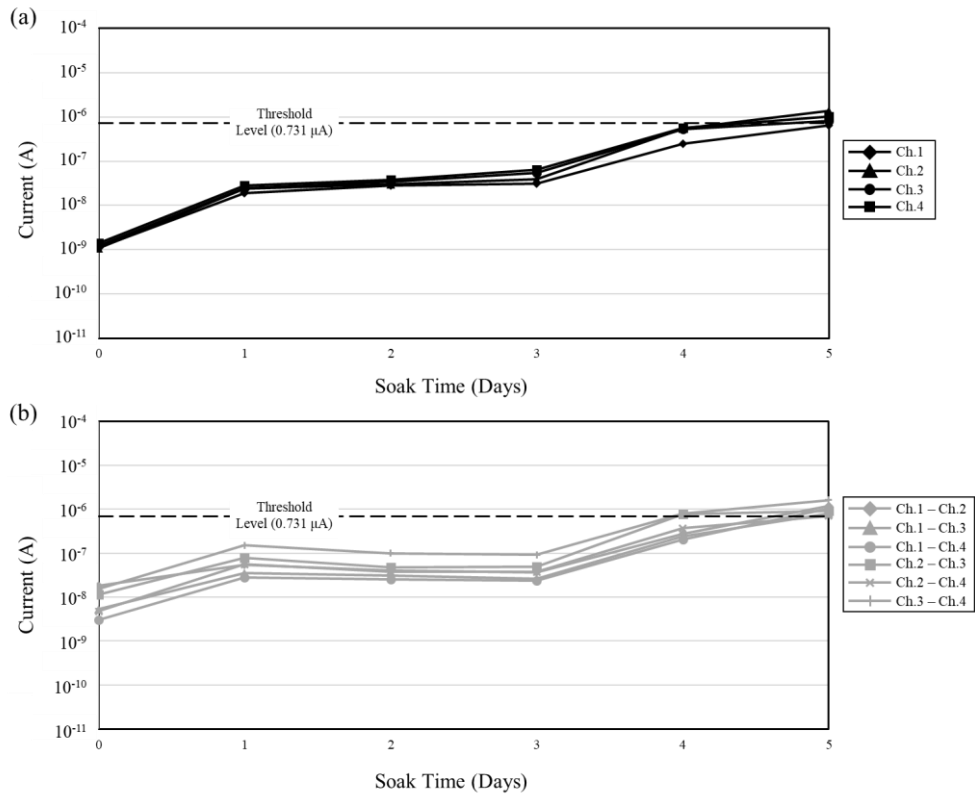


Appendix Figure 1.1 Impedance magnitude of gold electroplated CNT bundle during 50 bending cycles with 1 mm and 3 mm bending radii.

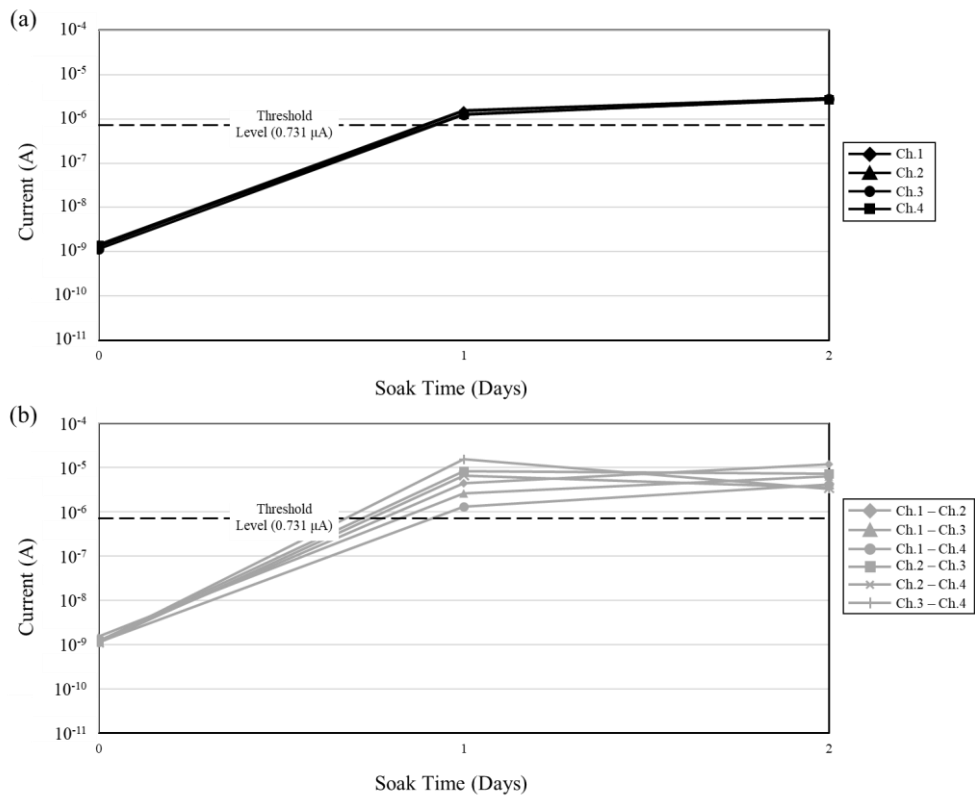
Appendix

II. Leakage and Crosstalk Current Measurements of Implantable Multi-channel Connectors

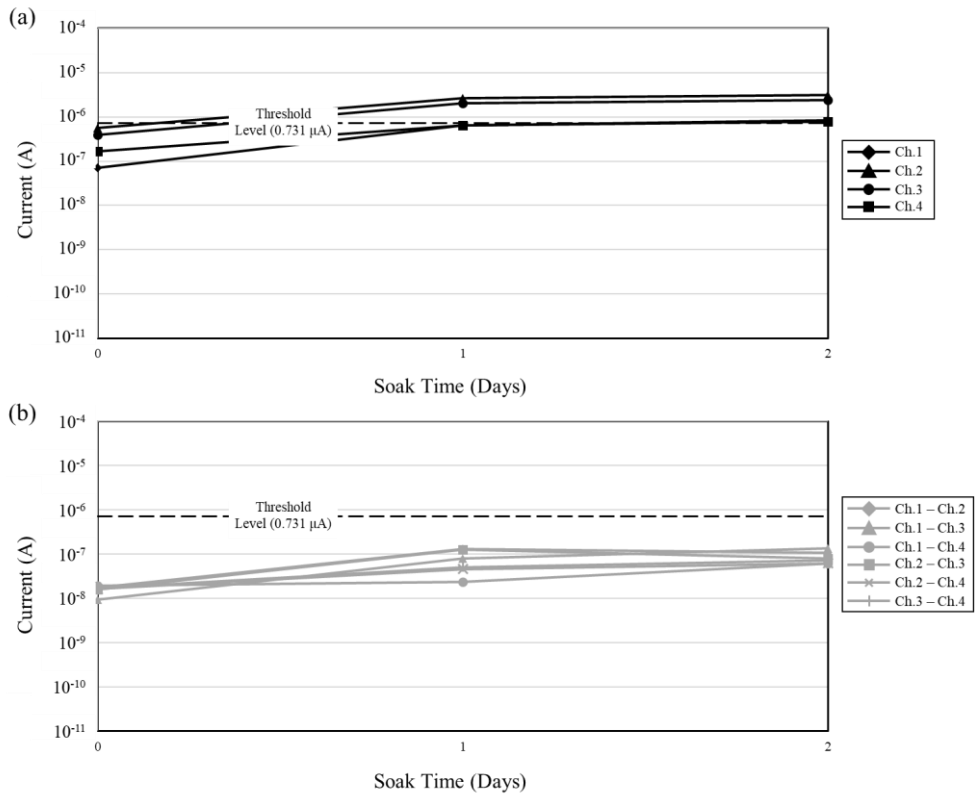
The leakage and crosstalk current were measured during the *in vitro* 75°C accelerated soak test. Connector samples were assembled with the metal cases and the silicone elastomer packings with various sizes. The block-shape packings have 125 %, 137 %, and 150 % volume ratio to the internal space of the metal case. For comparison, connector samples sealed with the dental resin and the silicone elastomer were also testes. The leakage and crosstalk currents in every channel of the samples are shown in each figure.



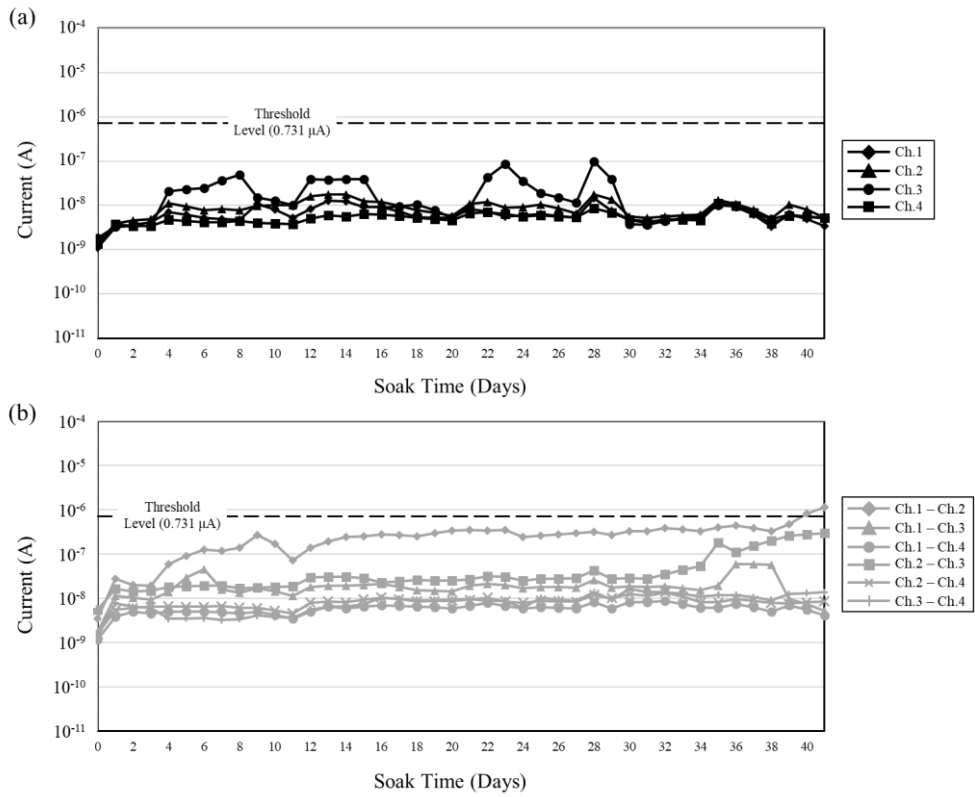
Appendix Figure 2.1 (a) Leakage and (b) crosstalk currents of connector sample (D1) sealed with dental resin during *in vitro* accelerated soak test.



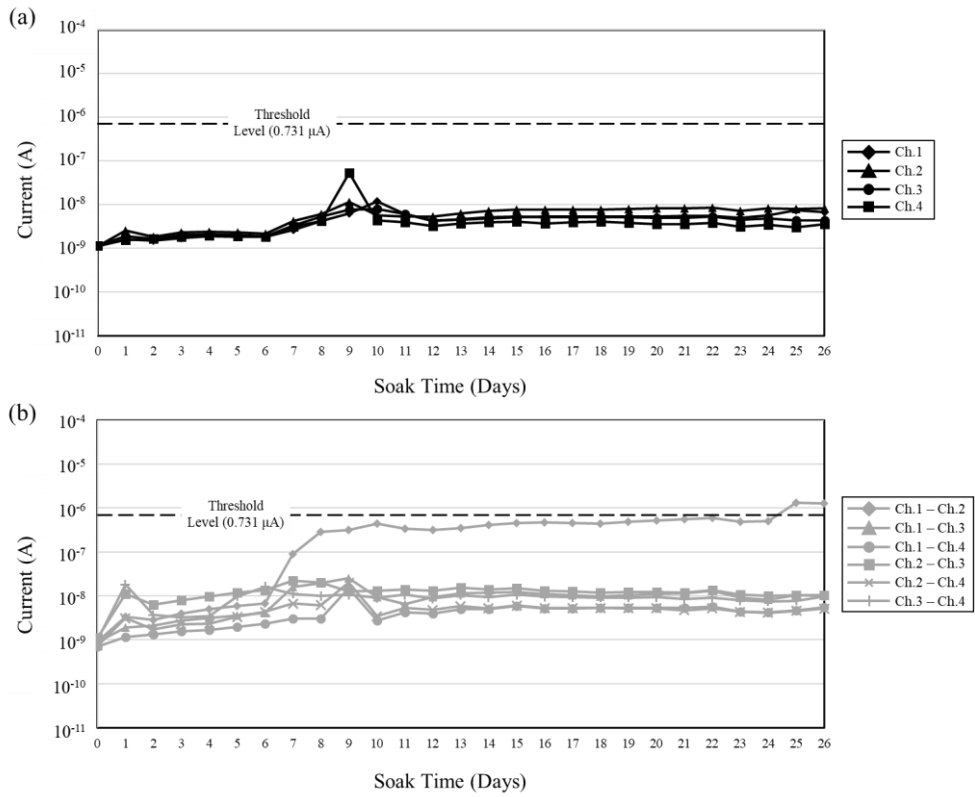
Appendix Figure 2.2 (a) Leakage and (b) crosstalk currents of connector sample (D2) sealed with dental resin during *in vitro* accelerated soak test.



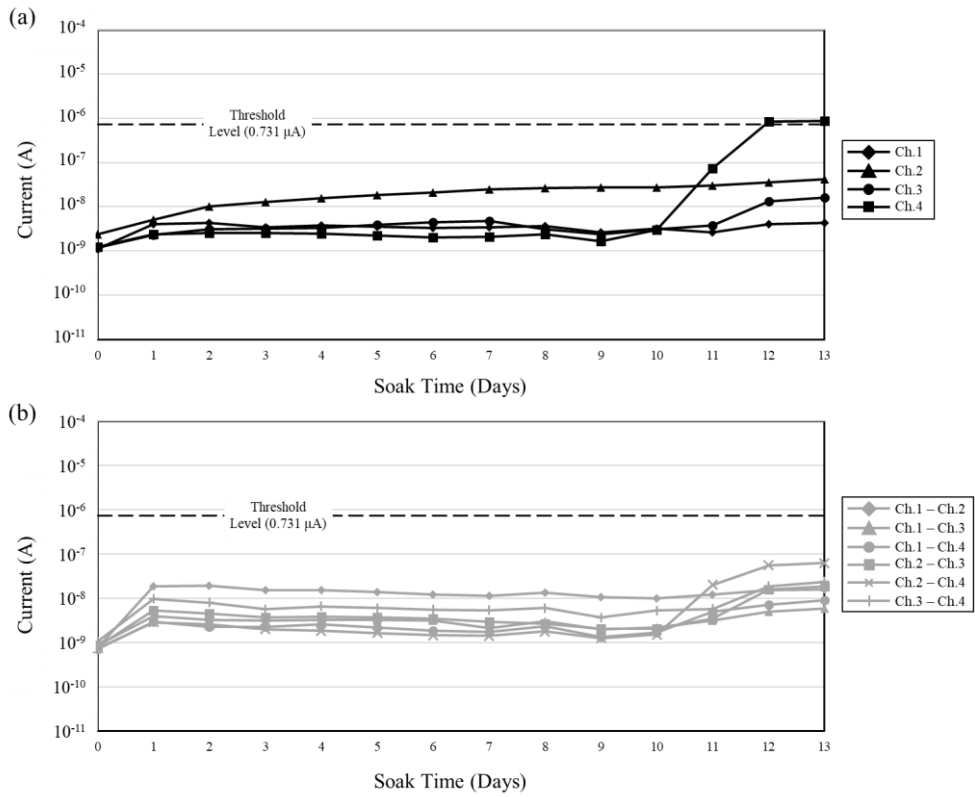
Appendix Figure 2.3 (a) Leakage and (b) crosstalk currents of connector sample (D3) sealed with dental resin during *in vitro* accelerated soak test.



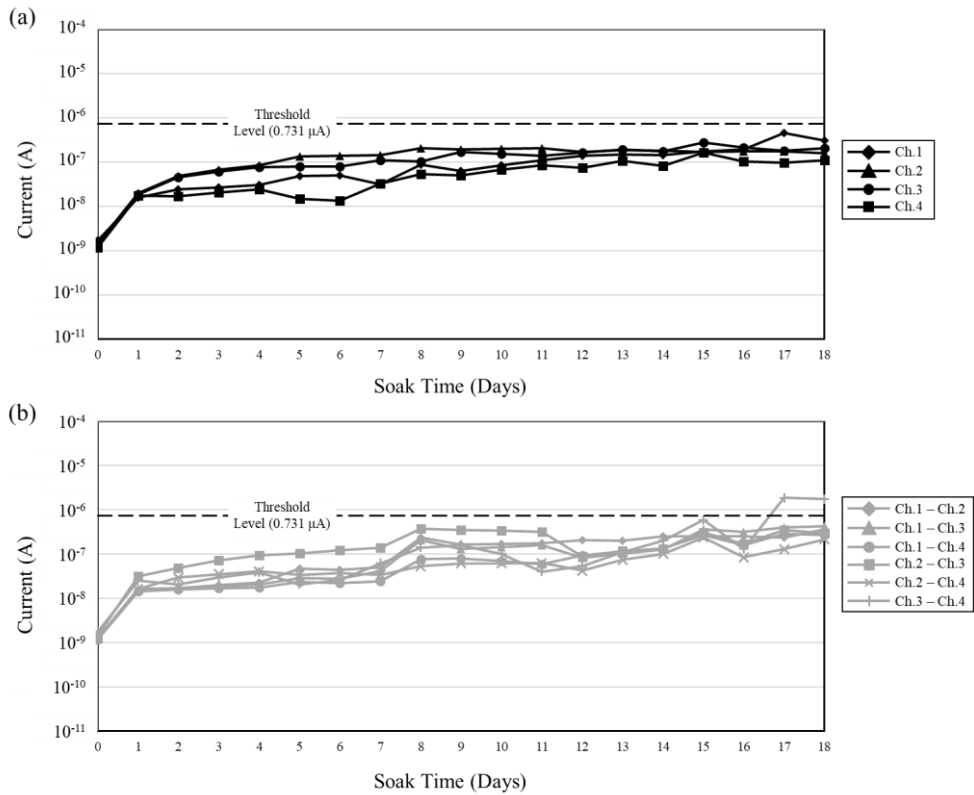
Appendix Figure 2.4 (a) Leakage and (b) crosstalk currents of connector sample (S1) sealed with silicone elastomer during *in vitro* accelerated soak test.



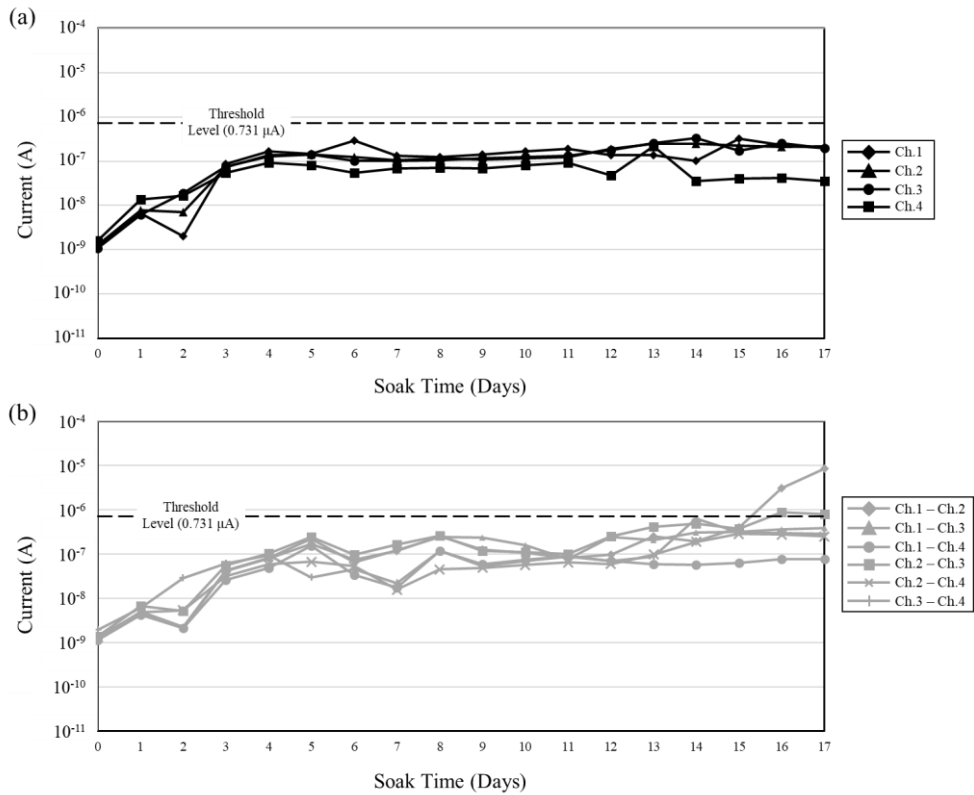
Appendix Figure 2.5 (a) Leakage and (b) crosstalk currents of connector sample (S2) sealed with silicone elastomer during *in vitro* accelerated soak test.



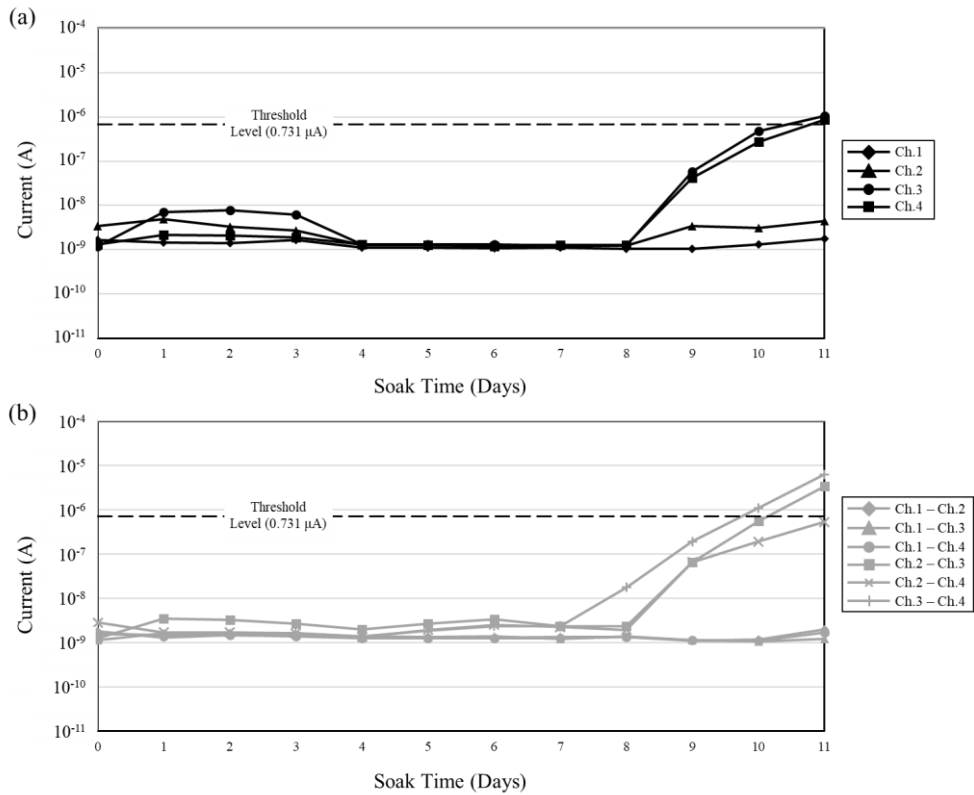
Appendix Figure 2.6 (a) Leakage and (b) crosstalk currents of connector sample (S3) sealed with silicone elastomer during *in vitro* accelerated soak test.



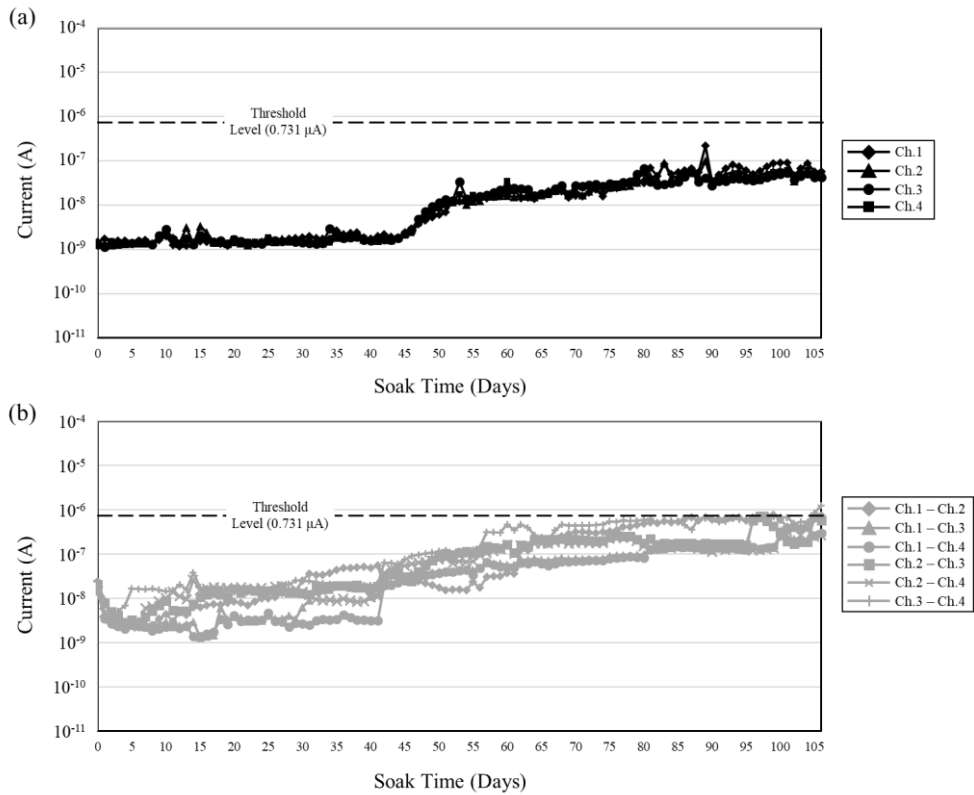
Appendix Figure 2.7 (a) Leakage and (b) crosstalk currents of connector sample (B1-1) samples during *in vitro* accelerated soak test. The sample was sealed with the metal cases and the block-shape packings having 125 % volume ratio.



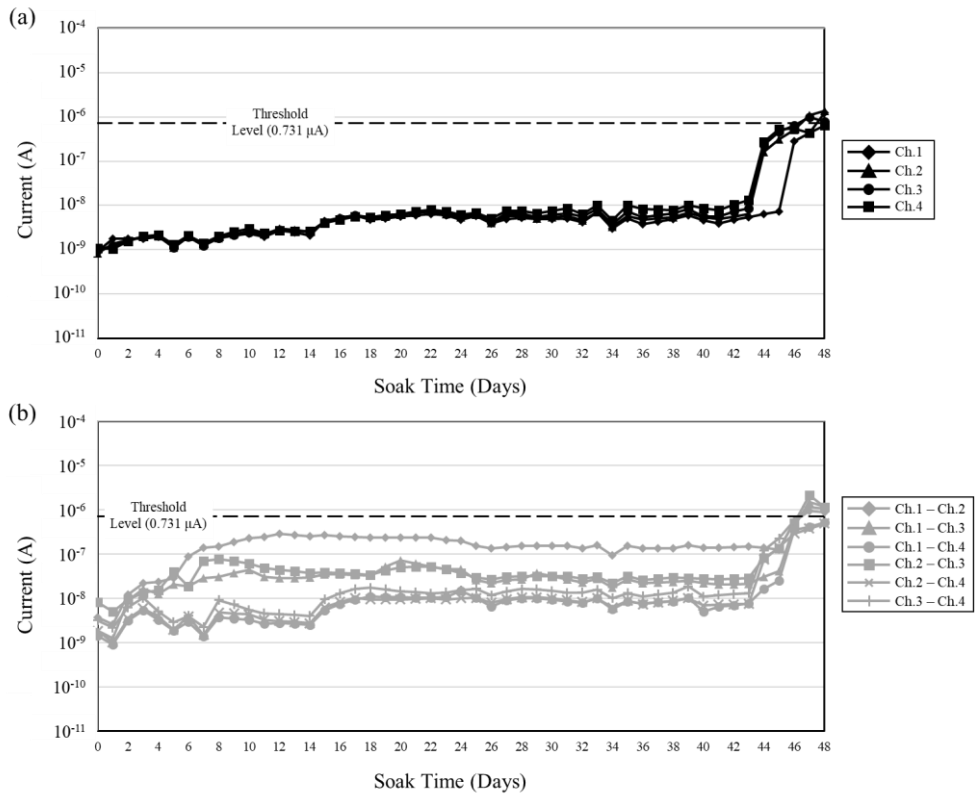
Appendix Figure 2.8 (a) Leakage and (b) crosstalk currents of connector sample (B1-2) samples during *in vitro* accelerated soak test. The sample was sealed with the metal cases and the block-shape packings having 125 % volume ratio.



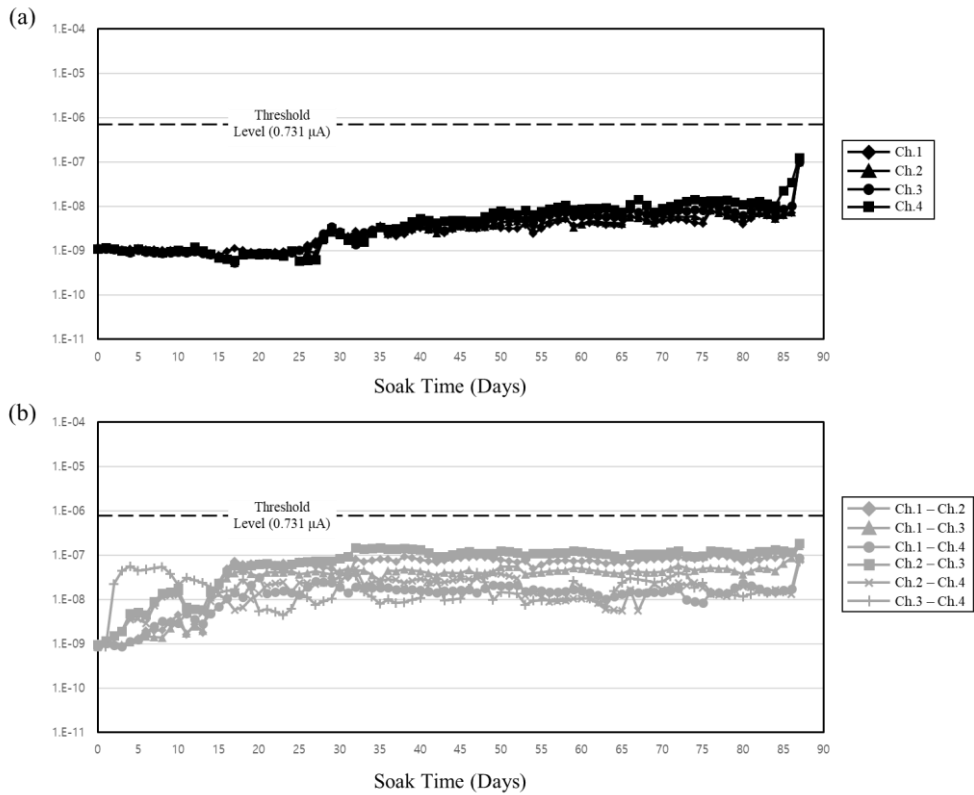
Appendix Figure 2.9 (a) Leakage and (b) crosstalk currents of connector sample (B1-3) samples during *in vitro* accelerated soak test. The sample was sealed with the metal cases and the block-shape packings having 125 % volume ratio.



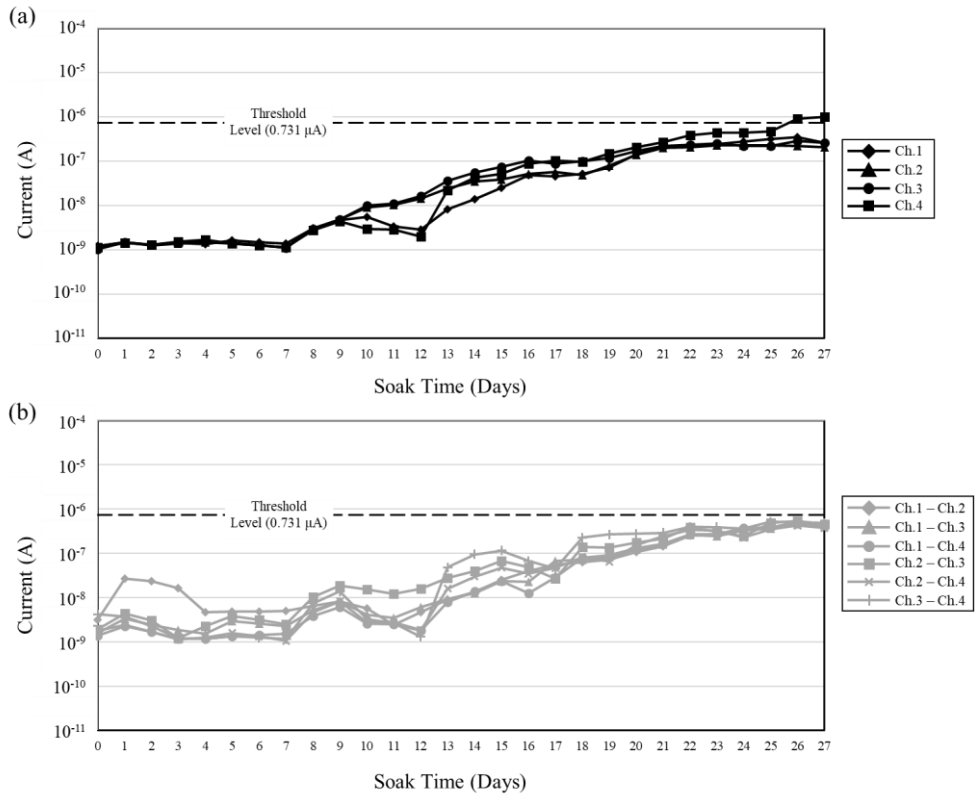
Appendix Figure 2.10 (a) Leakage and (b) crosstalk currents of connector sample (B2-1) samples during *in vitro* accelerated soak test. The sample was sealed with the metal cases and the block-shape packings having 137 % volume ratio.



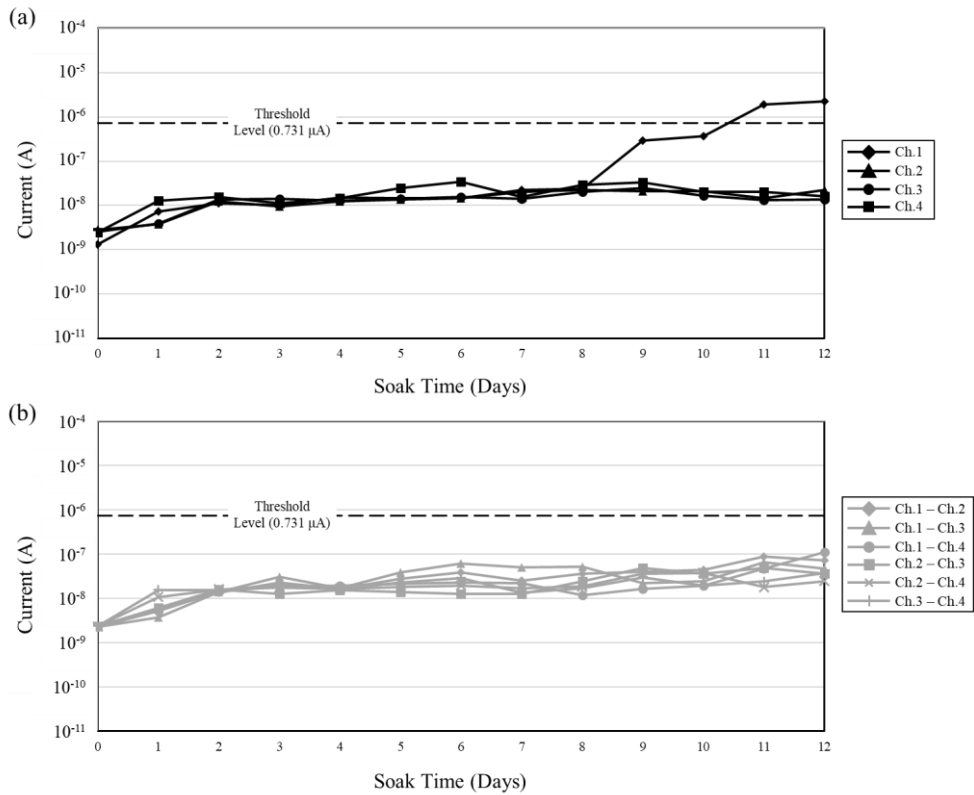
Appendix Figure 2.11 (a) Leakage and (b) crosstalk currents of connector sample (B2-2) samples during *in vitro* accelerated soak test. The sample was sealed with the metal cases and the block-shape packings having 137 % volume ratio.



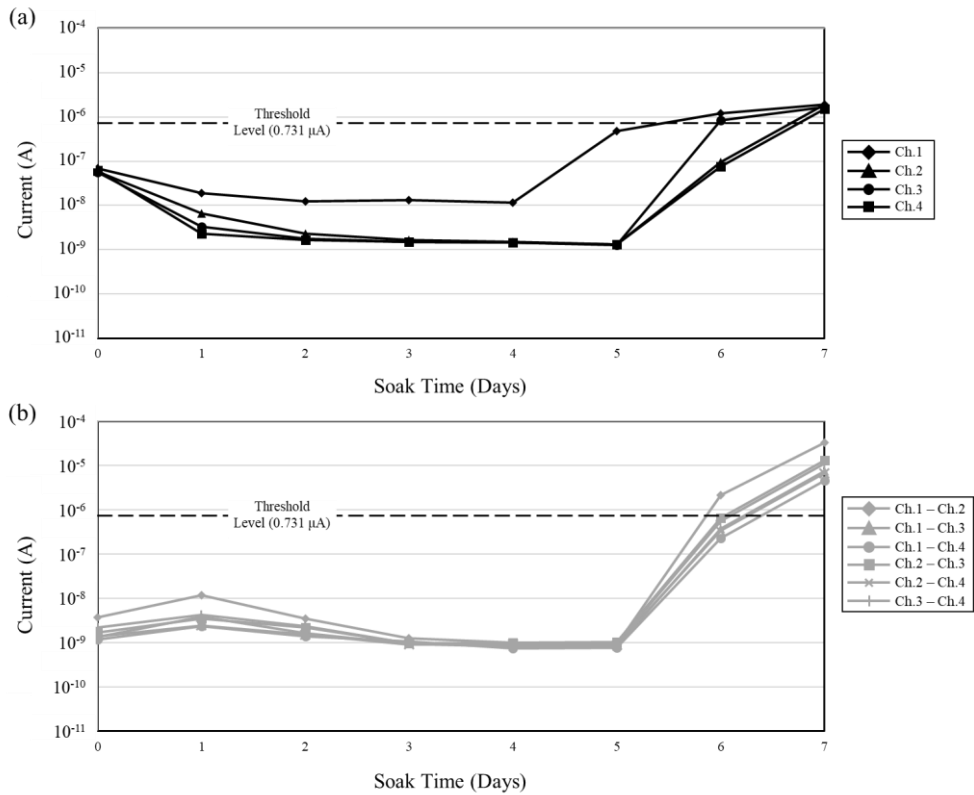
Appendix Figure 2.12 (a) Leakage and (b) crosstalk currents of connector sample (B2-3) samples during *in vitro* accelerated soak test. The sample was sealed with the metal cases and the block-shape packings having 137 % volume ratio. (Measurement is in progress)



Appendix Figure 2.13 (a) Leakage and (b) crosstalk currents of connector sample (B3-1) samples during *in vitro* accelerated soak test. The sample was sealed with the metal cases and the block-shape packings having 150 % volume ratio.



Appendix Figure 2.14 (a) Leakage and (b) crosstalk currents of connector sample (B3-2) samples during *in vitro* accelerated soak test. The sample was sealed with the metal cases and the block-shape packings having 150 % volume ratio.



Appendix Figure 2.15 (a) Leakage and (b) crosstalk currents of connector sample (B3-3) samples during *in vitro* accelerated soak test. The sample was sealed with the metal cases and the block-shape packings having 150 % volume ratio.

국문 초록

인공와우(cochlear implant)는 감각신경성 난청을 겪는 환자들에게 청력을 회복시켜주기 위해 이식되는 신경보철 기기이다. 인공와우 장치의 체내 삽입부는 전기자극 파형을 생성하는 밀봉 패키지와 청신경에 접촉하여 생성된 자극 파형을 전달하는 인공와우 전극으로 이루어진다. 인공와우 전극은 와우에 삽입되는 과정에서 조직의 손상을 일으킬 수 있기 때문에, 환자의 청력을 회복시키는 데에 중요한 요인으로 고려된다. 본 학위논문에서는 전극의 비외상성 삽입 위한 탄소나노튜브(carbon nanotube) 다발 기반의 얇은 인공와우 전극을 제안하였다. 다양한 의공학 분야에서 탄소나노튜브를 적용하기 위한 연구가 진행되고 있다. 금속 기반의 전극보다 낮은 강성을 갖는 신경 전극의 제작을 대표적인 예로 들 수 있다. 파릴린 C 로 코팅된 탄소나노튜브 다발이 각각의 전극 채널을 형성하는 데에 사용되었으며, 다수의 코팅된 다발을 하나로 뭉치는 방식을 통해 다채널의 인공와우 전극을 제작하였다. 제작된 전극은 기저부와 첨단부에서 각각 395 μm 와 135 μm 의 두께를 가져, 상용 인공와우 전극보다 얇게 제작되었다. 또한, 유연성과 자극 전극으로써의 동작을 확인하기 위해 삽입 시험과 동물실험을 진행하였다. 제작된 전극을 와우 모델 내에 삽입하면서 발생하는 삽입 힘을 측정하였으며, 쥐의 와우 조직에 삽입된 전극을 통해 전기자극을 가하여 전기자극 뇌간유발반응이 유발되는지를 확인하였다. 탄소나노튜브 다발 기반의 인공와우 전극은 금속 와이어 기

반의 전극에 비해 6배 낮은 삽입 힘을 보였으며, 제작된 전극을 통한 전기자극을 통해 전기자극 뇌간유발반응이 나타남을 보였다.

다양한 신경보철 기기에서 사용되는 생체삽입형 커넥터는 이식 수술 과정을 간소화하고 이식된 장치의 안전한 교체가 이루어질 수 있도록 한다. 신경보철 기기가 발전함에 따라 소형화되며 다채널을 가지는 생체삽입형 커넥터의 필요성 또한 대두되고 있다. 또한, 생체삽입형 커넥터는 인공와우 장치의 재이식과정을 안전하고 간소화하는 데에 사용될 수 있다. 현재 인공와우 장치는 인공와우 전극이 밀봉 패키지와 분리되지 않는 일체형 구조를 가진다. 이러한 인공와우 전극과 밀봉 패키지가 생체삽입형 커넥터를 통해 탈부착이 가능하다면, 보다 유연한 이식 수술 과정과 장치 교체 중에 일어날 수 있는 외상의 위험성을 줄일 수 있을 것으로 기대된다. 본 연구에서는 재연결이 가능하며 소형화된 생체삽입형 다채널 커넥터의 실험용 프로토타입을 제안하였다. 액정폴리머 필름을 사용한 미세 패턴 형성과 열압착 공정을 통해 양방향 암-암 구조의 커넥터가 제작되었다. 커넥터 내부에 형성된 요철 구조를 통해 케이블과 커넥터 사이의 접촉을 위한 압력이 가해져 전기적인 연결이 이루어지도록 하였다. 또한, 커넥터는 케이블과 연결된 후에 수분 침투를 방지하기 위해 실리콘 재질의 패키징 및 금속 케이스와의 결합으로 밀봉되었으며, 결합 후 $28.3 \text{ channel/cm}^2$ 의 높은 채널 밀도를 가지도록 제작되었다. 제작된 4채널 및 8채널 커넥터는 각각 $53.2 \text{ m}\Omega$ 과 $75.2 \text{ m}\Omega$ 의 접촉저항을 가

지며, 50회의 반복시험동안 일정한 값의 접촉저항이 유지되는 것을 확인하였다. 또한, 가속 담금 시험을 통해 커넥터의 밀봉 성능과 장기 신뢰성을 검증하였으며, 제작된 커넥터는 75 °C 온도에서 평균 79일 동안의 수분 침투가 방지됨을 확인하였다.

결과적으로, 기계적인 특성 측정 및 동물 실험을 통해 제작된 탄소나노튜브 기반 인공와우 전극에 대한 검증이 이루어졌다 또한, 제작된 생체삽입형 다채널 커넥터의 전기적, 기계적 특성 및 수분 침투 방지 성능을 확인하였다. 이러한 탄소나노튜브 기반의 인공와우 전극은 최소화된 삽입 힘을 가져 비외상성 삽입에 기여할 수 있을 것으로 예상된다. 또한, 제안된 생체삽입형 커넥터의 채널 밀도와 수분 침투 방지 성능의 추가적인 향상이 이루어진다면, 인공와우 장치에 적용되어 재이식 수술 과정의 안전성에 기여할 수 있을 것으로 기대된다.

주요어: 인공와우, 인공와우 전극, 비외상성 전극 삽입, 탄소나노튜브, 재이식술, 생체삽입형 커넥터, 고밀도 채널

학 번: 2015-20997